UNIVERSITAT DE BARCELONA

Combining Discrete Element and Process-based sedimentary models: a new tool to model syntectonic sedimentation

Ana Carmona Bardella

Institut de Recerca Geomodels

Grup de Geodinàmica i Anàlisis de Conques

Departament de Dinàmica de la Terra i de l'Oceà

Facultat de Ciències de la Terra

COMBINING DISCRETE ELEMENT AND PROCESS-BASED SEDIMENTARY MODELS: A NEW TOOL TO MODEL SYNTECTONIC SEDIMENTATION.

Memòria presentada per

Ana Carmona Bardella

per optar al títol de Doctor dins el programa de doctorat de Ciéncies de la Terra de la Universitat de Barcelona, sota la direcció del **Dr. Òscar Gratacós** i del **Dr. Stuart Hardy**.

Òscar Gratacos

Director

Stuart Hardy

Director

Pilar Queralt

Tutora

Ana Carmona Bardella

Juliol 2016, Barcelona

A la meva família.

AGRAÏMENTS

M'agradaria començar aquest agraïments amb els meus directors de tesi, sense ells, i els seus treballs previs, aquesta tesi no hauria estat possible. Gràcies Óscar Gratacós i Stuart Hardy pel vostre suport durant tots aquest anys.

Especialment m'agradaria agrair el suport incondicional de l'Óscar. Gràcies Óscar per la teva confiança. Gràcies per mirar que sempre tingués un recolzament econòmic. Gràcies per les discussions, i per estar disposat a solucionar qualsevol dubte. Gràcies per la teva paciència infinita; amb mi de vegades se'n necessita molta. I sobretot gràcies per totes les correccions, sobretot aquestes d'última hora... han millorat l'estructura, les idees i la qualitat del text. I no cal dir les figures! Gràcies per tota la teva ajuda i esforç per a que pogués acabar la tesi. En sóc conscient i t'ho agreixo.

Un altra persona clau en aquesta tesi ha sigut en Josep Anton Muñoz: gràcies per posar el fil a l'agulla, pels teus consells en els plantejaments dels exemples i per trobar solucions... en general, gràcies per la teva ajuda per que aquesta tesi arribés a bon port.

Durant tots aquest anys he tingut un company d'aventures 'professionals', que ha acabat convertint-se en un bon amic. Gràcies Roger Clavera per tots aquest anys d'amistat i recolzament, tant tècnic com geològic. Gràcies per les tardes 'fent el got' i les converses, on 'arreglàvem' les nostres tesis i de pas, el món.

En Miguel López i en Pau Arbués han estat també dos persones que han contribuït desinteressadament, tant en l'elaboració i correcció dels exemples com dels articles que han sortit (i sortiran!) d'aquesta tesi. Gràcies per tot el vostre ajut i la vostra paciència.

Aquesta llarga aventura va començar de la mà dels geofísics. Gràcies Pilar, Àlex i Juanjo, per obrir-me les portes del Departament ara ja fa uns quan anys, i per preguntar com va i tenir sempre unes paraules amables i de suport.

Durant aquest anys han estat molts els companys que han passat pel despatx 222. Però sempre ha estat un lloc tranquil i molt agradable de treballar-hi. Merci a tots per la vostra companyonia... Mireia, Oriol, Anna, Fabian, Joan, Xènia, Perla... crec que sóc la última que queda per aquí... ja era hora d'acabar! I als company del despatx del costat, Eloi i Lena, merci per la paciència en resoldre tots el meus dubtes!

Gràcies Anna Martí per la teva amistat tant dins com fora de la facultat.

Al reguitzell de gent que han compartit amb mi les hores de dinar, molts han anat marxant durant aquest anys, Héctor, Òskar, Marc, Jordi, Miquel i molts d'altres s'hi han

anat afegint, Oriol, Maria, Esther... i d'altres que no han canviat...Mireia, Óscar, Eduard, Oriol... gràcies a tots per aquestes estones de converses, riure i desconnexió!

La meva família sempre ha estat un puntal important de la meva vida, fa que tot plegat tingui sentit i, a més a més, em donen tot l'ajut i suport que necessito, emocional i logístic!

La meva mare és una MARE amb tot el sentit de la paraula. Que necessito ajuda?! Que necessito un cangur?! Doncs ella tant agafa un autobús com un avió i ve fins on jo sóc... i això que fa pocs anys pràcticament no havia sortit del poble. Mama, gràcies per tots els cangurs, pels dinars i per cuidar-me cada cop que ho he necessitat!

Papa, que ja acabo *d'estudiar*! Gràcies pel teu suport incondicional en totes les decisions que he pres, i per mirar que poguéssim accedir als estudis universitaris amb facilitat. Sóc una privilegiada!

Eva i Josep, gràcies per totes les bones estones que passem junts, pels soparons i les cervesetes, per les visites a Glasgow i a Milton quan us trobo a faltar, i pels 'súper' cangurs que feu del nen més guapo guapo del món!

Tinc un marit genial, que també em fa de supervisor de tesi, bé, o ho intenta! Pau, gràcies per l'empenta, els consells i les correccions. Et faig més cas del que et sembla. Sobretot gràcies per la paciència i sacrificis d'aquest últim any i mig... a partir d'ara tornem a tenir caps de setmana! Però sobretot, gràcies per respectar i valorar la meva feina. M'agrada estar al teu costat. A partir d'ara venen temps interessants... podrem finalment anar de vacances??!!

Bran, quantes estones sacrificades... i ja tens tres anys! Espero que tot l'esforç hagi valgut la pena... t'estimo amb bogeria!

La meva família política, fa molt temps que és també la meva família... gràcies Juan i Estefania per tot el suport i ànims per acabar aquesta tesi. Elena, ha sigut genial poder compartir amb tu aquest últim any i mig. Mil gràcies per les estones compartides, per les converses, i per deixar-me estar a casa vostra com si fos casa meva. I també per cuidar-me aquest últims dies!

Tot i que durant aquest últim any i mig, tinc la sensació d'haver estat aïllada i que només he fet tesi, tesi, tesi... la veritat és que són una collada de bons amics els que m'han acompanyat durant tots aquest anys, i que fan que la vida sigui molt més agradable:

A la meva colla de Tremp, gràcies per les excursions, per les sortides amb bicicleta, per les tardes de beurets! El món és més bonic i interessant amb vosaltres!

A les Maripilis, Cristina, Maria, Anna... i a les més garses, Rosa, Silvia, Davinia, Carina... gràcies pels soparons i les bones estones.

I a les meves més amigues, Anna B i Alicia, les estones amb vosaltres són de qualitat, gràcies per la vostra amistat! Que duri molts, molts anys...

Annita, sense tu, no sé qué faria!

Bea, I finally made it! Now, you are the next! Thank you for your encouragement and your freindship.

Ruth, Berta, Irma... ja fa uns quants anys que passàvem les hores al pati de física. Es un plaer que, tot i els canvis, ens puguem anar trobant, i posar-nos al dia amb les nostres vides. Busquem un dia per un berenar? Us he d'explicar que ja he acabat la tesi!

LIST OF FIGURES

LIST OF TABLES

ABSTRACT

The forward numerical model developed during this thesis is able to simulate deformation and sedimentation in one single setting. To do this, the model uses a novel approach that combines a Discrete Element Model (DEM) (Finch et al. 2004; Hardy and Finch 2006) and a process-based sedimentary model, the Simsafadim model (SFM) (Gratacós 2004, Gratacós et al. 2009a, Gratacós et al. 2009b), to link both processes, deformation and sedimentation (Carmona et al. 2010).

Discrete Element Modelling (DEM)

Discrete Element Modelling (DEM) deals with the simulation of deformation in different materials (Finch et al. 2004, Hardy 2011, Hardy 2013) in 2D and 3D. It is primarily used to investigate the propagation and evolution of deformation in the upper crust caused by tectonic movements. This deformation is a consequence of interaction of many individual elements according to mechanical rules, which are affected by the movement of rigid boundaries, simulating normal and reverse faults, etc., in order to produce different structures such as detachment folds (Hardy and Finch 2006), thrust/extensional fault-propagation folds (Finch et al. 2003, Hardy and Finch 2005), doubly vergent thrust wedges (Hardy et al. 2009) or the evolution of calderas (Hardy 2008).

The Discrete Element (DE) technique models the rock mass through an assemblage of spherical elements of different radii, which interact in pairs through a repulsive-attractive force as if they are connected by breakable elastic springs. The model can consider initial cohesion, i.e. two particles are bonded until their separation exceeds a defined breaking threshold and their bond is irreparably broken. The repulsive force acts again between the particles if the particle pair returns to a compressive contact. The model can also consider friction, which acts between two non-bonded particles in an opposite direction to that of the relative tangential velocity (Hardy et al. 2009). In addition, the model includes a viscous damping term, proportional to the particle velocity term, which is considered to make the model less dynamic and more quasi-static. This is assumed to be more suitable for modelling the development of tectonic structures over long time scales (cf. Donzé et al. 1994). Each element also considers the gravitational force, acting in the z direction. The deformation is simulated through small displacement of the rigid bounding box, where the discrete elements assemblage is confined. At each time step, which is chosen to ensure numerical precision and stability (Mora and Place 1994), particles proceed to their new position by integrating their equation of motion using Newtonian physics and

velocity Verlat Scheme (Allen and Tildesley 1987). The reader is referred to the bibliography for a full description of the DE methodology and model scaling (Finch et al. 2004, Hardy and Finch 2005, 2006, Hardy et al. 2009, Mora and Place 1993, 1994, Place et al. 2002).

Simsafadim (SFM)

Simsafadim (SFM) is a process-based numerical forward model, which simulates subaqueous clastic transport and sedimentation in three dimensions (Bitzer et al. 2002, Gratacós 2004, Gratacós et al. 2009a, Gratacós et al. 2009b), including processes of carbonate interaction, production, transport and sedimentation (Bitzer et al. 2002, Clavera et al. 2012). It can model effeciently the distribution of facies and the depositional architectures in a sedimentary basin and it is a powerful tool for the 3D prediction of stratigraphic structures.

SFM considers a 2D potential fluid flow system (Bitzer and Salas 2002, Gratacos 2004) in a transitional pattern. The fluid flow value in each node depends on the water depth, but it is considered constant along the water column. The transport model assumes that the sediment is transported in suspension mainly by advection processes as a result of the fluid flow velocity, but it also considers dispersion and diffusion terms (Gratacos 2004). Advance time step discretization is chosen according the Courant criterion, which gives interval time steps to ensure the stability of the differential equation solutions (Gratacós 2004). Both equations, fluid flow and transport, are solved using the finite element method (Kilzebach 1986). The sedimentation of the diferent materials is calculated in each node of the mesh, and the model assumes that a particle is susceptible to settling when the linear fluid flow velocity is lower than a critical settling velocity. This critical settling velocity is defined for each sediment type according its density and its grain size.

Combining sedimentation and deformation processes

The approach used to combine both processes treats each model separately without mixing up the two methods. The link between them is the surface of the DE assemblage, which shapes the topography of the basin while the sedimentary processes take place. The finite element mesh used to solve the equations of SFM is established over this assemblage surface. At each time step the z values of the mesh are updated according to the new position of the surface. The resulting basin topography will be a consequence of the deformation of the DE model plus the sediments added by SFM, whose settling patterns are now influenced by this deformation.

To choose the time step of model update, the requirements of the discretization time for convergence and stability of the mathematical methods used in each program is checked (Gratacós 2004, Hardy and Finch 2006). The smallest Δt is selected in order to ensure proper results for both programs.

When the amount of new sediment deposited in the model is higher than a critical value, e.g. when a number of nodes is reached with an amount of sediment equal or bigger than the diameter of a sphere, a numerical transfer of the settled sediments from SFM to discrete elements takes place. In this transfer the space taken up by the new sediment is refilled with new discrete elements. The transfer process allows the interaction of the new sediment with the pretectonic material in the DEM. The new spheres in the DEM summarize several time steps and stratigraphic units from SFM. Therefore, these new spheres can be coloured by the most abundant sediment type in the respective stratigraphic units, or by the individual sediment percentage of each sediment type.

Merging both codes provides a new tool for geological modelling (Carmona et al. 2010) in which deformation is influenced by the presence of syntectonic sediment dispersal and deposition. In addition, the tectonic processes change the topographic surface, which influences fluid flow, transport and, consequently, sedimentation in the process-based sedimentary model.

The tectonic and sedimentary models interchange allows also the study of the propagation of deformation in the syntectonic materials as well as how these new sediments influence the propagation of deformation in the pretectonic cover.

Therefore, the new tool can be used to predict and analyse various different syntectonic depositional architectures with complex geological scenarios.

The model is applied in two different cases studies. The motivation, configuration of the model to reproduce the geological setting, and the results of the case studies, are detailed in the next sections.

First case study: The Effect of Normal Faulting and a Relay Ramp on Sediment Dispersal

Relay ramps are common in extensional settings and play a significant role in sediment dispersal as they control sedimentary pathways. Unlike for subaerial settings, the impact of subaqueous relay ramps on sediment dispersal, clastic sedimentation and carbonate deposits evolution is less studied. In these subaqueous cases, numerical approximations could be a good approach to understand syntectonic sedimentation.

Considering this, the model to simulate syntectonic sedimentation is used to study the sedimentary infill in an extensional basin, specifically related to a relay ramp system. To perform the test study two configurations are designed: with one normal fault, and with two overlapping normal faults linked by a relay ramp. To these initial configurations, three different deformation velocities, 10, 5 and 2 cm/y, are applied in dip-slip direction. All these scenarios are considered as initially submerged. The same incoming amount of three different terrigenous sediments is considered in all the experiments. These sediments are transported basinward in suspension, by processes of advection, dispersion and diffusion.

Finally, the analysed examples also include four different boundary conditions for the sedimentary model, which define the source area location for the incoming water and sediment.

The different results show that the source area location in relation to the available accommodation space plays the major role in the distribution of different sediment types into the basin. Nonetheless, when the source area for water and sediment is defined as regional and parallel to the fault, the grain size distribution obtained by the two overlapping faults linked by a relay ramp have clear asymmetries when compared with the ones obtained by one-fault configurations. Therefore, the different extensional experiments allow us to conclude that the configuration with a relay ramp can play an important role in the distribution of the sediments into the basin.

Second case study: The effect of syntectonic sedimentation on fold geometry

Syntectonic sediments have been widely studied to decipher the kinematic evolution of different geological systems and structures. Nonetheless, the control of sediment on the structural style or on fold geometry is more difficult to determine, since it is complicated to derive conclusions directly from the geological record, as only the final stage can be observed. Considering this, a numerical model developed during this thesis is used to investigate the effect of syntectonic sedimentation on fold geometry specifically related to a delta progradation surrounded by two growing anticlines.

The initial DE model is defined with initial cohesion and a detachment level at the base of the model (with low cohesion). The model is tilted 1.6 degrees with an increasing bathymetry in $\boldsymbol{y}$ direction ranging from 51 to 861 m. Different shortening rates are defined perpendicular to $\boldsymbol{y}$-axis from right to left, corresponding to fold growth rates of 0.1, 0.5, 1 and 2 mm/y. At the base, two velocity discontinuities perpendicular to the shortening direction are defined acting as breaking points, which unleash in the formation of two folds. Total simulation time is 800ky. To this initial configuration, three different cases are

considered, one without sediments, and two with the addition of syntectonic sediments and considering two different rates of sea-level rise (0.25mm/y and 0.5mm/y). The incoming water and sediment points are located in the boundary with the lowest bathymetry.

The experiment with a fold growth rate of 1mm/y is analysed carefully, since is the one that show the clearest relationship between the two modelled processes. The main results obtained for these experiments are summarize as follow:

-Experiment without sedimentation: two detachment anticlines with box-fold geometry are obtained over the discontinuities defined at the base of the model.

- Experiment with sedimentation and a sea-level rise of 0.25mm/y: the deposition of the new materials clearly controls the geometry of the left-side fold, showing a left-vergent asymmetric wide anticline. Moreover, the strain suggests that this anticline is passing from a detachment fold to a fault propagation fold basinwards. Structural changes are more noticeable where sediment settling is higher.

- Experiment with sedimentation and a sea-level rise of 0,5 mm/y: the control of the syntectonic unit over the left-side anticline is more evident as a consequence of the increase in the accommodation space, e.g. the more proximal cross-section a-a' now is showing a fold-propagation fold instead of a detachment fold. Furthermore, the right-side anticline now is showing a right-vergent asymmetric geometry.

Summing up, the syntectonic sedimentation is controlling the fold style and the fold geometry. As a consequence, the inner syncline and the related sedimentary basin are also changing in transversal and longitudinal direction, being wider with syntectonic sedimentation and a higher sea-level rise.

Conclusions

The results of the experiments support the viability of the approach of combining the two models (i.e. SFM and DEM). Thus, we can conclude that the model meets the objective for which it is designed: this new tool allow us to study the syntectonic sedimentation (syntectonic architectures and sedimentary patterns in tectonic settings); and it also allows us to perform a more realistic and detailed investigation of the manner in which sedimentation and tectonics interact in nature.

RESUM

El principal objectiu d'aquesta tesi és donar un pas endavant en l'estudi i el coneixement de les conques sedimentàries, i dels processos geològics que intervenen en la seva formació, mitjançant la creació d'un model numèric per modelitzar la sedimentació sintectònica en un ambient subaquàtic.

El model numèric desenvolupat és capaç de modelitzar la sedimentació clàstica subaquàtica i la deformació de la unitat pretectònica en un sol programa. Per fer això, el model combina dos models ja existents: un model d'elements discrets (DEM) per simular la deformació de la unitat pretectònica (Finch et al 2004;. Hardy i Finch 2006), i Simsafadim (SFM), un model sedimentari basat en processos per modelitzar la sedimentació clàstica subaquàtica (Gratacós 2004 , Gratacós et al. 2009a, Gratacós et al. 2009b).

Model d'elements discrets (DEM)

El model d'elements discrets, utilitzat en aquesta tesi, està dissenyat per estudiar la deformació en diferents materials de l'escorça superior, com a conseqüència de moviments tectònics, tant en 2D com en 3D. En el model, aquesta deformació es simula mitjançant la interacció de molts elements individuals i d'acord amb unes regles mecàniques.

La tècnica dels elements discrets modela la unitat rocosa a través d'un conjunt d'elements esfèrics de radis diferents. Aquest elements interactuen entre ells a través de forces atractives-repulsives, com si estiguessin connectats per molles elàstiques. El model pot considerar una cohesió inicial entre els seus elements, és a dir, dos partícules estan lligades fins que la seva posició relativa excedeix una distància llindar determinada i el seu lligam es trenca irreversiblement. El model també pot considerar fricció, que actua en la direcció oposada a la velocitat tangencial relativa entre dues partícules que no estan lligades, bé per que no tenen cohesió inicial, o bé per que el lligam entre les partícules està trencat (Hardy et al. 2009). El model també inclou un terme d'esmorteïment viscós. Aquest terme és proporcional a la velocitat de les partícules, i té l'objectiu de reproduir la pèrdua d'energia del sistema, fent el model menys dinàmic i més estàtic, el que fa que el model sigui més idoni per modelar el desenvolupament d'estructures durant una escala de temps geològica (Donzé et al. 1994). Cada element del conjunt també considera la força gravitacional en l'eix z. La deformació del model es porta a terme mitjançant petits desplaçaments de les parets rígides que contenen el conjunt d'elements discrets. Les diferents configuracions d'aquestes parets i del seu moviment reproduiran diferents contextos tectònics, com per exemple un sistema extensiu o compressiu i la propagació de

falles normals o inverses. El passos de temps són escollits de manera que asseguren l'estabilitat i la precisió numèrica (Mora i Place 1994). A cada pas de temps, les partícules es mouen a la seva nova posició a través de la integració de les equacions de moviments. Aquestes equacions s'estableixen a través de la física Newtoniana i aplicant un esquema de velocitats de Verlat (Allen i Tildesley 1978). Es remet el lector a la bibliografia citada per a una descripció completa de la metodologia del model dels elements discrets (Finch et al. 2004, Hardy and Finch 2005, 2006, Hardy et al. 2009, Mora i Place 1993, 1994, Place et al. 2002).

Simsafadim (SFM)

Simdafadim (SFM) és un model numèric basat en processos que simula el transport i la sedimentació clàstica subaquàtica en tres dimensions (Bitzer et al. 2002, Gratacós 2004, Gratacós et al. 2009a, Gratacós et al. 2009b). El model inclou també processos de producció i sedimentació carbonatada (Bitzer et al. 2002, Gratacós 2004, Clavera et al. 2012), però que no seran considerats en aquesta tesi. SFM és capaç de modelitzar eficientment la distribució de fàcies i les arquitectures deposicionals en una conca sedimentària. SFM considera un sistema de flux per potencial en règim transitori, on la velocitat del flux és determinada en funció del caudal i la profunditat de la columna d'aigua, en la que es considera constant la velocitat obtinguda. El model de transport considera que el material és transportat principalment en suspensió per processos d'advecció resultants de la velocitat del fluid. No obstant també considera processos de transport del sediment per difusió i dispersió. Per garantir l'estabilitat numèrica dels resultats de les equacions diferencials, la discretització temporal es realitza mitjançat el criteri de Courant (Gratacós 2004). SFM utilitza el mètode numèric dels elements finits per resoldre les equacions de flux de fluid i transport (Kilzebach 1986). D'aquí que la batimetria inicial de la conca està discretitzada mitjançant una malla d'elements triangulars. La sedimentació dels diferents materials es calcula per cada node d'aquesta malla. SFM assumeix que una partícula pot sedimentar quan la velocitat lineal del flux de fluid que la transporta és menor que un valor crític. Tant la velocitat crítica de sedimentació, com la velocitat de deposició, es defineixen segons la mida de gra i la densitat del sediment clàstic considerat. Es remet el lector al treball de Gratacós (2004) per una descripció completa del model i dels processos que modelitza.

Combinació de processos de deformació i de sedimentació

Cada un dels models previs, DEM i SFM, tenen lloc en ambients i en escales temporals diferents. En el primer, els processos de deformació tenen lloc a la massa de roca de l'escorça, mentre que en el segon, el processos de transport i sedimentació, tenen lloc en un ambient superficial i subaquàtic. Per això, per combinar els dos processos, el nou model numèric busca els lligams entre SFM i DEM sense arribar a barrejar els seus mètodes.

Un dels lligams es troba en la superfície del conjunt dels elements discrets, que a partir d'ara serà la que donarà la topografia de la conca sedimentària modelitzada, on tenen lloc els processos modelitzats per SFM. Per fer això, la malla d'elements finits que s'utilitza per resoldre les equacions que governen el processos de transport i sedimentació, s'estableix sobre aquesta superfície del conjunt d'elements discrets. A cada pas de temps els nodes de la malla restabliran la seva posició d'acord amb la nova posició d'aquesta superfície, que variarà en funció de la deformació que està patint DEM. Així, la nova topografia serà conseqüència de la deformació i dels sediments depositats per SFM, alhora que influenciarà els processos que hi tenen lloc (nous canvis batimètrics).

L'altre lligam es troba en el sediments depositats per SFM, que passen a formar part del rebliment sedimentari. Quan aquest sediment dipositat és més alt que un valor crític, és a dir, la quantitat de sediment dipositada en un nombre de nodes és suficient per ser canviada per elements discrets, té lloc una transferència de sediments entre els models SFM i DEM. En aquesta transferència l'espai que correspon al cos sedimentari dipositat 's'omple' amb elements discrets. D'aquesta manera el nou sediment sintectònic passa a formar part de DEM i, en conseqüència, també pot ser deformat. Aquets pas també permet que el nous sediments dipositats interactuïn amb la unitat pretectònica, completant així la interacció entre els dos processos.

Degut a la seva mida, aquest nous elements discrets poden estar substituint vàries unitats estratigràfiques de SFM corresponents a diversos passos de temps. Els elements discrets poden registrar i representar el material més abundant de les unitats estratigràfiques a les que corresponen, la quantitat de sediment dipositat total i de cada tipus de sediment en particular, com també el seu percentatge.

La unió d'aquest dos models, DEM i SFM, proporciona una nova eina per la modelització geològica. En el nou model, l'evolució de la deformació canviarà la topografia de la conca que afectarà directament a la batimetria, influenciant així els processos de transport i sedimentació que hi tenen lloc.

Alhora aquesta evolució de la deformació de la unitat pretectònica estarà influenciada per la presència dels materials sintectònics. La interacció tectònica-sedimentació en el nou model, també permet estudiar la deformació en els materials sintectònics.

La nova eina de modelització permet simular i analitzar diferents arquitectures deposicionals sintectòniques i escenaris geològics més complexos.

Per tal de comprovar l'eficàcia del model, i per intentar ampliar el coneixement de com els processos de sedimentació-deformació interactuen en alguns ambients tectònics, la nova eina s'aplica per estudiar dos casos diferents. A continuació, en els dos apartats següents, es detallen la motivació de cada cas estudiat, la configuració del model per realitzar l'estudi i l'anàlisi i conclusions dels resultats obtinguts.

Primer estudi: efecte de la presencia de falles normals i de les zones de relleu en la dispersió del sediment.

Les zones de relleu són comunes en ambients extensionals i juguen un paper important en la distribució del sediments a la conca, ja que poden controlar les rutes i direccions de transport dels sediments. Aquest control de les zones de relleu en el transport de sediment està ben estudiat en les zones subaèries. No obstant, en ambients subaquàtics, l'impacte d'aquestes estructures en la dispersió i sedimentació de materials clàstics és menys conegut. En aquests casos els models numèrics poden ser una bona aproximació per mirar d'entendre el paper que juguen aquestes estructures en la sedimentació sintectònica subaquàtica.

Tenint en compte això, el model numèric desenvolupat en aquesta tesi s'utilitza per estudiar el rebliment d'una conca extensional específicament relacionada amb una zona de relleu. Per realitzar aquest estudi es realitzen dues configuracions estructurals diferents (moviments de les parets que contenen el model a DEM), la més senzilla, que reprodueix l'evolució d'una falla normal, i una segona per reproduir el moviment de dues falles normals solapades i comunicades mitjançant una zona de transferència o de relleu. Per cada una d'aquestes dues configuracions estructurals es consideren tres velocitats diferents de moviment de les falles (10, 5 y 2 cm/y). Finalment es defineixen 4 condicions de contorn diferents pel model sedimentari, que bàsicament indiquen la posició de l'àrea font, és dir, els punts d'entrada d'aigua i sediment a la conca. Els experiments consideren l'entrada de tres tipus de sediment diferents definits per la seva mida de gra. La quantitat d'entrada de cada tipus de sediment és la mateixa per a tots els experiments, i independentment de l'àrea font.

Els resultats analitzats mostren que la posició de l'àrea font respecte la configuració estructural i, per tant, de l'espai d'acomodació, és el factor que més influencia la distribució dels sediments a la conca. No obstant, quan l'àrea font es defineix paral·lela a la direcció de les falles, la distribució dels diferents tipus de sediments considerant dues falles mostra clares diferències quan la comparem amb la distribució obtinguda en la configuració amb una sola falla normal (en posició proximal o distal). Aquestes diferències són més visibles pels materials de mida de gra groller i mitjà, que són els que sedimenten a zones més properes de la zona de deformació. Ambdós materials mostren asimetries tant longitudinals com perpendiculars a les estructures que són més visibles per velocitats altes de deformació de les falles (més espai d'acomodació).

Segon estudi: efecte de la sedimentació sintectònica en la geometria d'un plec.

Les geometries i relacions dels cossos sedimentaris sintectònics han estat àmpliament estudiades per desxifrar l'evolució cinemàtica dels diferents sistemes geològics. No obstant, el control d'aquests sediments en l'estil estructural o sobre la geometria d'un plec és més difícil de determinar, atès que és complicat extreure conclusions directament del registre geològic, ja que només es pot observar la seva situació final. Tenint en compte això, el model numèric presentat en aquesta tesi s'utilitza per estudiar l'efecte de la sedimentació sintectònica en la geometria d'un sistema de plecs, específicament relacionada amb la progradació d'un sistema deltaic confinat per dos plecs en creixement.

El model d'elements discrets utilitzat en aquest estudi es defineix amb cohesió inicial. A la base del model s'hi defineix un nivell de baixa cohesió que actuarà com a nivell de desenganxament. El model està inclinat 1,6º, definint un augment de la batimetria en direcció *y* que va des dels 51 als 861 m. El moviment (de dreta a esquerra) de les parets del model defineix un escurçament perpendicular a l'eix *y*. A la paret de la base, es defineixen dues discontinuïtats de la seva velocitat de moviment, perpendiculars a la direcció d'escurçament. Aquestes discontinuïtats actuen com a punts de ruptura, on es desencadena la formació dels dos plecs anticlinals. Es defineixen quatre velocitats d'escurçament diferents que reprodueixen una velocitat d'aixecament dels plecs de 0.1, 0.5, 1.0 i 2.0mm/any. El temps total de simulació és 800.000 anys. Per a aquesta configuració inicial, es defineixen tres condicions inicials i de contorn pel model sedimentari: un sense sediments (que s'utilitza com a model de referència), i dos amb la incorporació de sediments sintectònics, tenint en compte dos increments del nivell del mar diferents: 0,25

mm/any i 0,5 mm/any. L'àrea font es defineix pel mig del contorn amb menys batimetria, coincidint amb la posició del futur sinclinal entre els dos anticlinals

Dels experiments proposats, els resultats obtinguts pels experiments amb una velocitat d'aixecament del plec d'1 mm/any s'analitzen a continuació. Aquest experiments són els que mostren una relació més clara de la interacció dels dos processos deformació-sedimentació. Els principals resultats obtinguts per aquests experiments es resumeixen tot seguit:

- Experiment sense sedimentació: S'obtenen dos plecs de desenganxament amb una geometria de *'plec en caixa'*, situats, cadascun d'ells, sobre les discontinuïtats definides a la base.

-Experiment amb sedimentació i un increment del nivell del mar de 0.25mm/any: S'aprecia com la sedimentació dels nous materials està afectant a la geometria del plec situat a l'esquerra del model. Aquest anticlinal ara és asimètric i té una clara vergència cap l'esquerra. A més a més, l'estudi de la deformació interna suggereix que l'estructura ha passat de ser un plec de desenganxament, a ser un plec de propagació de falla. Aquest canvis estructurals són més notables en les zones on la sedimentació és més alta.

-Experiment amb sedimentació i un increment del nivell del mar de 0.5mm/any: l'efecte de la sedimentació en la geometria del plec situat a l'esquerra del model és més evident, degut a una major sedimentació a conseqüència de l'augment de l'espai d'acomodació. A més a més, en aquest exemple, l'anticlinal situat a la dreta del model també mostra una asimetria i una vergència, però en aquest cas, cap a la dreta.

En els dos experiments que consideren sedimentació, el sinclinal situat entre els dos anticlinals també està canviant la seva geometria, transversalment i longitudinalment, essent més ample quan es considera sedimentació sintectònica i una pujada més gran del nivell del mar.

Resumint, els resultats conclouen que la sedimentació sintectònica pot condicionar la deformació de la unitat pretectònica i, per tant, l'estil i la geometria del plec/s anticlinal/s.

Conclusions

Els resultats dels experiments donen suport a la viabilitat de nou model, així com també a la metodologia desenvolupada per combinar els dos models previs de sedimentació i de deformació (és a dir, SFM i DEM). Per tant, podem concloure que el model compleix amb l'objectiu per al qual està dissenyat: aquesta nova eina permet l'estudi

de la sedimentació sintectònica (arquitectures deposicionals i patrons sedimentaris en ambients tectònics); i també ens permet realitzar un estudi més realista i detallat de la manera en què la sedimentació i la tectònica interactuen en la natura.

CHAPTER 1

INTRODUCTION

1.1 GENERAL INTRODUCTION

Humans rely on the natural environment to live. Therefore, the knowledge and understanding of this natural environment is essential to their own lives and survival. An important part of the natural resources necessary for human life to thrive comes from the Earth's rocky environment. However, this is an extremely complex environment, which extends to regions of difficult access, from where observations can only be acquired by indirect measurements of the subsoil (e.g., drilling or geophysical data). As a consequence of this limited observation, our understanding is also limited, since we only have direct access to a small part of the system we want to comprehend.

Moreover, the natural rocky environment that we observe today is the result of a long dynamical and physical evolutionary process requiring the interaction of many different geological processes. Hence, in order to understand the current state of the natural rocky environment and its heterogeneity, we require to infer the interaction and time evolution of the numerous geological process that have contributed to the geological reality we observe today.

Given this, the thesis presented here concerns itself with numerical modelling of geological processes. More specifically, this thesis deals with the simulation of deformation processes and syntectonic sedimentation in a subaqueous system. The thesis presents a new numerical model, which is able to model processes of sedimentation and deformation in a unified manner.

In order to reproduce the processes of sedimentation and deformation simultaneously, the new model combines two different models and their respective methodologies. The first model is a process-based numerical code, Simsafadim, referred to hereafter as **SMF**, which simulates processes of transport and sedimentation of different clastic grain-size sediments in a subaquatic environment, and also processes of carbonate production and sedimentation. The second is a 3D mechanical model based on the discrete element technique to model the deformation of a rock mass. Specifically, this **D**iscrete **E**lement **M**odel (**DEM**) is used to study the deformation in the upper crust due to tectonic movements. The main goal in merging both codes is to develop a new 3D tool to study the interaction of these two processes.

Combining both models allows a feedback between deformation and sedimentation. On the one hand, the deformation model is altering the topographic surface (the bottom basin geometry and/or the accommodation space), where processes of transport and sedimentation take place. Therefore, the resulting sedimentary bodies and their depositional architecture are now influenced by tectonic deformation. On the other hand, since these new sediments are also incorporated the deformation model, the progression of deformation can also be affected by the location and load of these new materials. Moreover, at the same time, these new materials can be deformed according to the deformation model.

The formation of sedimentary basins is related to deformation processes, due to both tectonic and/or lithosphere flexure processes. Also, a notable proportion of the infill of sedimentary basins takes place during the deformation period, i.e., during the formation of the basin itself. Hence, these two processes occur usually together in most of the geological environments. Therefore it is important to reproduce synchronously both processes to obtain a better approximation of the structures and geometries observed in nature. By combining both processes, the program allows modelling of much more complex depositional architectures (syntectonic geometries). Moreover, the program also allows a much more complete and realistic analysis of the evolution of the deformation and fracturing of these geological structures. Typically, deformation begins as a result of tectonic motion that affects the basement and propagates towards the sedimentary cover. The propagation of the deformation into the sedimentary cover is now influenced by the addition of the new syntectonic materials. Understanding the development of these syntectonic structures is important in many geological scientific areas, such as structural geology and stratigraphy. Their knowledge is also important for the natural resources exploration, such as water reservoir location, essential to human live; and gas and oil exploration, important in energy production and in other industrial fields.

The novelty of the work presented here is two-fold. On the one hand, as previously mentioned, the numerical model itself is presented as a novel tool to model syntectonic sedimentation. This model uses a new approach in coupling of deformation and sedimentation. On the other hand, this thesis also presents the results of applying the model to two different case studies. These case studies try to show the program's potential to deal with different contexts and scenarios. But more importantly, an exhaustive analysis has been performed in both case studies, and the results give new insights into how these two processes interact in the different modelled scenarios.

In the first case study, the numerical model is used to study the sedimentary infill in an extensional basin. The extension of the basin is modelled such that it specifically relates to the development of a relay ramp system. This example analyses the sedimentary pattern of three different grain-sized clastic sediments obtained under two configurations: a setup with one normal fault, and a second setup with two normal faults linked by a relay ramp.

In the second case study, the model is applied to analyse the influence of the syntectonic sedimentation on the fold geometry and evolution in a contractional environment. This case study takes as a reference the Sobrarbe Delta in the Ainsa Basin (Southern Pyrenees). This example reproduces the development of a delta complex located in a syncline between two growing folds under different contractional conditions.

The work undertaken during this thesis has resulted in the publication of two papers, published in international peer-reviewed journals. The first is titled "Modelling Syntectonic Sedimentation: combining a discrete element model of tectonic deformation and a process-based sedimentary model in 3D" and it was published in Mathematical Geosciences (Carmona et al. 2010). This paper is an introduction to the new model and its applicability through two simple test experiments. The second paper is titled "Numerical Modelling of Syntectonic Subaqueous Sedimentation: The Effect of Normal Faulting and a Relay Ramp on Sediment Dispersal". It presents the results obtained in the first case study, which studies the sedimentary infill in an extensional basin, specifically related to the development of a relay ramp system. This second paper is in press in Tectonophysics (Carmona et al. 2016). There is also a third paper in preparation, which aims to publish the results of the second case study. The different results achieved during the development of this thesis have been also presented in several international and regional conferences and workshops.

1.2 BACKGROUND

1.2.1 Numerical Modelling

Over the past decades, and thanks to the improvement of computer technology, numerical modelling has become an essential and useful tool in geosciences, geodynamics and, specifically, in the study of sedimentary basins. As mentioned before, numerical models help on the understanding of processes where direct observation is strongly limited, or impossible, in terms of space and time scale. They also provide information about geometries and architectures difficult to otherwise observe or quantify numerically. Even more important, numerical modelling can also help to reproduce the heterogeneity of the

natural environment, which controls the natural resources distribution and migration. Moreover, they may also be a useful validation tool for other methods such as 3D reconstruction and analogue modelling.

But what is a numerical model? Many definitions have attempted to describe the word 'model'. The most suited definition, considering the type of work that is reproduced here, is that of found in Kramer (2007): "models are a simplification of reality intended to promote understanding and reasoning". Even if the definition of modelling may vary depending on the context of its application, the essence of its meaning remains the same: the process of solving physical problems by appropriate simplification of reality. Therefore numerical modelling can be defined as: *the process by which we construct a simplified mathematical reality from a more complex physical one* (Barbour and Krahn 2004). In this processes, we make use of numerical methods.

A typical example of a numerical modelling methodology would be the one proposed by Mercer and Faust (1981) for groundwater modelling. They suggest the following steps, which have been repeated and reproduced by many authors (as well as by the models used in the present thesis):

- Develop an understanding of the physical system (Conceptual Model)
- Translate the physics describing your understanding into a mathematical system (Mathematical Model)
- Develop a solution of the mathematical model using numerical, analytic, graphical, analogue or other techniques.

The difficulty of problems treated in science typically originates from the complexity of the systems under consideration, and numerical models provide an adequate tool to break up this complexity and make a problem tractable (Velten 2009).

The development and selection of an appropriate approach, as well as the choice of the right numerical method, is a key step for a successful application of the numerical model. Many numerical methods have been developed to solve differently the problems and the mathematical system, such as the Finite Element Method (FE) and the Finite Difference Method (FD), which are more appropriate for continuum mediums; or the Discrete Element Method (DEM) (Cundal, 1978), which is useful where discontinuities play an important role such as in granular assemblies. Nonetheless, no single numerical method has been shown to be sufficient to fully study a particular problem. Hence, these numerical methods have evolved into more sophisticated methods. One example is the hybrid

FEMDEM (Munjiza 2004), which is used to apply the continuum mechanics principle in systems where the behaviour of individual particles is also important.

Due to the increase of numerical models in geosciences and engineering in the late 80's and early 90's, Oreskes et al. (1994) argue about the verification and validation of such models. After their analysis, they conclude that a complete validation is impossible and numerical models can only be evaluated in relative terms. Nonetheless, the primary value of models is heuristic: this means that numerical models help to improve the perception and understanding of the reality.

Barbour and Krahn (2004) also set out the objectives of the numerical models, how they should be used and interpreted. They conclude " ... *modelling is more about process than prediction. The modelling process is indeed a journey of discovery, a way of learning something new about the complex behaviour of our physical world. Furthermore, it is a process that can help us more fully understand highly complex real physical processes, and that can help us exercise our engineering judgment with increased confidence to make predictions*".

Hence, numerical modelling cannot pretend to reproduce the reality 'exactly', because our models will be just an abstraction or simplification of this reality. Nonetheless, they happen to be essential tools in the analysis and understanding of this reality. The more we can understand this reality, the more predictive we can be.

Bearing in mind the previous discussion, the objective of the work presented in this thesis is twofold: firstly, to understand the modelled processes and their interaction and, secondly, to understand the observed reality through these simulations. Moreover, this thesis also aims to validate the new numerical model, as well as its predictions and interpretations, by comparing the obtained results with simple real examples, which can be found easily in nature.

1.2.2 Numerical modelling of sedimentary basins

There are many processes involved in the formation of a sedimentary basin, as well as different environments where these processes are active. Transport and sedimentation can take place in either continental (fluvial systems, alluvial systems, continental shelf systems...) or subaquatic systems (marine systems, lacustrine systems, shallow waters, deep waters...). Besides the environment, there are different processes of transport and settling for different types of sediments (carbonates, conglomerates, sands, clay...). The basin can also undergo different deformation processes during its formation (tectonic movements, isostacy and flexure of the lithosphere due sediment load...), and it can suffer erosion due

different external causes (wind, water...). Moreover, there are also factors that can influence the evolution of the basin in distinct ways. The initial topography, the origin of the new sediments that are filling the basin, the position of the source area of the sediments related to basin position (and their evolution trough time), sea-level changes, are just some of these factors that can be involved in the basin formation. These processes and factors can have different roles in basin formation. Also, there may be different degrees of interaction and relationships between them, which could make the interpretation and understanding of the basin evolution even more complex.

It is here where numerical models can play an important role, since they can provide information in a relatively quick way; offering a wide range of possible scenarios by varying a few parameters. As a result of improvements in computer technology since 1970, numerical modelling has become an essential tool in the analysis of geological processes. Numerical modelling may assist in the understanding of geometries, architectures and processes difficult to otherwise observe in nature, or to understand by simple conceptual models.

There are many quantitative models that focus on the study of sedimentary basins. The most widely used are known as stratigraphic forward models. These models create synthetic strata based on simulated tectonics and various others processes of sediment transport and deposition (Paola 2000, Burgess 2007).

The simulation of the processes involved in the basin formation can be complex, mainly because they can occur in different environments and at different time scales. This is the reason why different authors tackle separately processes that occur in different environments of a sedimentary basin. Particularly, among the published work modelling the processes of transport and sedimentation, we can distinguish between those focussing on continental and those focussing on subaquatic environments.

In continental settings, authors have dealt with the modelling of fluvial and alluvial systems (Flemings and Jordan 1989, Murray and Paola 1997, Clevis et al. 2003, Nicholas and Quine 2007), fluvial to delta (Hoogendoor et al. 2008), as well as the evolution of continental shelf (Harris and Wiberg 1997). In subaquatic settings, the principal distinction is between the modelling of clastic sedimentation (Tetzlaff and Harbaugh 1989, Bitzer et al.1990, Ritchie et al. 2004a, 2004b, Tezlaff 2005) and the modelling of carbonate production and carbonate platforms formation (Bice 1991, Burgess et al. 2001, Bitzer and Salas 2002, Clavera-Gispert et al. 2012, Burgess 2013). Within the group of subaquatic clastic sedimentation models, the modelling of turbidity current, debris flows and gravity

currents have received special attention (Syvistky and Alcott 1995, Kneller and Buckee 2000, Blanchette et al. 2005, Waltham et al. 2008).

The development of plate tectonics had also a great impact in the understanding of sedimentary basin formation, once the connection between plate tectonics and stratigraphy was established. The growth of numerical models for basin subsidence also evolves into the coupling of these models with sedimentary numerical models in order to study the depositional architecture of the infilling sediment. Therefore, most of the models cited above already consider processes of basin subsidence due to the flexure of the lithosphere, caused by tectonics or sediment load. Nonetheless, these models focus on the processes of sedimentation and basin infill rather than on the subsidence processes itself (Paola 2000).

Once the modelled processes are understood and described, they are combined and coupled. Gradually new factors such as erosion, sea-level changes, river floods, climate and ocean storms are added to increment complexity. Some of these models have evolved into complete stratigraphic forward model packages for basin formation simulations, which allow the interplay of a large number of parameters in two and three dimensions. Some particular models also include a broad range of sediment environments, and they are known as models of the whole-sedimentary system (Paola 2000).

An example of the effort of combining different processes in a single framework is found in 2D SEDFLUX 1C (Syvitsky and Hutton 2001a), a 2D dimension process-based model developed to simulate continental margin strata. This model combines several single processes, among which the following are included; the modelling of spread of fluvial, bedload of coarse material, dispersion of the suspended sediment, ocean storm, failures of margin deposits and the consequent debris flows or turbidity currents, changes of the basin topography due thermal subsidence and tectonics, and compaction. The SEDFLUX 2.0 (Hutton and Syvitsky 2008) is an improved version of the its former 2D SEDFLUX, which adds the 3D in some of its features.

There are other examples of whole-sedimentary systems, such as ROMS v3.0 (Warner et al. 2009), which is a coupled model that implements sediment transport and the evolution of bottom morphology in a coastal circulation model.

DIONISOS (Granjeon and Joseph 1999, Burgess et al. 2006, Sømme et al. 2009, Granjeon 2010), a stratigraphic forward model, widely used in the hydrocarbon exploration industry, is another example of a whole-system model. Initially, DIONISOS was a siliclastic diffusion-based model, however it has been expanded to include other processes like: sea-level variations, oceanic currents, slope instability, sediment compaction,

basement erosion, carbonate production or evaporite precipitation, and deformation processes such as vertical uplift and subsidence, thrusts and growth faults, salt and shale diapirs.

SEDSIM is another whole-sedimentary system model that has been applied to hydrocarbon exploration and production problems (Griffiths et al. 2001, Huang et al. 2012). This is a three-dimensional numerical stratigraphic forward model that simulates a wide variety of depositional processes, such as sediment erosion, transport, and deposition both on geological and engineering time scales. SEDSIM can simulate also subsidence, flexural isostatic loading, compaction and slope failure, among others. It is controlled by a number of input parameters, for example, relative sea level/base-level curve, initial topography/bathymetry, tectonic movement, sediment input rates, etc.

1.2.3 Coupling processes of sedimentation and deformation

As previously discussed, the development, and later introduction, of deformation models for the lithosphere in the sedimentary basin interpretation was a big step towards the understanding of the sedimentary infill. The numerical simulation of the evolution of the basin due to the deformation of the lithosphere has also been a frequent subject from the early years in numerical modelling to nowadays. In this numerical models, the deformation of the lithosphere is mainly modelled as a consequence of tectonics or as a consequence of its own flexure due to the effect of sediment load. In this sense, the simulation of syntectonic sedimentation, understood as the combination of processes of deformation and sedimentation together, has been tackled by different authors.

Nonetheless, even combining both processes, most of these works are centred either in the evolution of the deformation, due to thermal and mechanical behaviour of the lithosphere, and the subsequent basin morphology (Kuznir, Garcia-Castellanos et al. 1997, Chen et al. 2013) or in the infilling of these sedimentary basin and in the changing strata geometries rather than the deformation itself (Fleming and Jordan 1989, Hutton and Syvitski 2006).

Some numerical modelling approaches are able to reproduce both sedimentation and deformation at the same time, treating their interaction in 2D and also 3D. Some of them are focussed in how the deformation rate is affected by sedimentation and erosion (e.g. Maniatis et al. 2009), while others include sedimentation as an additional phenomenon in the study of crustal rocks subject to specific tectonic boundary conditions (e.g. Gawthorpe and Hardy 2002, Simpson 2009). However, in most cases, sedimentation

processes are modelled either by a simple diffusive process or treated simply as a refill process, never as a real process that follows physical rules of transport and sedimentation.

Despite all the advances in tools for the analysis and modelling of sedimentary basins, there are still many aspects that need answer and further investigation. It is clear the importance of deformation processes on final geometry, as well as fracture and deformation patterns on sedimentary bodies; hence, it is necessary to consider deformation and sedimentary processes at the same time. When this approach is adopted, a more realistic geological model is obtained. Moreover a fully coupled tectonics-sedimentary model has to account both for tectonic controls on sedimentation and the effects of sediment transfer on tectonics.

Both processes working together imply more than just working simultaneously because one is affected by the other and vice versa (i.e. there is feedback and interaction). From the point of view of the deformation, the addition of new sediments to a deforming pretectonic unit affects its evolution. On the other hand, deformation affects previously deposited sediments and basin geometries thus creating a depositional environment that is going to affect directly the deposition of new sediments.

1.3 SCOPE OF THE THESIS: A NEW NUMERICAL MODEL TO COMBINE DEFORMATION AND SEDIMENTARY PROCESSES

The main objective of this thesis is to take a step forward in the modelling of sedimentary basins, by presenting a new model able to simulate both deformation and syntectonic subaquatic sedimentation. The merging of realistic models for deformation and sedimentation is the basis of the original work presented in this thesis. A new code has been developed that combines mechanical and sedimentary process-based numerical models. The merging of these two approaches allows us to include the simulation of both sedimentation and deformation processes in a single and more realistic model.

The new code has evolved from combining two previous published works: Simsafadim (SMF) (Bitzer and Salas 2002; Gratacós 2004; Gratacós et al. 2009a) and a discrete element model or DEM (Finch et al. 2003, 2004; Hardy and Finch 2005, 2006; Hardy 2008, Hardy et al. 2009). The former simulates sub-aquatic clastic transport and sedimentation in three dimensions, including processes of interaction, production and sedimentation of carbonates; moreover it is also powerful tool for the 3D prediction of stratigraphic structures and facies distribution modelling in sedimentary basins. The latter deals with the simulation of the deformation in sedimentary rocks in 2D and 3D. This

deformation is a consequence of interaction of many individual elements according to mechanical rules.

The new model presents a different approach to simulating syntectonic sedimentation. On the one hand the deformation model is focused in the mechanical deformation of the sedimentary upper crust. Deformation is as a consequence of tectonic movements that affect the basement. This deformation propagates into the sedimentary cover, producing faults and folds. On the other hand the sedimentary model is a process-based model, which is able to reproduce reliable sedimentary bodies in three dimensions with realistic depositional architectures. The main goal in merging these two models is to develop a new tool able to offer a more complex and realistic understanding of the evolution of the structures and deformation in sedimentary materials produced by faults and folds. Deformation is based in mechanical rules and is therefore, influenced by the presence of syntectonic sediments. In addition, the tectonic processes change the topographic surface, which influences fluid flow, transport and consequently, sedimentation in the sedimentary model. Therefore deformation is affecting the sedimentary bodies architecture as well as the facies distribution. Finally, analysis of the evolution of deformation within these new syntectonic materials can also be performed.

These two previous codes already are, by themselves, two established projects that have been widely tested through comparison with case studies and analogue models (see the aforementioned bibliography). They provide two effective tools for verification, prediction and study of geological processes (see next chapter to more information about these two works).

By merging these two codes, the new developed model allows us to model and analyse more complex geological structures. As a result of the capability of the new numerical model in reproducing these two processes simultaneously, syntectonic geometries can now be studied, together with more complex analysis of the evolution of the deformation.

The formation of sedimentary basins also includes complex processes that involve flexural and thickening or thinning of the lithosphere and the upper part of the mantle, where thermal processes are more important than mechanical processes. The scope of the models presented here does not deal with this type of deformation, neither with the processes that cause the deformations in the upper crust of the earth. Here the deformation model wants to study how this deformation is propagated through the upper sedimentary cover material. The new syntectonic sedimentary model does not include important

processes such as subsidence, or isostacy, but this can be assimilated in terms of accommodation space by the relative sea-level rise.

The characteristic of the programs allows modelling the basin in wide range of both spatial scale (regional or local, from meters to kilometres) and time scale (years to geological time scales).

1.4 WORK METHODOLOGY

The methodological procedure adopted in this thesis can be divided in two main parts. The first part concerns the development of the numerical model itself and its code. The second part concerns to the case studies modelled, whose development requires a methodological procedure by itself (summarized below).

1.3.1 Numerical modelling methodology

The procedure used to develop the numerical model can be divided in three main phases, which are the basic phases in any work aiming to develop a numerical model. These three phases are subdivided in a total of eight steps:

Initial Phase

- Step 1- Define the background of the problem to put the task in context. Literature review on the state of the art in numerical modelling of sedimentary basins and, specifically, the syntectonic sedimentation. Determine what needs to be done, why and how; i.e. define the background, motivation and methodology.
- Step 2- Study the theories/numerical models on which the new numerical model will be based. This means studying their respective backgrounds and basis as well as their numerical methods.
- Step 3- Look for and study the best technique to couple both models.

Development and building phase

- Step 4- Develop and implement the algorithm/algorithms to build the new code.
- Step 5- Test the new code looking for bugs and errors.

Verification phase

- Step 7- Apply the new model to simple case studies. Compare the results with sedimentary bodies found in nature. Evaluate the results as well as the working of the model, its limitations and advantages.
- Step 8- Draw conclusions about the numerical model and its applicability and limitations.

1.3.2 Methodological procedure to build a case study

The methodological procedure used to develop the case studies is divided in five steps:

- Step 1- Define the geological scenario that we attempt to study. This means, define the problem and its background, as well as its scientific interest; and also how has been tackled by the scientific community until now.

- Step 2 - Build the initial set up of the model. This implies building the appropriate DE assemblage and finite element mesh according the spatial scale of the problem to treat. The initial set up also needs to define the initial and boundary conditions, as well as the range of different parameters that will be used to characterize the examples. Some case studies would require modifying or/and expanding the code to simulate the boundary and movement conditions of DEM.
- Step 3 - Run the simulations.
- Step 4- Represent and analyse the data obtained in order to interpret and evaluate the results. Discuss these results with expert geologist in area treated.
- Step 5- Deduce deformation and sedimentary patterns and draw conclusions.

1.5 THESIS OUTLINE

This thesis has been structured in seven main chapters.

This first chapter provides a general introduction to the thesis. The chapter defines what numerical models are, how these models have to be understood and what their limitations are. A review of the state-of-the-art in numerical modelling of sedimentary basins is then provided, placing a special emphasis on the models that couple sedimentation and deformation processes. After that, the main objective and scope of the

thesis are settled, and the new numerical model and its capabilities are then introduced. A final section explains the methodology used in the development of this thesis.

The second chapter details the two initial models from which the numerical modelling developed in this thesis is based; a DEM simulating deformation of the upper sedimentary cover and SMF. The development and history of both models are described, together with their conceptual, mathematical basis and the numerical methods required to solve their differential equations and dynamical systems.

The third chapter presents the approach and methodology adopted to develop the new numerical model and its respective numerical code. This chapter is divided in three main sections. The first section present the work carried out before starting the development of the new model. A first overview of the methodology adopted to combine both previous models, Simsafadim and DEM, is also included in this section.

The second section presents the development of the new numerical code and its workflow. This section also discuss on the problems encountered during model development and how these problems were solved. A final section, including two simple examples to illustrate the proper working of the program, concludes the chapter.

The fourth chapter summarizes the several tasks and developments that modify and improve the model and its respective numerical code. These include upgrades and updates of the two inherited versions of DEM and SFM, as well as other numerical codes developed in order to build an initial model (i.e. the initial DE assemblage and the finite element mesh).

The fifth chapter presents the two aforementioned case studies.

The sixth chapter discusses the work done during this thesis, drawing appropriate conclusions and proposing future lines of research.

The seventh chapter summarizes the included and cited bibliography in this volume.

Finally, one appendix is added to the final volume. The appendix provides additional figures of the experiments presented in the chapter 5.2.

CHAPTER 2

PREVIOUS COMPONENTS: DEM AND SFM

As introduced in the previous chapter, the numerical model developed and presented in this thesis uses a novel approach that links a **D**iscrete **E**lement **M**odel (DEM) (Finch et al. 2004, Hardy and Finch 2006, Hardy et al. 2009) and a process-based sedimentary model, SFM (Gratacós 2004, Gratacós et al. 2009a, Gratacós et al. 2009b, Clavera-Gispert 2016), in order to synergistically combine the processes of deformation and sedimentation (Carmona et al. 2010, Carmona et al. 2016). In this chapter, a review of the theoretical basis (the conceptual and mathematical model) used by the aforementioned models, DEM and SFM, is summarized for a better and easier understanding of how the merged model works. In addition, a description of the historical development of each model and their subsequent evolution precedes each model description. For more detailed information on SFM and DEM, the reader is referred to the cited bibliography (i.e., Hardy et al. 2009 and Gratacós 2004).

Hereafter, the acronym DEM standing alone will refer to the particular implementation of the discrete element model used in the code developed for this thesis. On the other hand, the wording *discrete element method*, or *model*, will always refer to the general methodology.

2.1 DEM TO STUDY THE DEFORMATION OF THE UPPER CRUST

2.1.1 Introduction to the model of deformation

Rock masses are often under stress and continuously altered by different mechanisms and processes that affect the upper crust, such as tectonic movements, earthquakes, isostacy and land subsidence, among others. Numerical modelling has been proved to be a useful tool to study and to understand the deformation of the rock mass, and several numerical methods have been developed and applied to rock mechanics problems in different contexts and scenarios (Jing 2003, Bobet et al. 2009).

One of the most used numerical techniques is the discrete element technique, which has been widely applied to simulate and to study the mechanical behaviour of different rocks materials, due its nature and ability to reproduce faults, fractures and boundary conditions where discontinuities play an important role. Therefore, the discrete element technique has been used in different branches of geology, such as the modelization and

simulation of earthquakes mechanics (Scott 1996, Mora and Place 1998, 1999, Abe et al. 2006), or the study of the deformation behaviour of different materials under different contexts. For example, the study of deformation bands in sandstones (Antonellini and Pollard 1995), the analysis of the influence of porosity and crack density in cohesive materials (Schöpfer et al. 2007) and the propagation of blind normal faults in basaltic sequences (Hardy 2013) have all been performed using the discrete element technique. This technique has also been used to reproduce the evolution of geological structures with the objective to understand or to study their formation, e.g., the evolution of a faults system over active diapirs (Yin et al. 2009) or the evolution of calderas (Hardy 2008).

2.1.2 Background of the discrete element technique

The origins of the discrete element technique are based in the first granular media models. The technique is based in the idea that, instead of treating a material as a continuum, one can represented it as an assemblage of elements with defined interactions. These granular media models were born due the difficulty in performing actual measurements of internal stresses in granular materials, such as sand. The first granular models, geometrically more simple than sand, were analytical (Deresiewicz 1958) and physical (De Josselin de Jong and Verruijt 1969). But soon it was realized that the most effective and useful way to model the granular assemblies was using numerical techniques. Numerical models would allow a wide range of configurations and information during their evolution in time (Rodriguez-Ortiz 1974), and they can also imply different particle sizes and distributions and a larger number of particles.

One of the first implementation of the discrete element modelling is known as the 'distinct element method' and was developed by Cundall (Cundall 1971) for the analysis of rock mechanics problems. Later on, Cundall developed the program BALL (Cundall 1978), a 2D discrete numerical model for granular assemblies. The model was validated comparing their results with the corresponding plots of analytical photo-elastic analysis (Cundall and Strack 1979).

Most of the works and different branches of discrete element modelling that followed Cundall (1971), such as the modal method (William and Hocking 1985), the generalized discrete element method (William et al. 1987) or the discontinuous deformation analysis (Shy 1988), have indeed evolved from Cundall's initial work (see Morris et al. 2011 to have an overview the different branches and their characteristics). In addition, the discrete element technique has undergone different extensions, such as the discrete element modelling with no-spherical particle shapes (Cleary and Sawley 2002),

BEM, which combines the discrete element method with the boundary element method in a hybrid model (Lorig et al. 1986) or the DEM-FEM coupling (Munjiza et al. 1995, Munjiza 2004, Oñate and Rojek 2004), which merge the discrete element technique with the finite element model in a single model.

Nowadays, the different approaches of discrete element model are widely used in diverse research fields in science, engineering and even in industry, to tackle different problems where granular media, powder materials, molecular interactions, or discontinuous systems in general, have a relevant role. The areas where DEM is applied include such distinct disciplines as environmental sciences (Richard et al. 2004), the pharmaceutical industry (KetterHagen et al. 2009), industrial manufacturing business (Cleary 2000, Moreno et al 2003, Bertrand et al. 2005) and, obviously, rock mechanics (Morris et al. 2011), among others.

The main limitation, or disadvantage, of discrete element methods is (or was!) the long duration of their simulations when dealing with large assemblies of particles. Nowadays, however, this limitation is practically solved. Two main breakthroughs have been responsible for the latter; firstly, the increase in computational power and, secondly, the implementation of parallelized computations, e.g., using openMP or MPI, allowing us to run DEM in multicore processor computers or large clusters in much reduced times.

2.1.3 DEM

The **D**iscrete **E**lement **M**odel (DEM) used in this thesis was developed by Stuart Hardy and Emma Finch (Finch et al. 2003, 2004, Hardy and Finch 2005, 2006, Hardy et al. 2009) and it is a variant of the 'Lattice Solid Model' (Mora and Place 1993,1994, Mora et al. 2002), which at the same time is an evolution of the distinct element method proposed by (Cundall 1971). It was created with the objective to study and to investigate the propagation and evolution of deformation in the upper crust caused by tectonic movement, and it was developed in 2D and 3D. While the methodology and basis of the model are already widely expounded in the bibliography, a summary is given here to help the reader to understand the method.

Discrete element modelling uses an assemblage of spherical elements to model a rock mass (fig. 2.1.1 A). These discrete spheres interact in pairs through a repulsive-attractive force as if they are connected by breakable elastic springs (Mora and Place, 1993). The particles can also consider cohesion and friction.

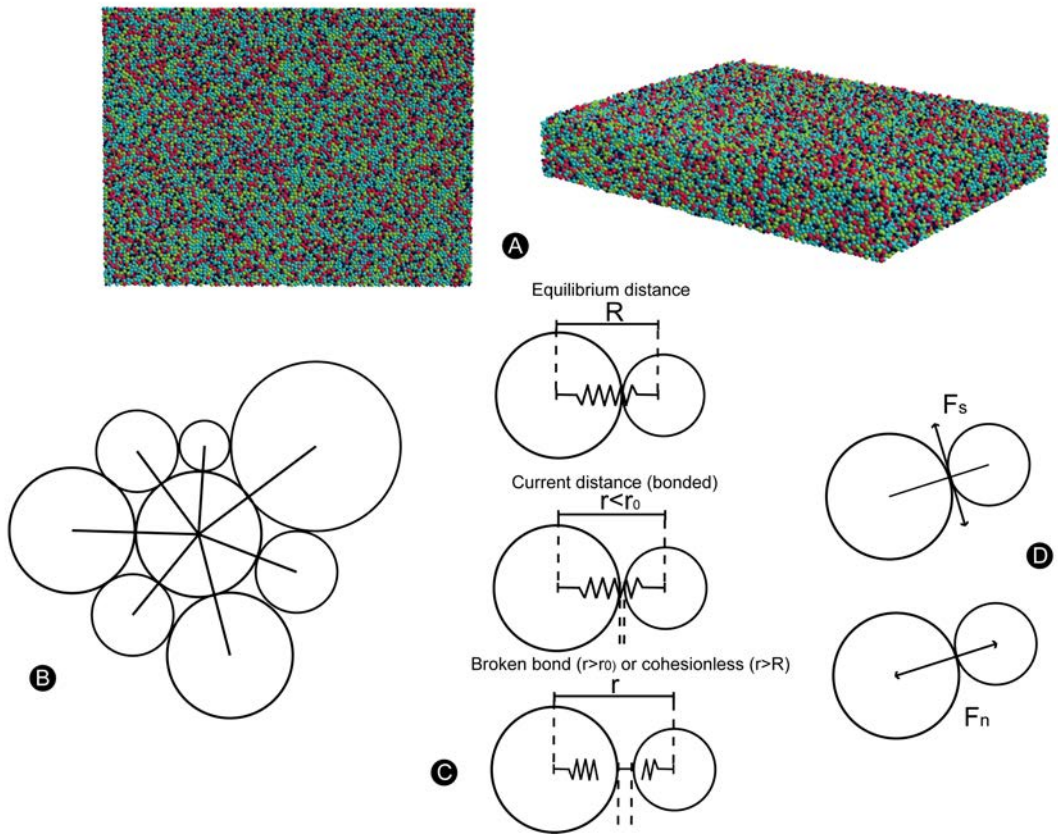

Figure 2.1.1. A- An example of a 3D spheres assemblage of four different radii used by DEM. B - Interaction of one element 'i' with its neighbours. C- Different possible interactions between two particles according their current distance r and the definition of equilibrium distance, R, and breaking separation threshold r_0. D- Direction of the shear and normal force acting between two particles (modified from Hardy et al. 2009)

To define the strength of a bond, a breaking separation threshold is defined. Two particles are bonded until the separation between them exceeds this upper limit, after that the bond is irreparably broken (fig. 2.1.1 B). Nevertheless the repulsive force can act again between them if the particle pair goes back to a compressive contact. The resultant normal force, F_n is given by (Finch et al. 2003, Hardy et al. 2009):

$$F_n = \begin{cases} K(r-R), & r < r_0, \quad intact\ bond \\ K(r-R), & r < R, \quad broken\ bond \\ 0, & r \geq R, \quad broken\ bond \end{cases}$$

Equation (2.1.1)

K - Elastic constant

r0 - Breaking threshold separation distance

r - Separation distance between particles

R - Equilibrium distance between particles

Friction (Hardy et al. 2009), when activated, acts between particles when they are initially unbounded or a bound is broken. The frictional force, F_s (Eq. 2.1.2), acts in opposite direction to the tangential velocity (fig 2.1.1C). Therefore, this shear force comes as a result of the perpendicular displacement to the vector that connects the particles centroids (X_s). It is modelled as a threshold-limited elastic spring in parallel with that used to calculate the normal forces and the magnitude of this force is limited to be less than or equal to the shear force allowed by Coulomb friction:

$$F_s = K_s X_s$$

$$F_{smax} = \mu F_n$$

$$F_s = F_{smax}, \quad if\ (F_s > F_{smax})$$

Equation (2.1.2)

F_s - Frictional force

F_{smax} - Maximum frictional force

K_s - Shear elastic constant

X_s - Perpendicular displacement

In order to calculate the total elastic force applied on a particle, it is only necessary to sum all the forces, normal and tangential, on each bond that link the particle to all its neighbours.

$$F_{i,\alpha} = \sum_{j=1}^{\alpha\ neighbours} F_{i,j}$$

Equation (2.1.3)

α - Number of neighbours of the element

Fi,j - Force between the particles i and its neighbour j

Fi,α -Total elastic force applied by its α neighbours to the particle i

The gravitational force is finally added to the total force acting on each element. In addition, a viscous damping term is included. This viscous damping term is proportional to the particle velocity and it is considered in order to make the model less dynamic and more quasi-static, which is more suitable for modelling the development of tectonic structures over long time scales (Donzé et al. 1993, Mora and Place 1994). So the total force applied in each particle is given by:

$$\boldsymbol{F} = \boldsymbol{F_{i,\alpha}} + \boldsymbol{F_g} - \nu\dot{\boldsymbol{x}}$$

Equation (2.1.4)

Fi,α - Total elastic force applied by its α neighbours to the particle i

F_g - Gravitational force

$\nu\dot{x}$ - Viscous damping term (ν, viscous coefficient; $\dot{\boldsymbol{x}}$, velocity)

The assemblage is confined into a bounding box. The time step is chosen to ensure numerical precision and stability (see next section 2.1.3.1). The bottom of the box is supposed to be the basement and it is considered to be rigid and undeformable. We carry out the deformation making small displacements to this bounding box for each time step (fig 2.1.2). The displacements are performed according to the process of choice; a normal fault, strike-slip, a detachment fold, etc. At each time step, particles proceed to their new position by integrating their equation of motion using Newtonian physics and the explicit velocity Verlat Scheme (Allen and Tildesley, 1987):

$$x(t+\Delta t) = x(t) + \Delta t\dot{x}(t) + \frac{\Delta t^2}{2!}\ddot{x}(t)$$

$$\dot{x}(t+\Delta t) = \dot{x}(t) + \frac{\Delta t}{2}(\ddot{x}(t) + \ddot{x}(t+\Delta t))$$

$$\ddot{x}(t) = F(t)/M$$

Equation (2.1.5)

x - Position of the particle

$\dot{x}$ -Velocity of the particle

$\ddot{x}$ - Acceleration of the particle

M - Particle mass

F - Total force acting in the particle

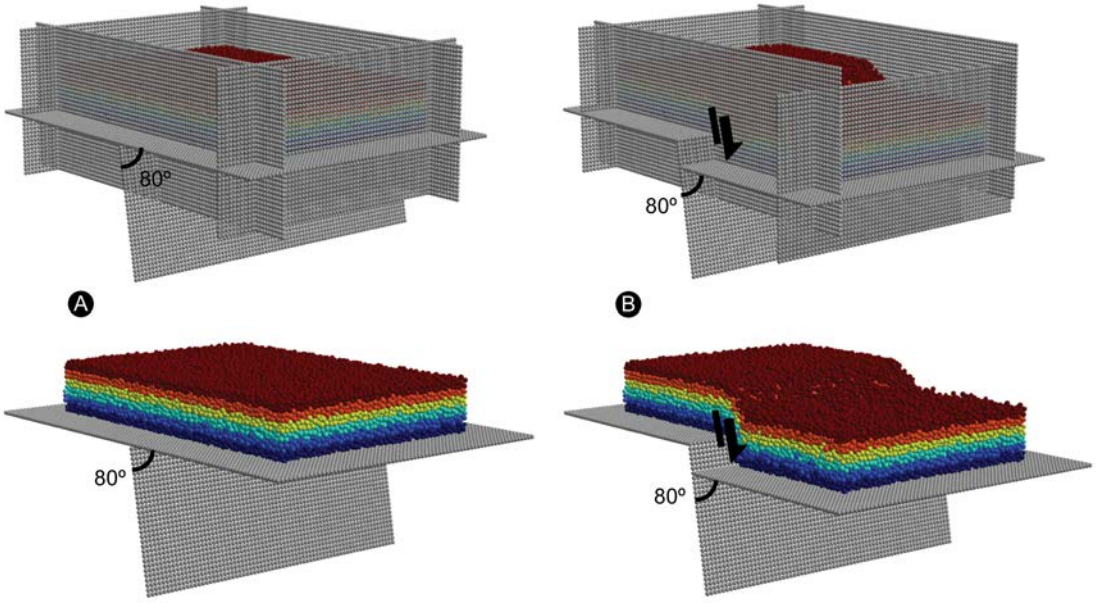

Figure 2.1.2. Example of boundary conditions defined in the bounding box confining a DE assemblage. In this example, an extensional normal fault dipping 80º is defined. The picture shows the bounding box and the base wall of the bounding box with the DE assemblage in their initial (A) and final (B) positions. The deformation of the DE assemblage can be appreciated in the last stage. In the lower images only the base of the bounding box is represented in order to show the DE assemblage.

2.1.3.1 Scaling

An important part of the discrete element methodology concerns how to scale, or set, the different variables in the equations, in order to obtain the desired deformation of the upper crust materials. DEM follows the same principles that Mora and Place (1993, 1994) and Mora et al. (2002) applied in their models.

The mass corresponding to one sphere of the assemblage is calculated by assuming that the particles are packed following a 3D cubic face centred lattice. The mass of a particle is given by

$$M_i = \rho \frac{\sqrt{2}}{2} D_i^3$$

Equation (2.1.6)

M_i - Mass of the particle i

ρ - Density of the material that the DEM is modelling

D_i - Diameter of the sphere

The forward time step is defined to ensure numerical precision and a stable numerical integration. If we consider the velocity of the waves P as the maximum speed of information propagation, the forward time step for the DEM is defined as follow:

$$\Delta t = 0.2 \frac{D_{min}}{V_p}$$

Equation (2.1.7)

D_i - Diameter of the sphere

V_p -Velocity of the waves P

Finally, the spring constant K, which defines the elasticity of the particle, is approximated by Eq. 1.2.8 in order to avoid collapse between spheres, also considering the maximum wave speed:

$$K = \left(\frac{8M}{9}\right)\left(\frac{V_p}{D}\right)^2$$

Equation (2.1.8)

M - Mass of a particle

V_p -Velocity of the waves P

D- Particle diameter

2.1.3.2 Time scale and time steps in DEM

Despite the fact that DEM needs to define a time step discretization and a total simulation time, neither the time steps neither the total time represent the geological time scale in which such a structure is formed/deformed. The forward modelling time steps are

chosen to ensure numerical stability of the model according to its scaling, and the total time is just the value that provides the number of time steps to achieve a desired final situation.

2.1.4 DEM outputs and representation

DEM saves information at pre-established time steps of the simulation time, from which an evolution of the DE simulation can be examined.

The output files can be easily represented by 'DataTank', a tool to visualize numerical data. At each time step, the discrete elements can be represented in their new position coloured by sizes (fig. 2.1.1), layers or facies (fig. 2.1.3 A and B). The layer representation is only an initial geometric layout of the model, where the different layers do not represent any mechanical property, but whose evolution allows us to accurately visualize the deformation, from its initial position to its final position. In the facies representation, each facies will represent different mechanical properties of the DE such as cohesion or internal coefficient friction.

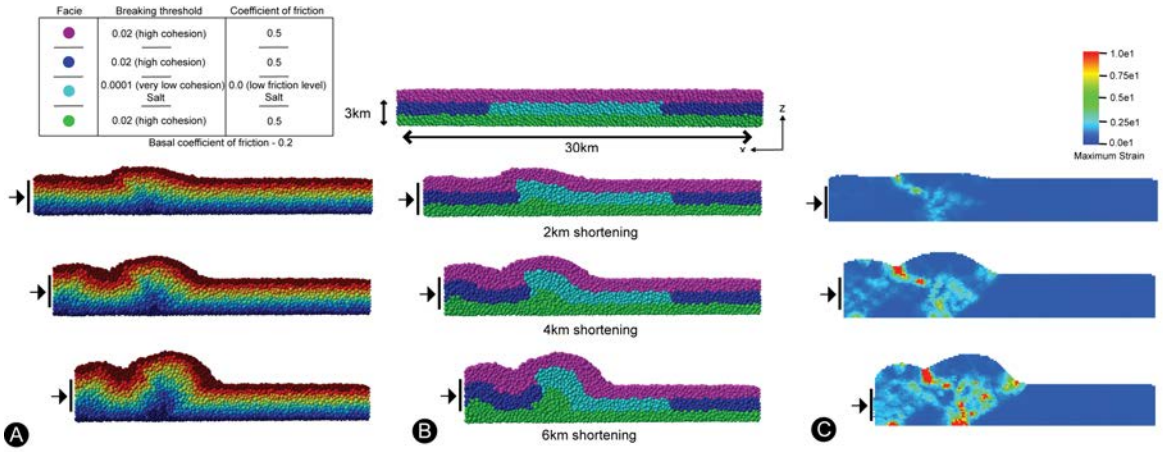

Figure 2.1.3. Cross-section of a DE model in three different time steps of the simulation. The results are represented using the program 'Datatank'. Discrete elements are coloured by: A- layers (without any mechanical property and just for a visualization purpose; B- facies (according to the mechanical information); and C- the maximum shear strain values calculated by the SSPX programme.

Another manner with which to represent the DEM assembly deformation is by using the SSPX program (Cardozo and Allmendinger 2009). In this case, the Maximum Shear Strain is calculated using SSPX, which is an application to compute strain from displacement/velocity data in two and three dimensions. The maximum shear strain is calculated from the displacement between the particles (fig 2.1.3C) and it allows us a proxy for geological deformation. For details of the calculation see Cardozo and Allmendinger (2009).

2.1.5 Limitations of DEM

In the 2D and 3D configuration of DEM, new DE can be introduced into the model during the simulation, if this option is activated. These new DE can act as new sediments, representing new syntectonic sedimentation. However, these new sediments are homogeneously distributed and infilling all the available accommodation space without any physical (transport and sedimentation) process and without representing any lithological property. This type of syntectonic sediment addition could be sufficient in that case where the lithological information or the sedimentary architecture is not relevant. However, to add realism as well as accuracy to the results, sedimentological processes must be considered for the incorporation of syntectonic sediments into the model. Thus, new scenarios can be simulated and investigate, for example by playing with different source area location, or considering different sedimentation rates or different sediment types, among others. It is clear that having a realistic model of sedimentation providing input to a discrete element model will allow us to simulate much more realistically 'real' geological scenarios and to compare the simulations results with outcrop data.

2.2 SFM TO MODEL STRATIGRAPHIC ARCHITECTURE AND FACIES DISTRIBUTION OF A SEDIMENTARY BASIN

2.2.1 Introduction to process-based numerical models

There are different criteria to classify the sedimentary numerical models: forward or inverse; stochastic or deterministic; and process-based or structure-based among others. For more detailed information, the reader is referred to Gratacós (2004), where a comprehensive dissertation is made about the classification of the sedimentary models as well as the advantages and limitations of each model type. Specifically, the SMF program can be classified as a *process-based numerical* model. Process-based numerical models are widely used to analyse the sedimentary basin formation, since they are useful tools for the prediction and study of sedimentary facies distribution and depositional architecture. They assist with the understanding of physical, chemical and petrophysical characteristics within sedimentary bodies.

Process-based models use the physical laws that drive the different processes that take place in the basin, such as transport, deposition and erosion. Once the physical system that wants to be modelled is understood (*conceptual model*), it is translated into a mathematical equation or a system of equations (*mathematical model*), which will be numerically solved using different mathematical technics (*numerical model*). These process-

based models are also classified inside the forward numerical model category. Process-based models analyse the evolution of the interaction of the different processes to produce sedimentary results through a sequence of time steps starting from a particular initial situation.

The solutions or results obtained to solve these equations can reproduce the temporal and spatial evolution of a sedimentary basin, as well as the interplay among various factors, which are contributing or influencing the formation of the aforesaid basin. For example, the changes in the topography in a subaquatic system produce changes in the bathymetry. Consequently, topographic changes also produce fluid velocity variations, which affect the transport and deposition of the suspended materials. At the same time, the concentration of this suspended clastic sediment can benefit or harm the growing of a certain carbonate producing organisms, therefore can influence the presence of carbonate deposits in the basin.

Forward based-process numerical modelling can provide a wide range of information in a relative quick way, allowing the analysis of different experimental results just by varying a few parameters.

As mentioned earlier, the sedimentary model used in this thesis is known as Simsafadim (Simulation of stratigraphic architecture and facies distribution model). This is a process-based numerical forward model, which simulates in 3D clastic transport and sedimentation including processes of carbonate production, transport and sedimentation. Simsafadim is a useful tool to model efficiently the facies distribution and depositional architecture in sedimentary basins.

2.2.2 Background of Simsafasim

The first version of Simsafadim was developed by Bitzer and Salas (2001). These authors present a 2D model of Carbonate-Clastic sedimentation. The production of carbonate sediments is represented through the evolution of carbonate producing organisms using a 'predator-prey' ecological model. The program introduces the relationship between carbonate producing organisms and clastic sediments, but it deals just with one clastic-carbonate material, produced by the system itself. One year later the same authors (Bitzer and Salas 2002) introduce the program Simsafadim, which is an extension of their previous work to a 3D model. Simsafadim can simulate in three-dimensions the architecture and facies distribution of carbonate sediments. Gratacós (2004) introduces a new 3D code version named Simsafadim-Clastic (or SFM). This code introduces an improved version of the mathematical model for sediment transport and sedimentation as

well as their affection on carbonate production. Moreover, Gratacós (2004) introduces two extra features: 'the mass balance control' to guaranty the conservation of the mass volume of the system and a coherent time step discretization to ensure numerical stability results. The program has been applied successfully to different case studies (Gratacós et al. 2009a, 2009b).

Later on, Clavera-Gispert et al. (2016), includes new extra features in SMF such as an improved version of sea-level changes, the incorporation of the modelization of an unlimited number of clastic sediments and the possibility to consider subaerial nodes. Clavera-Gispert et al. (2016) also makes an in-depth update of the carbonate production model, in order to include an ecological model which considers new factors that can affect the carbonate production, such as the water depth, light, presence of nutrients, basin slope topography, etc. At the same time, the work also performs a comprehensive review of the code, updating it to Fortran 90, improving the algorithms and structure of the code. These improvements successfully manage to make the code much more computationally efficient.

An extensive exposition of the basis of SFM is given in Gratacós 2004, and Clavera-Gispert (2016). Nevertheless, a brief description of the main characteristics of Simsafadim's models and methods are given below, with the objective to provide the reader with the main tools to understand the methodology adopted in the thesis.

The version of SFM provided by Gratacos (2004) is the firts version of SFM to be implemented in the new merged code (SFM-DEM) to model syntectonic sedimentation (chapter 3). Later on, the merged code (SFM-DEM) is updated with the new version of SFM (chapter 4) improved by Clavera-Gispert (2016).

2.2.3 Conceptual, mathematical and numerical models of SFM

The main processes that SFM simulates are transport, clastic sedimentation as well as to carbonate production. Nonetheless to start the transport process, the system needs to define an initial fluid flow over the basin.

The fluid flow system used by Simsafadim was proposed by Bitzer and Salas (2002). It is a bi-dimensional transient potential flow model (Eq. 2.2.1), where the fluid flow moves from higher to lower potential values. The fluid flow system assumes a laminar, non-viscid and irrotational fluid. It does not consider changes in flow rate due to changes in density or salinity, neither due to short-term events. In a certain position of the basin, the value of the fluid flow velocity is determined by its bathymetry, and it is constant along the water column. Even though the program does not consider short-time processes, neither changes

of fluid flow with depth, a minimum water depth can be defined where no sedimentation occurs due wave action.

$$\frac{\partial}{\partial x}\left(T\frac{\partial h}{\partial x}\right)+\frac{\partial}{\partial y}\left(T\frac{\partial h}{\partial y}\right)+q-\frac{\partial h}{\partial t}=0$$

Equation (2.2.1)

h - Potential head

T - Transmissivity

t - Time

q - Source fluid term

x, y - Spatial cartesian coordinates

The objective of the fluid flow model is to define the general trend of the velocity fluid flow in order to establish the transport and distribution of sediment inside the basin. Although the model is quite simple, it allows us to accomplish its main aim adequately, and also simulate long geological time scales in reasonable computing time.

Once the fluid flow system is established, the transport of the sediment is calculated. The inflow of sediment into the basin is defined through pre-established nodes. The transport model assumes that the sediment is transported in suspension, following the pattern of the fluid flow velocity distribution, which it means that sediment is transported mainly by advection processes. The model also includes transport mechanisms of diffusion and dispersion. The diffusion at each point of the basin is conditioned by the water depth, but its value is constant along the water column. Both mechanisms, diffusion and dispersion, aim to reproduce the transport of materials due no-advective processes. The suspended sediment is also uniformly distributed in the water column, regardless its size-grain, in order to better simulate a turbulent transport rather than a laminar flow. Taking into account the three mentioned mechanisms involved in the mass flow, the transport equation for each sediment type can be represented by:

$$\left[D^{*}\left(\frac{\partial^2 C}{\partial x^2}+\frac{\partial^2 C}{\partial y^2}\right)\right]+\left[\alpha_x\frac{\partial^2 C}{\partial x^2}+\alpha_y\frac{\partial^2 C}{\partial y^2}\right]-\left[v_x\left(\frac{\partial C}{\partial x}\right)+v_y\left(\frac{\partial C}{\partial y}\right)\right]=\left(\frac{\partial C}{\partial t}\right)$$

Equation(2.2.2)

D - Diffusion coefficient

α_x, α_y - Dispersion coefficients in both directions, x and y

v_x, v_y - Lineal velocity of the fluid flow in both x and y directions

C - Concentration of sediment in the water column

The transport equation gives the concentration of different types of sediment in the basin. Once the concentration is obtained, the settling of the different materials is calculated. The sedimentation of each clastic material type is directly conditioned by its grain size and density and the flow linear velocity. Each material is characterized according its grain size by its critical settling velocity and its theoretical settling rate. The critical settling velocity is the upper threshold velocity, below whom, the material is able to settle. The theoretical settling rate is the settling velocity of the material when the fluid flow velocity is zero. The final settling velocity of each material is defined as a linear dependence between the fluid flow linear velocity, its critical settling velocity and its theoretical settling velocity. The mathematical equation for the sedimentation of each clastic material type is expressed as follow:

$$\frac{dC_{di}}{dt}=f_{di}C_i$$

Equation 2.2.3

C_i - Concentration of sediment type 'i' in the water column

C_{di} - Thickness of type sediment 'i' deposited in a time step

f_{di} - Deposition factor, which is a function of the theoretical settling velocity, water depth and a velocity factor, scaled between 0 and 1, and which depends on fluid flow velocity and the critical velocity for deposition (Bitzer and Salas, 2002.

The modelled area is discretized into a triangular finite element mesh (fig. 2.2.1). These elements and their nodes are the basis to solve the differential equations that manage the fluid flow and transport and sedimentary processes. The spatial discretization is

performed accordingly the inhomogeneities that are expected in the system. Nonetheless, the stability criteria of the numerical solution have also to be taken into an account when performing the spatial discretization. These criteria are detailed below.

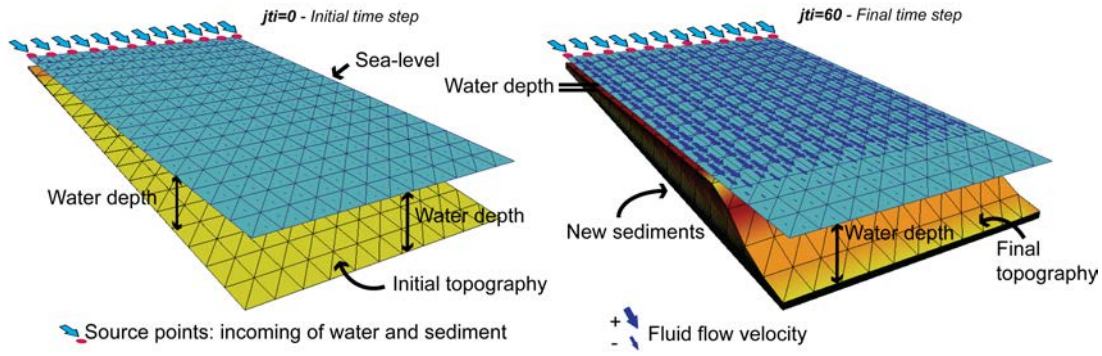

Figure 2.2.1. Simple simulation of SFM represented at the initial, jti=0, and final, jti=60, time steps. For both time steps, it is represented the topography of the basin, discretised in a triangular finite element mesh, as well as the sea-level position. Red dots indicate the source points for the incoming of water and sediment. The direction and magnitude of the fluid flow velocity are also represented by blue arrows. Note the higher velocity at the final time step, jti=60, due to the sedimentation and the resulting new bathymetry.

The Galerkin-finite-element method using linear interpolation functions is applied to solve both fluid flow and transport equations (Kinzelbach, 1986). The application of the method results in a system of ordinary differential equation with respect to time. The time derivative is discretized using the difference method. The system can be solved using any of the three schemes; explicit, implicit or a Crank-Nicholson scheme (Kinzelbach, 1986). The latter is an hybridization of the explicit and implicit schemes, which allows a second order accuracy.

In order to avoid numerical errors and overshoot solving the different equations, and to obtain reasonable results, several stability criteria for spatial and time discretization must be considered.

In relation to space discretization, it has to be taken into account that the characteristic size a finite element should not exceed the longitudinal dispersivity in order to control numerical dispersion. Also, to guarantee accuracy of the results independently of grid-orientation, discretization has to be in the order of magnitude of the transverse dispersivity for large ratios (α_L / α_T).

The forward time steps are defined according the Courant-criterion (Courant et al. 1967 [1928]). The time step is determined by the fastest process in the basin, transport or sedimentation, in function of the fluid flow velocity, settling velocity and spatial

discretization (Gratacós, 2004). When the system is transport-dominated, the maximum distance that a particle can travel is the distance between two consecutive nodes of the triangular mesh, therefore the time step (***dt)*** is conditioned by mesh spacing and the fluid flow velocity (Eq. 2.2.4). When the system is sedimentation-dominated, the maximum distance that a particle can travel is the water depth, so the time step will be now determined by the current water depth and the settling velocity of a particle (Eq. 2.2.5).

- Time step when advection is dominant:

$$\Delta t_{Courant} = \frac{\Delta x}{v}$$

Equation (2.2.4)

Δx - Distance between nodes

v - Fluid flow linear velocity

- Time step when sedimentation is dominant:

$$\Delta t_{Courant} = \frac{W}{v_s}$$

Equation (2.2.5)

W - water depth

v_s - Settling velocity

The model checks both conditions for the entire FE mesh, and the smallest time step is chosen in order to guaranty numerical stability in the solution.

Initial and boundary conditions are also required to solve both equations.

The initial conditions for the fluid flow equation set an initial value of the piezometric height in all the nodes of the basin. For the transport equation, the initial condition is set defining a basin without sediment in suspension.

Regarding to boundary conditions, only two types of boundary conditions can be admitted for both equations. The first kind sets a potential value in the boundary for the fluid flow and a constant concentration for the transport equation. The second kind is defined by a specific value of the fluid flow (special case: boundaries without flux) and by zero dispersive-flux boundaries in the case of the transport equation. These boundary conditions can vary during the evolution of the model.

The sedimentation equation is easily solved in each node of the FE mesh using the Euler method, which does not cause instability problems neither important numerical errors.

The carbonate production model used by SFM is an ecological model, based on the Generalitzed Lotka-Volterra equation that includes logistic growth and interaction among species (Clavera-Gispert et al., 2016 in press). Logistic growth of the species is constrained by environmental parameters such as: (1) presence of clastic sediments in suspension; (2) nutrients; (3) water depth; (4) energy of the medium; and (5) slope of the basin topography. These environmental parameters are converted to individual factors and finally combined into one single environmental factor that determines the evolution of species. Once species association population is computed, carbonate production is calculated using a carbonate production factor. Production factors are specified for the maximum population, and then linearly scaled to the real population.

This part of the SFM code with the carbonate model it has not been included yet in the new merged code. Therefore no father information about carbonate model is given here. For a more detailed information, the reader is referred to: Bitzer and Salas, 2002; Gratacós 2004; Clavera-Gispert et al. 2012, Clavera-Gispert et al. 2016 in press, Clavera-Gispert 2016).

2.2.4 SFM outputs and representation

Results in SFM are stored at pre-established time steps ***(jti)***. These time steps should be chosen in function of (1) the heterogeneity that can be expected, and (2) the desired discretization in the sedimentary record (one stratigraphic unit corresponds to one time step *jti*). For smaller time steps, a more detailed stratigraphy is obtained. This time step should not be confused with the time step ***dt*** discretization used to solve the numerical model (see section 2.2.3) that is obtained automatically during the simulation.

Thus, the results can be easily represented at each time step *jti* in order to reproduce the sedimentary record. The main parameters that can be represented are: the fluid flow velocities (fig. 2.2.2 A); the concentration of each sediment type in suspension in the water column (fig. 2.2.2 A); and the total amount of sediment deposited (fig. 2.2.2 B). Specifically, for each sediment type, it also can be represented the sediment percentage (defined by the amount of each clastic sediment type deposited in one time step in relation to the total sediment thickness deposited at the same time step); and the dominant sediment type (where the elements of the mesh are coloured in function of the most common sediment type) (fig. 2.2.2 B).

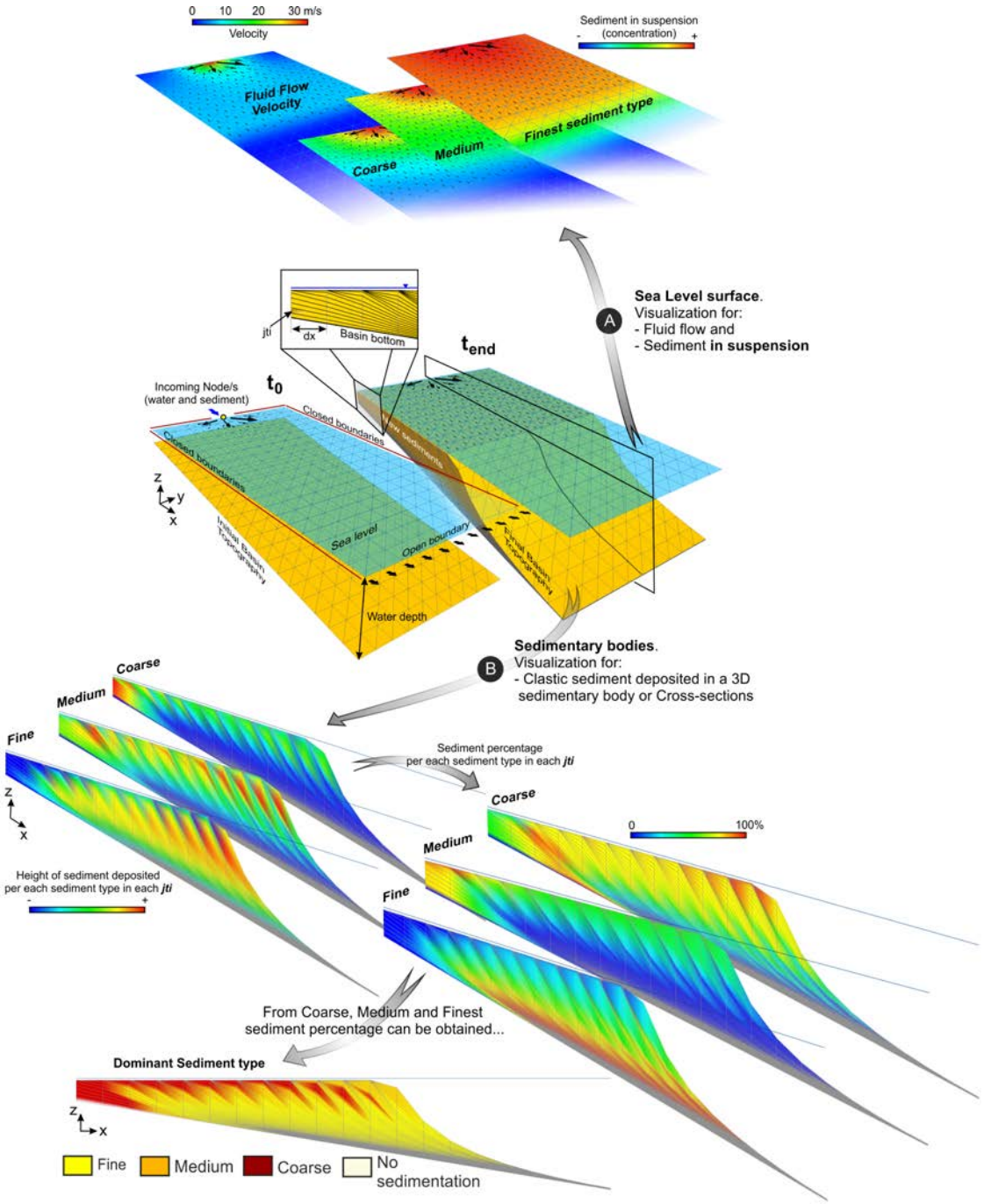

Figure 2.2.2. Visualization of the results of a SFM simulation. A- Initial and final topography of a basin with the sea-level position and the corresponding fluid flow velocities. Sediment concentration in suspension is also represented for 3 different clastic sediment types. B. Sedimentary bodies coloured by the sediment thickness deposited in each node at each time step. . The sedimentary record is also coloured according the sedimentary thickness of each sediment type, and also according the facies distribution, which represent the most abundant clastic sediment deposited in each node.

The output files can be easily represented by (1) 'DataTank', a tool to visualize numerical data, that here is used to represent the evolution of the sedimentation patterns of the different sediment types, the concentration of each sediment type and fluid flow; and (2)

'ParaView', an open source visualization application, which allows a complete representation of the sedimentary model evolution (fig. 2.2.2).

2.2.5 Limitations of SFM

The current version of SFM does not include changes in the topography due to deformation processes. The program just allows a vertical movement rate in a specific node/s and it can be easily implemented by the user with a predefined value, being this definition of the movement not as consequence of any deformation process. The upper crustal Earth is continuously undergoing strain and deformation due the tectonics movements, which consequently are changing the basin topography where the sedimentary processes take place. This deformation factor can be relevant when the simulations are done throughout both short or long geological time scales. Therefore, in most cases, it is relevant to take in account changes in the bathymetry due to real deformation processes to have a better control of the resulting sedimentation, and thus, to obtain a more realistic depositional architecture of the sedimentary bodies and the facies distribution.

CHAPTER 3

COUPLING MECHANIC AND SEDIMENTARY PROCESSES

The process of combining the DEM and SFM models and their respective codes has been divided into three main phases. The following sections describe each of these phases.

3.1 INITIAL PHASE - FIRST STEPS BEFORE COUPLING

This phase is related to the essential tasks completed prior to combining DEM and SFM. This first phase has been focussed on three main tasks: the study of the respective models and their modelled processes; the unification of the codes in a single programing language; and finally, the search of potential strategies to combine both models.

3.3.1- Studying the respective models, SFM and DEM.

This first task has focussed on:

- Studying the geological processes modelled by both, SFM and DEM (see previous chapter 2 for an detailed information):

  SFM: focuses on the study of sedimentary processes that take place in a subaquatic environment, such as fluid flow, and sediment transport and sedimentation of clastic materials, as well as the physical principles controlling each process. The program allows to study the 3D sedimentary bodies and its stratigraphic architecture, as well as, the resulting heterogeneity.

  DEM: Studying the processes of deformation into the upper crust, which derive from tectonic movements: fault propagation, fold formation, fault propagation-folding. Studying the mechanical behaviour of different materials that form the upper sedimentary cover (brittle materials, with and without cohesion...) and how they are deformed under stress.

- Studying the numerical techniques and mathematical methods that underpin each model as well as the equations that govern each process: the *discrete element technique* (in DEM), which manages the movement of assembly of the spheres; and the *finite element method* (in SFM), which is used to solve the differential equations of fluid flow and transport (the reader is also referred to chapter 2 for more information).

- Studying and analysing both respective numerical codes in order to become familiar with their different main variables and functions, as well as their algorithms and their respective flow charts (fig. 3.1.1).

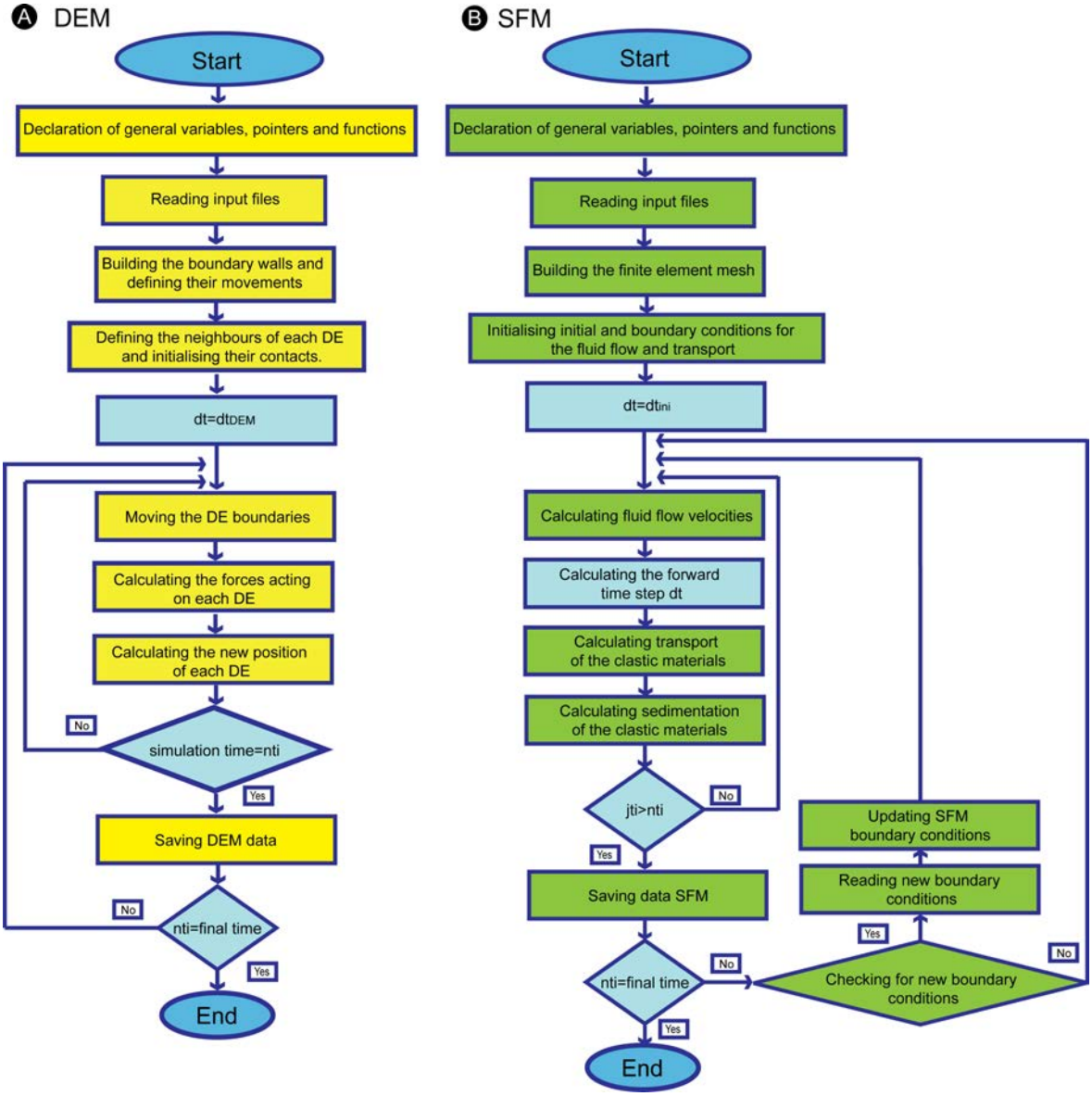

Figure 3.1.1. Flowchart showing the workflow of the DEM(A) and SFM(B) codes.

3.1.2- Unifying the different codes in a single computer language.

The first version of SFM to be implemented with the new syntectonic sedimentary model (see chapter 2), is written in Fortran 77. On the other hand, DEM is coded in C language. The necessity to have all codes in a single computer language arises from two different aspects:

- Computational time.

There are software interface tools that can combine different codes, functions or subroutines in different languages. However, the resultant executable program

requires longer computational time. Since computational time is already a significant issue for both models, it is paramount not to worsen the problem when merging the models in a single code. Hence, the unification of the codes in a single structure and a single computer language is deemed as the most efficient approach to merge the models.

- Easy manipulation of codes and their variables.

There are software packages capable of translating automatically a code from one computer language to another. The compiler can compile the new translated code without problems and the resulting executable is supposed to yield good results (but this last premise has not been tested). Nonetheless, the resulting code is non-treatable in terms of language, variables and structure, because the translator tool works only to be understood by the compiler, but not by the user. Hence, this option is not considered here, since there is a need for directly interacting with both codes, their algorithms and variables.

After the above mentioned considerations, it was decided that a single language for both codes will clearly best facilitate the work of combining the two models, and it would also provide the most efficient computational platform.

The chosen programing language to build the new code is the C language. C has proven to be quicker than Fortran 77 in terms of computational time, since it allows the variables to have direct access to the memory, if they are properly defined (pointers). Therefore the SFM code has been translated to C language.

Both C and Fortran languages are imperative procedure languages that use similar flow control, structures and functions to develop the code. Therefore, the translation from Fortran to C has not been extremely difficult. Nevertheless, it was a long and tedious task, albeit essential for the efficient merging of the models. Moreover, the task allowed to scrutinize and comprehensively *debug* the SFM code. This revision results in a more efficient code architecture of the SFM, e.g. by eliminating GO TO structures and some repetitive loops that could cause errors or increase computational times. The vectors and matrix variables are also replaced by vectors and matrices pointers, which allow for faster memory access. The latter significantly speeds up program execution and it also allows a dynamic memory reserve.

3.1.3 Discussion: the best coupling technique.

The main issue that arises when facing the merging of the models is that each model is based in completely different mathematical and algorithmic technique. SFM is a process-based model, which discretises the initial basin topography in a triangular finite element mesh and uses the finite element method to solve the main equations for fluid flow and sediment transport. DEM uses the discrete element technique to model the rock mass. The former model has a Eulerian specification, which, in simple terms, means that the calculus of fluid flow and transport are focused on specific locations, i.e. the nodes of the finite element mesh. The latter is a Lagrangian system, where the individual discrete elements are followed through position and time.

But independent of their respective methodologies, if we look at the environments where each processes operate, we can see that their settings are completely distinct: i.e., deformation takes place within the upper crust whereas sedimentary processes take place in a subaquatic system.

Despite this fact, there are two clear links between the two models. Specifically for a sedimentary basin, the first link can be found in the water-sediment interface that in this model is represented by the DEM surface. This surface will evolve as a result of the deformation that is affecting rock mass. The surface of DEM shapes the bottom topography of the basin. The evolution of this topography will modify the bathymetry of the subaquatic system contained by such a basin. Consequently this evolution will affect the processes that take place inside the subaquatic system. Hence, SFM only needs to consider the changes in this topography to modify accordingly the processes of fluid flow, sediment transport and sedimentation. Therefore, the basin topography considered by SFM will evolve as a consequence of the deformation produced by DEM and the sedimentation produced by SFM itself.

The second link is found in the syn-sedimentary unit, that in the new model is represented by the sediment settled in a specific time-step using SFM. The new deposited sedimentary unit is contributing to the thickness of the sedimentary cover. Under an active tectonic system, not only the initial sedimentary basin can be deformed accordingly, but also the syn-sedimentary unit. Thus, the new syn-sedimentary unit obtained from SFM must be added to DEM in order to be deformed according to the deformation that the basin is undergoing.

If these new sediments can be incorporated into DEM, which means updating the amount of sediment deposited as new discrete elements, a feedback is achieved. Firstly, the

syntectonic sediment will be deformed according to the deformation model. Secondly, since this new syntectonic unit is incorporated into DEM as new discrete elements, they are not only being deformed, but also interacting with the pre-tectonic unit, thus taking actively part in its deformation.

As a result of these two feedback links, combining both codes will not involve redesigning the modelled processes, neither the mathematical methods nor the numerical techniques used in each model. Each model will continue performing within its own environment, but will be updated with the information provided by the other model.

The following section details how the bathymetry of SFM will change in response to the deformation model, implying the adaptation of the triangular mesh to the surface movements of DEM, and how the new sediments are included and assimilated by DEM, in order to be affected by the deformation processes.

3.2 SECOND PHASE - IMPLEMENTATION: COMBINING DEFORMATION AND SEDIMENTATION MODELS

Once the conceptual links between the two models, DEM and SFM, have been established, the next step to perform is the design and construction of the new code.

This process is divided in three main stages, which are described in the following sections:

3.2.1. Shaping the sedimentary basin: Adapting the finite element mesh of SFM to the movements of DEM surface.

In the new model, the surface of the DEM will condition the initial topography of the sedimentary-modelled basin. Therefore, the triangular finite element mesh used by SFM to solve the equations of fluid flow, transport and sedimentation has to be 'located' over the DEM surface (fig. 3.2.1) and track its changes.

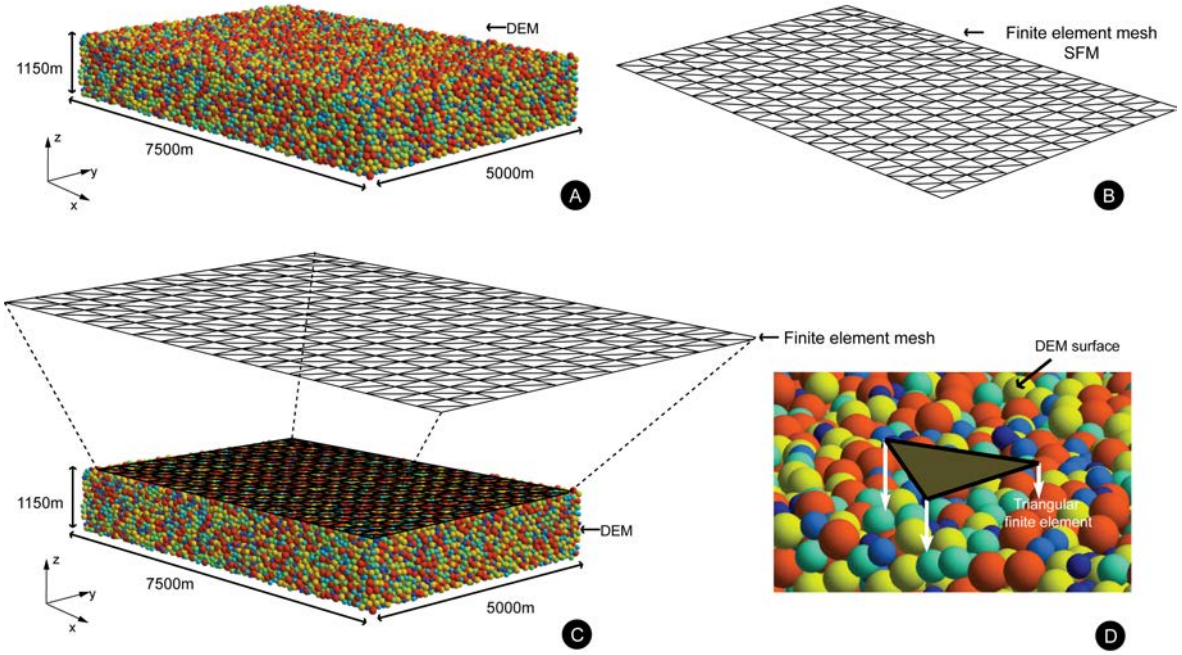

Figure 3.2.1. A- Example of an initial DE assemblage coloured by size. B- Example of an initial triangular FE mesh. C - Conceptual illustration on the FE mesh being located on the DE surface. D- Conceptual idea of one triangular element of the FE mesh, which is checking for the DE surface position. The irregularities of a surface made up by spheres can be also appreciated.

The process starts defining the nodes (coordinates *x,y*) of the FE mesh in function of the DE assemblage area, whose discretization will depend on the size of the model, and the heterogeneity expected for the system.

The *z* coordinate for each node of the defined FE mesh is obtained from the DEM surface. Therefore, first step requires us to define the position of the DEM surface to provide the consequent coordinate z value to each node. Nevertheless, defining the position of the surface is not straightforward, since DEM is built by randomly allocated spheres in the volume of the assemblage.

Thus, in order to define the surface of DEM, the DE assemblage (fig. 3.2.2 A) is divided in a 2D (x-y) fictitious square mesh whose elements have the size of twice the diameter of the largest DE spheres of the assemblage (fig. 3.2.2 B). The spheres contained in each volume, defined by the elements of the fictitious mesh, are checked, looking for the one with the highest *z* coordinate value; i.e. the sphere located at the highest point. The position of this latter set of spheres, one per element of the 2D fictitious square mesh (fig. 3.2.2 D), defines the shape of the DEM surface (fig. 3.2.2 C).

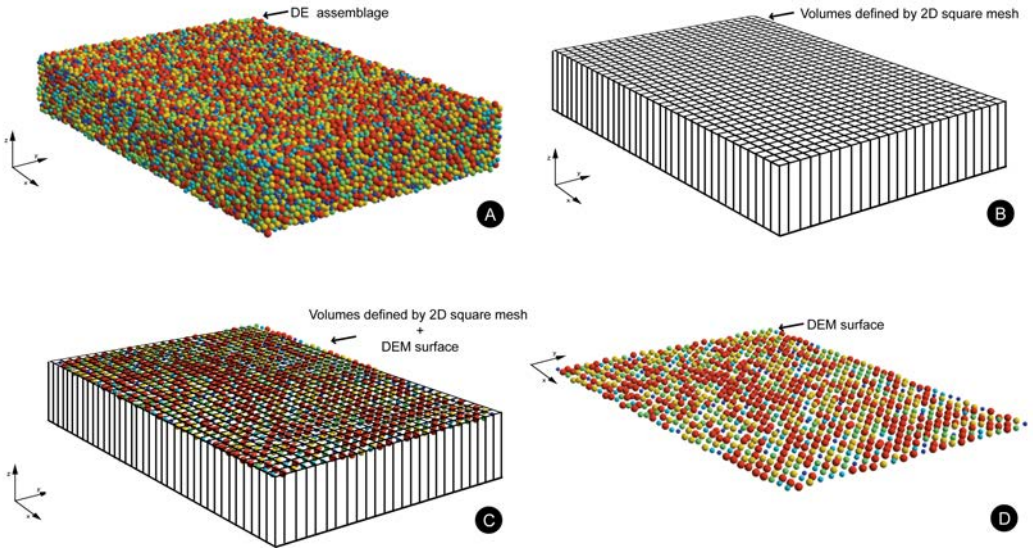

Figure 3.2.2. Illustration of the procedure to detect the DEM surface. A- Initial DE assemblage coloured by element size. B- Discrete volumes defined by a 2D square mesh, in which the DEM assemblage is divided. C- 3D visualization of the spheres that define the DEM surface. To localize these DEs, all the DEs belonging to each volume have been checked and the one located in the highest position has been chosen. D- Resulting DEM surface without the mesh for a better visualization.

Once the position of the DEM surface is defined, the next step is to transfer the corresponding ***z*** coordinate to each node of the triangular FE mesh in order to obtain the surface that will be used by SFM as a bottom topography of the sedimentary basin. Each node of the mesh checks the sphere of the surface of DEM located to its closer *x-y* position and the node takes the *z* value of the position of this sphere.

This procedure is performed at the beginning of the simulation, as well as at each subsequent time step. Therefore, the triangular finite element mesh will be updated as a result of the deformation produced by DEM, and the processes modelled by SFM will take into account such deformation.

The first problem encountered is that a surface made up by spheres is an irregular surface (fig. 3.2.1 D). Therefore the 'real' topography is sort of the average of the position of the highest spheres. This results because one sphere is not sufficient to shape the *z* position of each node. Therefore, the position of each node is ultimately determined not just by one sphere, but by the average position of the four spheres of the DEM surface located in the closest position of this node.

Although a ***z*** mean value is used, the final surface still having irregularities, small caves and bulges, not attributable to a real topography as a consequence of the DEM surface is derived from randomly allocated spheres with different radii. In the following

sections, this and another problem related to the working coordinates are introduced as well as, the solution proposed.

3.2.1.1 Irregularities in the DEM surface: Smooth filter

In order to minimize the aforementioned irregularities in the surface of the basin, a smooth filter is applied to the finite element mesh '*z*' coordinate. This filter works in the same way as an image-processing filter does to eliminate the 'noise' of a digital image (fig.3.2.3). The smooth filter used is similar to that of the 'weighted average linear filter' (Jain et al. 1995), which is a common digital filtering technique. This linear smoothing filter removes high-frequency components (noise), and the sharp detail in the image is lost. The smooth filter applied to the mesh has the same effect: the caves and bulges disappears while preserving the real average surface topography.

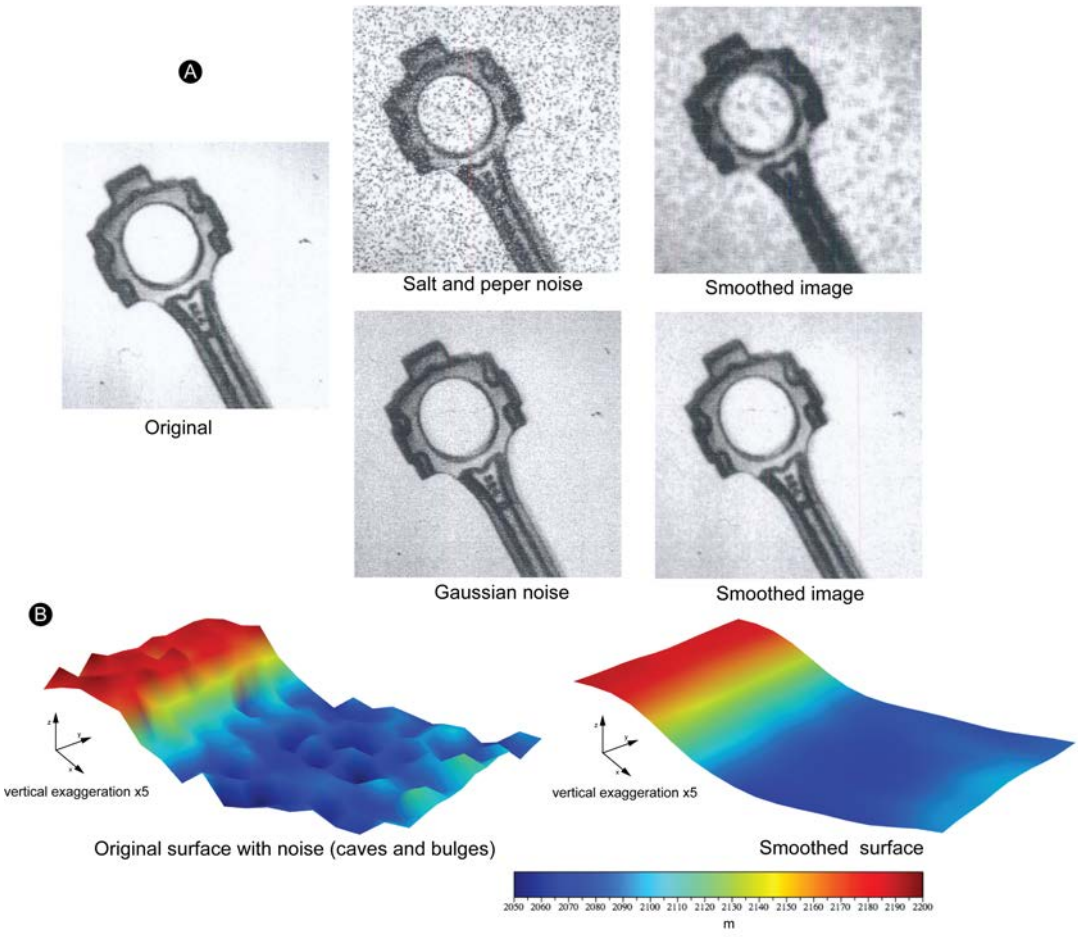

Figure 3.2.3. A- Left - original digital image. Centre - same image affected by two different types of noise (salt and pepper and Gaussian noise). Right - same images once a 'weighted average linear filter' is applied to eliminate the noise. B - finite element mesh after being located over the DEM surface: left - before and right - after apply the smoothing filter. It can be appreciated that the caves and bulges as a consequence of the irregularities of DEM surface, are smoothen while the 'shape' of the surface is kept.

Figure 3.2.3 A shows the same digital image before and after applying the 'median filter'. It can be seen how the 'noise' of the digital image disappears after applying the filter, and that this filtering does not modify the image.

Similarly, figure 3.2.3 B shows the mesh after being located over the DE surface. The caves and bulges consequence of a surface shaped by spheres can be easily appreciated in the left image. The right image shows the mesh after applying the smooth filter. In a similar way that the median filter blurs the noise in the digital image, the caves and bulges are also smoothen, but the overall 'shape' of the surface is preserved.

3.2.1.2 Working Coordinates

Another problem encountered when trying to merge both models is that each model is expressed in different ***z*** working coordinates. The initial basin topography of SFM is referred to the initial sea-level position, which defines the reference level in the zero value of the *z* axis. Therefore, the initial ***z*** values of the basin topography position are given by negative values (fig. 3.2.4 A). On the other hand, DEM is just an assemblage of spheres, which are randomly allocated in the space, and their position does not have any specific location.

Instead of transferring the coordinates of one model into the coordinates of the other model, (e.g., moving the DEM in a manner that its surface meet the coordinates of the topography of the basin with respect to the sealevel position), the merged model keeps the respective coordinates for each model. The problem is solved by establishing an internal reference in the code, $\boldsymbol{Z_{ref}}$, between the triangular FE mesh (Z_{SFM}) and the DEM surface (Z_{DEM}) that is obtained as follows:

$$Z_{ref} = Z_{DEM} - Z_{SFM}$$

Equation (3.2.1)

Once this reference is established, each model follows working with its own coordinates, and the merged model works as if the FE mesh was directly established over the DEM surface (fig. 3.2.4 B).

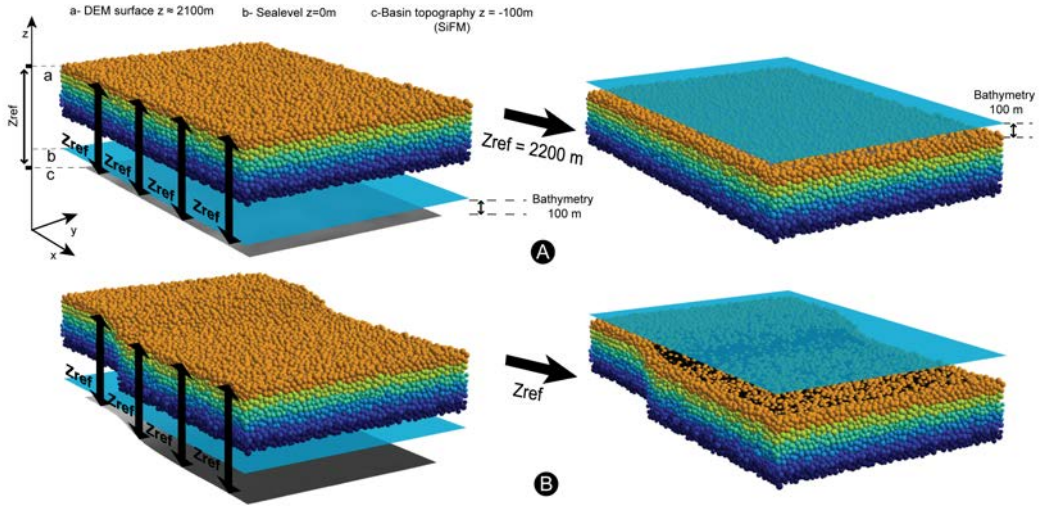

Figure 3.2.4. DE assemblage and SFM topography and the respective sealevel (A) in two different time steps of a model simulation. Each model is expressed in its own work coordinates. An internal reference is established between the triangular element mesh and the DEM surface. Once the reference is established (B), the model evolves as if the triangular FE mesh was directly established over the DEM surface.

3.2.2 Stability criteria: Time step discretization.

Both sedimentation and deformation models use different techniques and numerical methods to solve the equations that manage each process. To simulate both processes simultaneously, the convergence and stability of each model and their respective numerical methods must be guaranteed. Therefore, it is necessary to define an appropriate time step such that both models move simultaneously forward at specific time. Hence, the time steps must be compatible.

As explained in the previous chapter (section 2.2.3), the time discretization in SFM used to solve the fluid flow and transport equations is performed using finite differences. This method uses the Courant criterion for stability and convergence of the numerical solution. The time step can be calculated depending on whether the system is dominated by transport (Eq. 2.2.4) or sedimentation (Eq. 2.2.5) (Gratacós, 2004). The advanced time step in DEM (section 2.1.3) is constant for each simulation and it is also chosen according to a numerical stability criterion that ensures the accuracy and reliability of the results (Eq. 2.1.7). Nonetheless, as it is already argued in chapter 2, DEM time scale does not represent the deformation in real geological time scale, but a number of time steps that the model requires before it reaches the final situation.

In order to run the merged code, the new model takes, as a total simulation time, the total time given by SFM, since this model uses values at geological time scale. In this sense, the merged model scales the DEM total time in function of the SFM total simulation

time, and, accordingly, its time step, in order to be considered as the same as the modelled geological time with SFM (fig. 3.2.5). The objective is to achieve the desired deformation with DEM at the end of the simulation time considering a geological time-scale. This assumption, between the time scale of DEM and the geological time scale, allows the new model to run DEM and SFM simultaneously and to combine the sedimentary processes with the desired rates of deformation. Once this assumption is established, a specific function in the new code checks the three criteria for the time discretization, two for SFM and one for DEM. The stability of the models is ensured by fixing the advancing time step to the smallest time step.

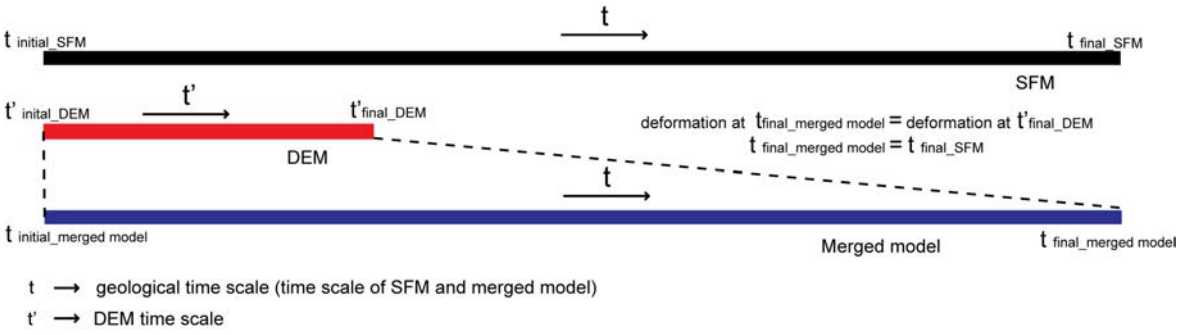

Figure 3.2.5. Conceptual diagram of the simulation time (geological time scale) in the merged model, in relation to SFM simulation time and DEM simulation time.

3.2.3 Sediment transfer between models

3.2.3.1 Previous considerations

There are three main issues, or considerations, to take into an account when attempting a sediment update from the results given by SFM to spheres (DE) in DEM. These three issues are imposed by the respective models, as well as the methodology adopted in combining these two processes.

The first issue relates to the size of the DE. In order to make an update between SFM and DEM, the amount of sediment deposited in an element of the SFM's mesh needs to have, at least, not only the volume, but also the height of a sphere of DEM, i.e., the diameter of a sphere.

A second issue lies in in the manner that SFM restores its topographic surface due to DEM deformation. In the merged model, the topography of SFM in a given time step is defined by the amount of sediment deposited and the deformation accrued in DEM. At each time step, the z component of SFM's mesh is updated with the new DEM surface values by means of the process described in Section 3.2.1. The position of this DEM surface needs to be well defined in order to detect variations between time steps. If new

spheres may be added to the DEM surface, due to sediment updates, the DEM surface needs to be re-defined. This process needs to be handled with special care, or else the new elements in DEM may be mistaken by surface movements.

On the other hand, SFM also needs to know the amount of sediment that has been transferred, in order to restore its topography accordingly.

The third issue is related to the deformation process of the syntectonic unit, which can only be performed by DEM. Thus, while sedimentation in SFM is not updated in DEM, this sediment will only undergo *z* direction movements according to the adaptation of the finite element mesh to the DEM surface. Therefore, the syntectonic sediment needs to be updated into the DEM as soon as possible in order that it can proceed with its own deformation.

The procedure developed to make the sediment transfer between models takes into an account these three considerations.

3.2.3.1 Procedure to perform the sediment transfer from SFM to DEM

According to the first issue described in the previous section, the sediment transfer from SFM to DEs takes place when the amount of sediment deposited in the model is higher than a critical value, i.e., when the amount of deposited sediment in a particular number of nodes is equal or larger than the diameter of a sphere.

The number of nodes will be determined as a function of the model size and the total number of the nodes on the finite element mesh. The objective is that all sediment data transfers occurring during a complete simulation would yield an increase of elements in DEM as close as possible to the deposition of sediments in SFM.

During the sediment transfer, the space taken up by the new sediment is refilled with new DEs. This refilling process aims to convert into DEs all the deposited sediment of the SFM model, which has been deposited up to the current time step; that is the time step at which the conditions to implement the sediment transfer data is satisfied.

Summarizing, the sediment transfer procedure works as follow:

A lamina of randomly allocated spheres of different diameters, with the same horizontal (*x-y*) size of the model, is created (fig. 3.2.6 B). Then, each sphere of the lamina checks its *z* component position over the DE surface, according to its *x-y* position. If the sphere is not higher than the height of deposited sediment, in its newly position in the DEM, and, at the same time, it does not overlap with other currently existing spheres in the model, the sphere is finally added to the DEM.

In order to assess if the height of the DEM model after the location of a new sphere is higher than the real topographic surface (i.e., DEM former surface plus new SFM sediment), the new sphere has to check to which element of the finite element mesh it belongs. Once the sphere knows the element at which it belongs, the z component of the topographic surface in its current x-y position can be determined. Consequently, the model can decide to permanently leave the sphere or remove it. In this way the shape of the DE assembly surface adapts to the shape given by the sediment deposited in the finite element mesh (fig. 3.2.6 F).

After checking the deposition of the DEs of a lamina, the DEM is left to equilibrated in order to assimilate the new syntectonic DEs: DEM then runs for a number of time steps without any displacement of the boundaries with the aim of packing and equilibrating the newly introduced sediment. With this process the new DEs are progressively integrated by DEM.

After the incorporation a lamina of the DEs into DEM, another lamina is created. Once more, the checking process for adding each sphere takes place and the spheres are placed in DEM accordingly. After placing the spheres, the DEM is 'equilibrated' one more time (fig. 3.2.6 D).

These three steps, creation of a lamina of spheres, placement of these spheres in DEM and equilibration of the DEM model, are repeated as many times as is needed: the sediment transfer from SFM to DEM is finished when no spheres of one lamine can be deposited, which basically means that the space occupied by the syntectonic unit has been filled with discrete elements (fig. 3.2.5 E and 3.2.5 F).

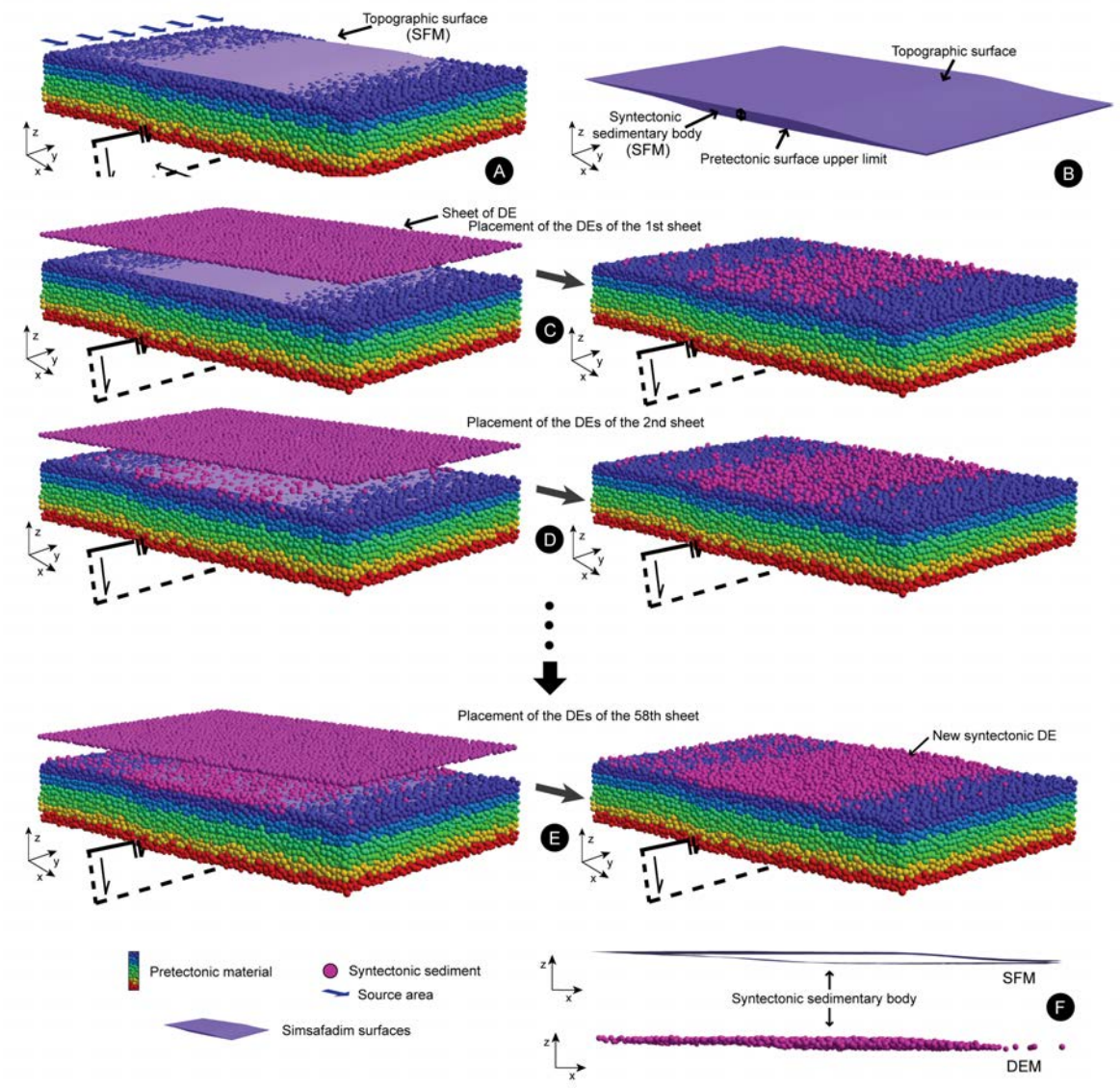

Figure 3.2.6. Sediment transfer procedure from SFM to DEM for the syntectonic sedimentation, e.g. in a normal fault. A- The pretectonic unit of DEM, plus the SFM topographic surface, just before the sediment transfer. The SFM surface is showing the real topography at the current time step. The gap between this topographic surface and the surface of DEM is the new syntectonic unit deposited till the current time step, when the condition for sediment transfer between both models is reached. B- Syntectonic sedimentary body that will be transformed from SFM into DEs. C- First step of the sediment transfer: the first lamina of DEs with the same area as DEM is created. Each sphere of the lamina is checked and is placed in the DEM according to the shape of syntectonic sedimentary body. Once all possible spheres of the lamina are added in DEM, they are compacted and equilibrated with the rest of the elements of the model. D- The first step of the transferring process is repeated again for a new lamina of spheres. This step will be repeated as often as necessary till the sedimentary body is completely filled with new DEs. E- DEM when the sediment transfer between models is finished. No spheres of the last lamina could be added to DEM. F- Lateral view comparing the new syntectonic unit in SFM and DEM.

Once the sediment transfer is finished, the finite element mesh is re-placed over this new DEM surface, and the values of deposited sediment used to restore the SFM topography are reset to zero. Once more, the evolution of the topographic surface will be a consequence of these new surface movements, plus the sediment that settles from now on. When the amount of sediment, which has been settled from the last sediment transfer to the current analysed time step, reaches once more the condition to undertake another transfer, all the processes for sediment transfer between SFM and DEM start again; and so on, till the end of the simulation (fig. 3.2.7).

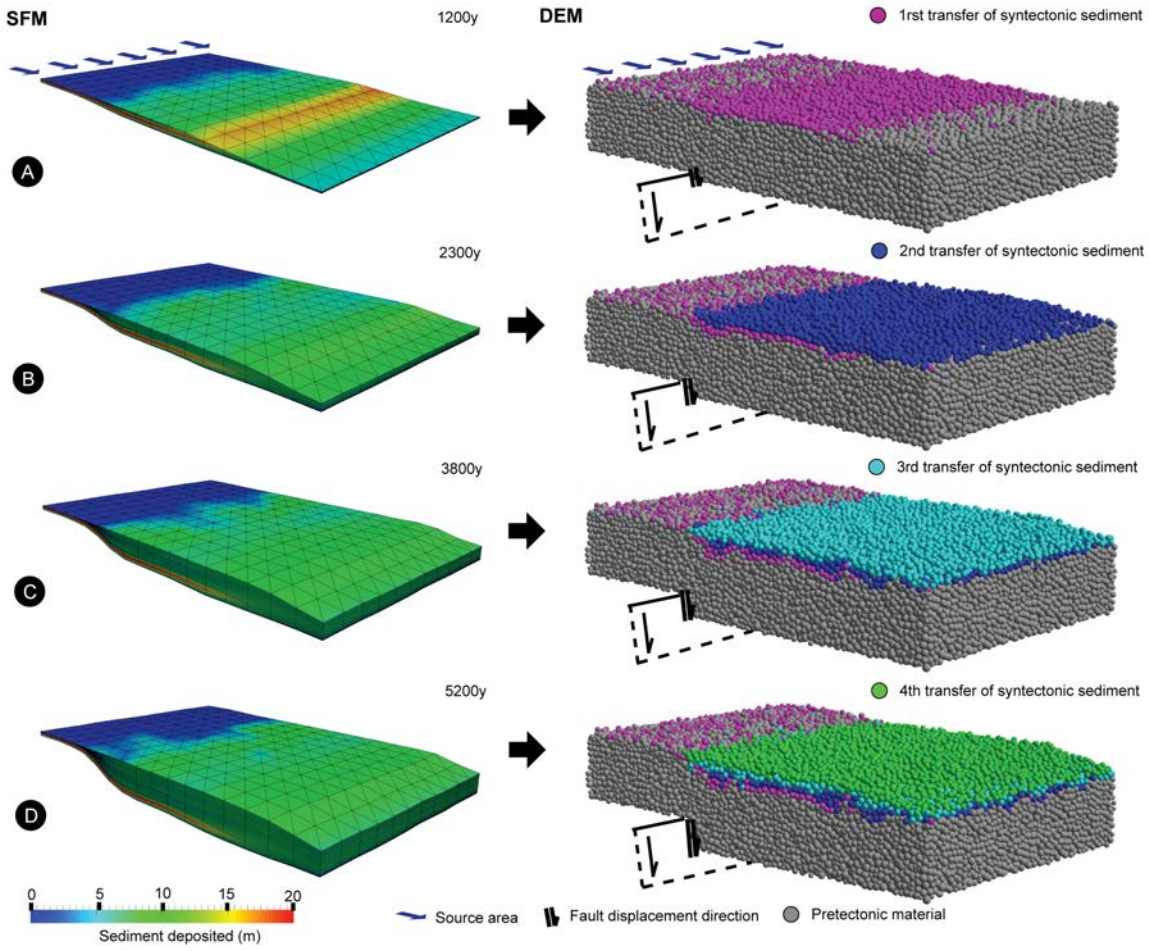

Figure 3.2.7. Example of a normal fault evolution with syntectonic sedimentation represented by SFM and DEM respectively. In this example, four sediment transfer have taken place during total simulation time at: (A) 1200y (B) 2300y (C) 3800y and (C) 5100y. Note how one transfer from SFM to DEM corresponds to several SFM time steps.

Due their diameter size, the new syntectonic DEs in DEM can summarise several time steps from SFM (fig. 3.2.7). The new spheres represent the related SFM sedimentary bodies and can store some properties from them (fig. 3.2.8). In this sense, each DE stores: (i) the total sediment deposited in the element of the mesh where the DE has been placed;

(ii) the percentage for each sediment type (fig. 3.2.8 C); and (iii) the representative facies (fig. 3.2.8 B) defined by the sediment with a higher percentage in the area.

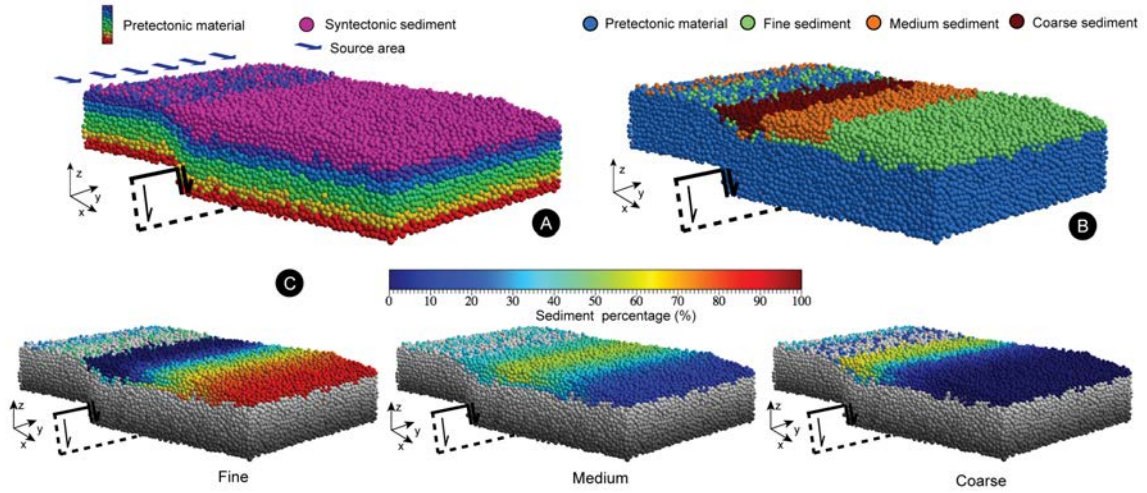

Figure 3.2.8. DEM representation of the syntectonic sedimentation considering a normal fault at the end of the simulation time (intermediate time steps of the same simulation are already introduced in the figure 3.2.6 and 3.2.7). A- The DEM showing in pink the new syntectonic DE unit, which represents the sediment added during the simulation time. B - Syntectonic unit coloured by facies, which represent the most abundant sediment type of the deposited sediments. There are three different sediment types introduced in the model, defined as coarse-, medium- and fine-grained sediment. C- Syntectonic DEs coloured according to the sediment percentage of each sediment type.

When a sediment transfer takes place, the syntectonic sediment is then fully part of the DEM. This allows a double interplay in the DEM model. On the one hand, this syntectonic material will be deformed according to the deformation model. On the other hand, this new material is now interacting with the pretectonic cover, and therefore, it could influence its deformation pattern. Hence, a more realistic study of the deformation of this new syntectonic material and also the pretectonic cover could be performed.

3.2.4 Workflow for the merged code

Once the conceptual model that links the two models are defined, the new unified model must be coded in order to include the new functions and relationships between each model. The general workflow of code of the new deformation and syntectonic sedimentary model is illustrated in the flowchart of figure 3.2.9:

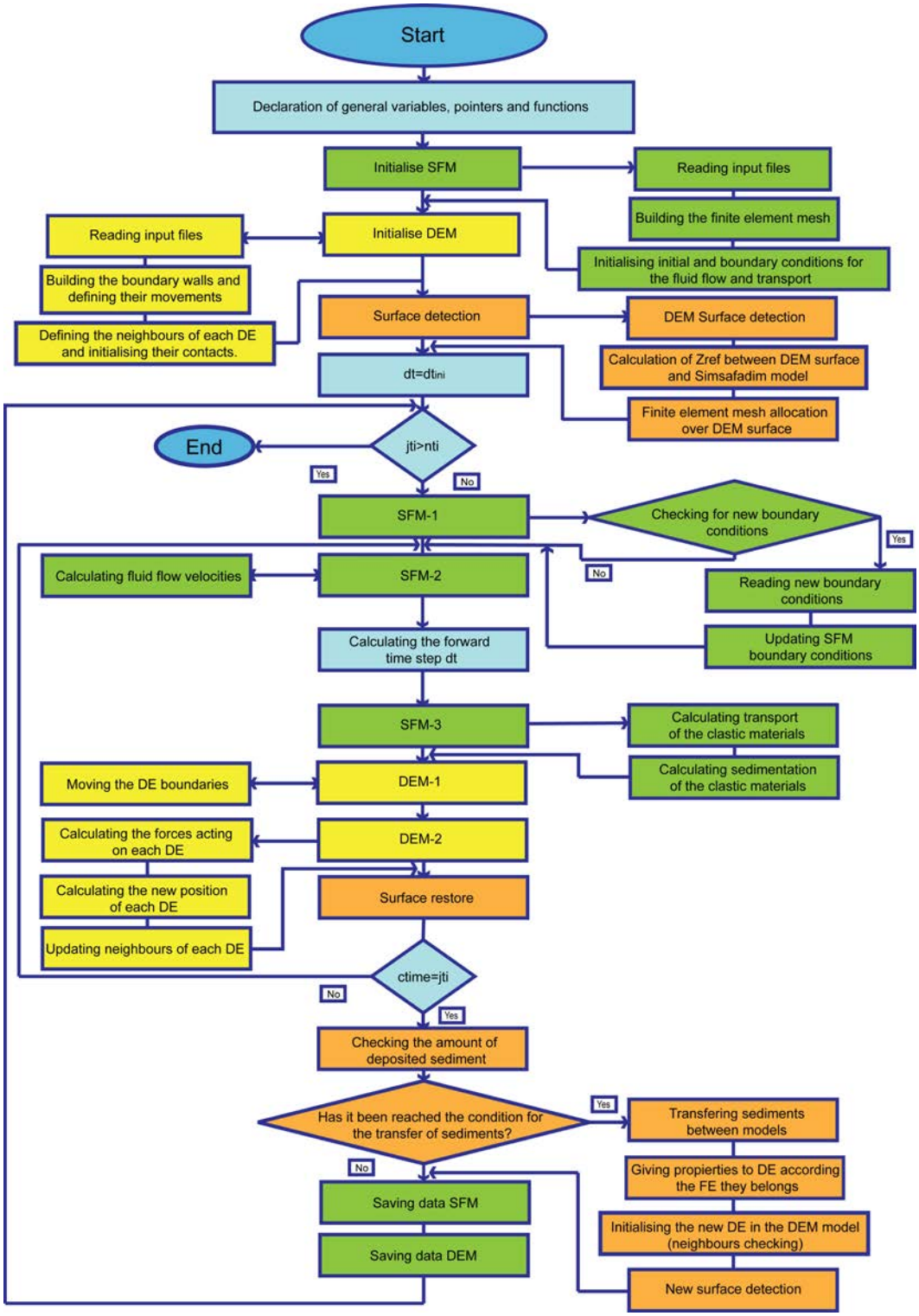

Figure 3.2.9. Flowchart showing the workflow of the merged code. Green coloured squares make reference to the parts of the code that includes the SFM model. The DEM part of the code is coloured in yellow. In orange are coloured the statements that make reference to the link between the two models: the finite element mesh allocation over the DE surface in order to shape the topography of the basin, and the sediment transfer between models. In light blue, the common parts of the code shared for both models are represented. These common parts mainly make reference to the general declaration of variables and functions and the advancing time step of the code.

3.2.5 Outputs and representation

Taking into account the methodology developed to model mechanical and sedimentary processes simultaneously, the experimental results can be represented using two different modes: through a DEM in which both pretectonic and syntectonic materials can be represented using DEs; or through the SFM, in which only the syntectonic unit can be represented using tetrahedral meshes.

The program saves information at pre-established time steps of the simulation time (*jti*). Considering the SFM visualization, a more detailed evolution of the syntectonic units can be represented as a function of the defined time steps *jti* (one stratigraphic unit in SFM corresponds to one time step). Considering DEM, the syntectonic materials visualization can also be done in each time step *jti*, but it is conditioned by the particle's diameter size (summarizing several time steps). Thus, new spheres can be visualized in DEM only at those time steps at which the transfer between SFM and DEM occurs. This lead to a lost of detail in the sedimentary model when it is represented through DEM (fig. 3.2.7). Obviously, if smaller spheres are defined, more detailed results can be presented, but longer run times are required. Hence, the use of both modes of visualization is recommended when this option is acceptable for SFM visualization type (see next section).

Using both programs, the following parameters can be represented in the FE mesh of the SFM or the DE of the DEM: the **sediment percentage** (defined by the amount of each clastic sediment type deposited in one time step in relation to the total sediment thickness deposited in the same time step, fig. 2.2.2 in chapter 2); or the **dominant sediment type**, where the FE or the DE is coloured in function of the most common sediment type per each time step. The total amount of deposited sediment in each time step, or specifically, the settled amount of each sediment type, can also be represented using the FE mesh.

As pointed out in chapter 2, the output files can be easily represented by (1) 'DataTank' (Visual Data Tools, Inc.), a tool to visualize numerical data, that here is used to show both the evolution of the DE model and the evolution of the sedimentation patterns of the different materials at each time step; and (2) 'ParaView', an open source visualization application, which allows a complete representation of the sedimentary model evolution.

3.2.6 Limitations of the new model

The methodology to combine both models involves some limitations, which must to be taken into an account when setting up a new experiment, or, specifically, when analysing and interpreting its results.

Some of these limitations are inherent to both models and the methodology used in their coupling. Nonetheless, most of these limitations could be easily improved; however these improvements are not included in the presented work. The main limitations are described below as well as some insights to improve them.

a) Size of the DEs: the 3D assemblages involve a large number of spheres, and depending on the model size, the diameters of the DEs have to be relatively large to avoid unmanageable DE assemblies, which too long computing time. Thus, the size of the DE is limiting the model in three different manners: (1) As it is mentioned in section 3.2.3.1, is conditioning when the sediment transfer can take place; (2) it is conditioning the resolution of the syntectonic sedimentary unit represented by the new DEs, since one DE may summarizes several times steps of the SFM model; and (3) it is also conditioning the resolution of the deformation model, since overly large spheres could influence the geometry of the final geological structure.

Clearly, smaller spheres would improve all limitations related to their size, but they also would increase the number of spheres in a model, therefore, would considerably increase the computing time. The user has to make a balance between the size of the model and its discretization (size of the DEs) and computing time, depending on the problem under consideration. Obviously more powerful computers will allow the assemblage to have a larger number of the DEs, with a smaller size, without to penalty of the computing time. But meanwhile the technology progresses, it is worth considering the parallelization of the code in MPI, which will allow us to run the simulation in a larger number of processors (see future task in chapter 6 for a further explanation).

b) FE mesh: Another limitation is related to the finite element mesh used by SFM, which has a fixed and static (in x, y direction) number of elements during the simulation. Those nodes of the FE mesh only accept vertical movements (in the *z* direction) in order to adapt to the DEM surface during deformation (fig. 3.3.10A). Nonetheless, the mesh can struggle to adopt the geometry of the DEM surface near the areas where surface is abrupt changing his slope attitude, e.g. at the bottom of steep slopes. Nonetheless, in these cases with high slopes, smaller elements of the FE mesh will minimize the error and the transition between near planar to almost vertical slopes, since will be more sensitive to

these abrupt topographic changes. This solution in the FE mesh will also provided a more accurate fluid flow velocities, since these are very sensitive to bathymetric changes, and therefore will also provide more accurate results for the concentration and sedimentation of the different materials. However, once again, a higher number of FEs will increase exponentially the computational time.

Considering this, one solution could be the introduction of an automatic adaptive mesh refinement. An adaptive mesh basically creates new elements in these areas with abrupt topographic changes, where a better discretization is needed (fig. 3.2.10 B). As such, the number of element of the mesh will only increase in those regions where a better discretization is necessary during the simulation time.

In the last time step of the figure 3.2.10A, it can be seen that the adaptation of the finite element mesh to the DEM surface, when there are high slopes in the topography, can lead to empty spaces and 'caves' between both surfaces. This difference between the two surfaces can be interpreted as deposited sediment when performing an update of sediment between SFM and DEM if this is not well defined (e.g. a solution could be not allow the deposition of an sphere in an element if the deposited sediment does not exceed a threshold limit). However, the correct and definitive solution lies in the introduction of an adaptive mesh refinement (fig. 3.2.10 B).

c) Syntectonic sedimentation in SFM between data transfer: Until the condition for the transfer of sediments between model is reached, the merged model is still calculating the sediment deposited in SFM at each time step. During these time steps, the deformation model keeps moving forward (deforming both pretectonic and previously transferred syntectonic sediments). Meanwhile the sediment deposited in SFM remains static in x,y position only recording deformation in vertical direction until the next transfer of sediments. This can lead to a difference between the final position the sediment have in DEM when the transfer is performed, and the real position that the sediment would had, if the transfer of sediment from SFM to DEM was instantaneously.

As pointed out in previous sections, smaller DE size would improve this limitation significantly, increasing the number of sediment transfer and thus, decreasing the difference in the sediment position. However, this solution has, again, the computer simulation time handicap, worsened by the fact that each sediment transfer requires also more computing time.

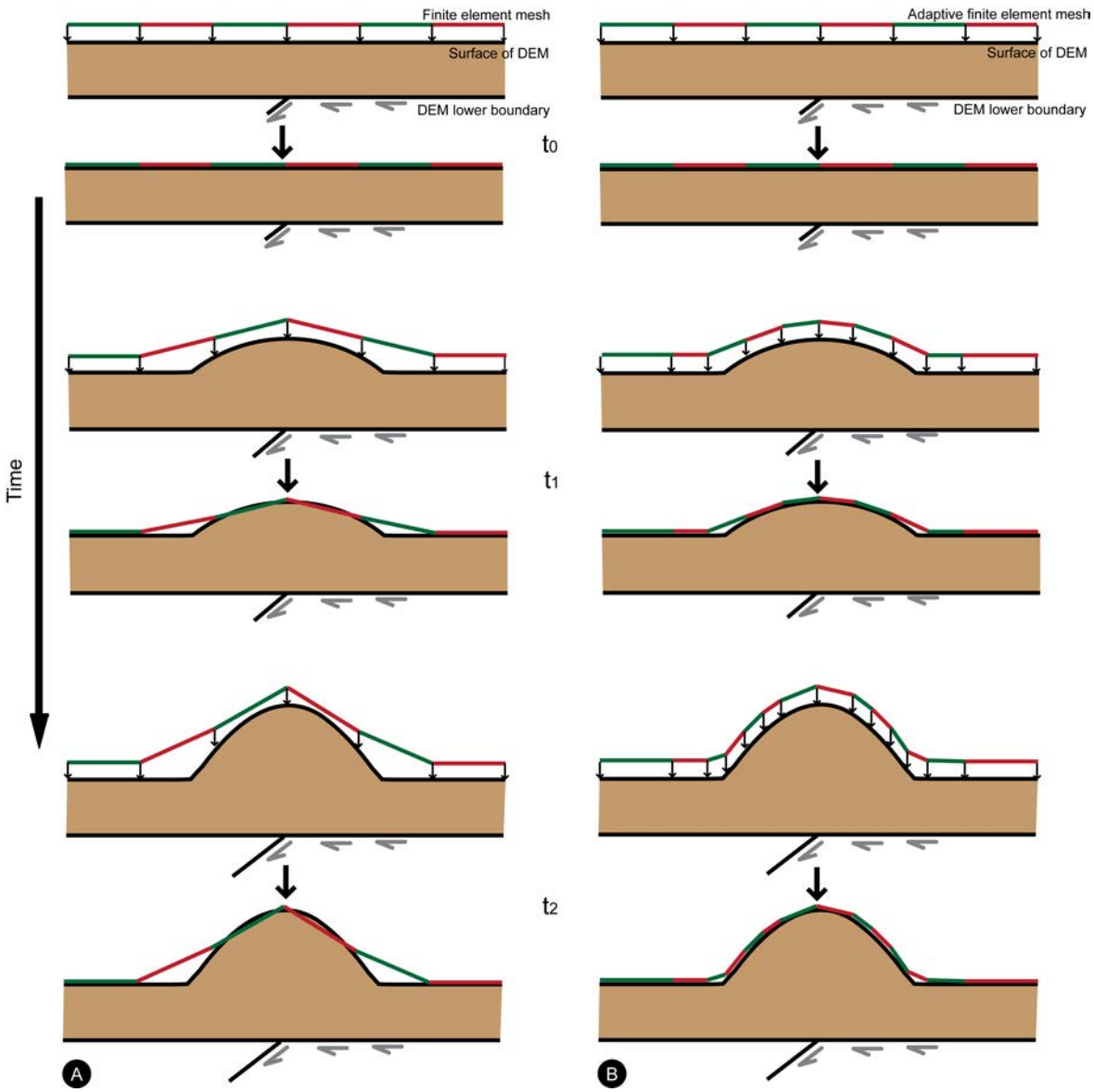

Figure 3.2.10. A- 2D simplified model that shows how the finite elements mesh adapts progressively to the changes of the topography as a consequence of a growing fold. It can be appreciated how topography and the surface defined by the FE mesh diverge as deformation progress and high topographic slopes are obtained. B- Same evolution of the topography, but considering an 'adaptive mesh', which creates new elements when abrupt slope changes are identified. Note that the example in this figure is just for an illustrative purpose.

Obviously, this difference is strongly conditioned by the experiment that the user is dealing with. For example, this difference is larger when DEM movements are mainly horizontal and/or close to the shortening boundary, and lesser when deformation movements are mainly vertical and/or far away from the deformation boundary The user has to determine when this difference between the final and the real position of the sediment is acceptable or not. As a simple rule, this difference can be considered acceptable when the relative movement of DEM in horizontal direction between two consecutive transfers is less than the distance between nodes in the FE mesh.

d) Data visualization using SFM: The representation of the syntectonic sediment through the tetrahedral meshes of SFM is possible because each node of the FE mesh will keep on saving its 'historical' sedimentary record for each time step. Nonetheless, due the deformation processes, it is possible, and more than probable, that the final position of this syntectonic sediment may vary between DEM and SFM. Therefore, the record of sediment in SFM just can be taken as a reference value, especially in the cases where the deformation rates are high in the horizontal direction. However, the position of this 'historical' record of the syntectonic sediment in SFM can be quite accurate with its final position when the deformation takes place mainly in the z direction, since the SFM stratigraphic surfaces are being adapted to this axis of deformation.

However, the limitations mentioned above are not an impediment in applying the model successfully to different case studies (see next section and chapter 6). Nonetheless it is worth to be aware of them, on the one hand, in order to look for solutions that could improve the model; on the other hand, for performing a better interpretation of the evolution of the models and their results.

3.3 THIRD PHASE - TEST EXPERIMENTS

In order to illustrate/check the potential of the new code, two simple examples are presented. The first one considers syntectonic sedimentation associated with an extensional fault, in order to analyse the evolution and distribution of sedimentation as a result of the tectonic movement, as well as the obtained syntectonic sedimentary architecture. The second example, considering syntectonic sedimentation in a thrust fault propagation environment, not only deals with the structure but also with deformation and the way in which the introduction of new sediments affect its evolution.

3.3.1 Initial configuration of the experiments

The two experiments use the same initial configuration. The DEM assemblage has a size of 250m×250m×2000m and consists of 8067 spheres of four different radii: 15, 13.75, 12.5 and 11.25 metres (fig. 3.3.1).

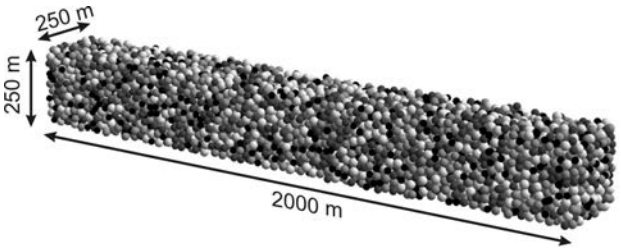

Figure 3.3.1. Initial discrete element (DE) assemblage used in the simulations

An initial finite element mesh of 180m×1800m size for the SFM is located above the assemblage surface. The mesh is divided into 32 columns and 4 rows, which results in 128 nodes or 186 triangular elements.

Sea-level is fixed at a height of 0 meters. Initial topography of the basin is −100 meters for all nodes, implying an initial bathymetry of 100 meters.

These examples save all information at each sixty years of simulation time. Both sample experiments are defined to be cohesionless. The coloured layers in the DEM are just used to better visualize deformation and addition of new sediments. Results are visualized using 'Datatank' program and deformation is calculated using the SSPX program (Cardozo and Allmendinger, 2009).

3.3.2 Example 1:Syntectonic sedimentation associated with an extensional fault.

3.3.2.1 Initial and boundary conditions

Using the common configuration described in Figure 3, for this extensional example an 80° dipping fault is defined in the bottom of the DE boundary (fig. 3.3.2). The rate of displacement along the fault plane, simulating extensional fault movement, is 0.06 $m.y^{-1}$ with a total displacement of 96 m in dip direction during the total simulated time (1440 y).

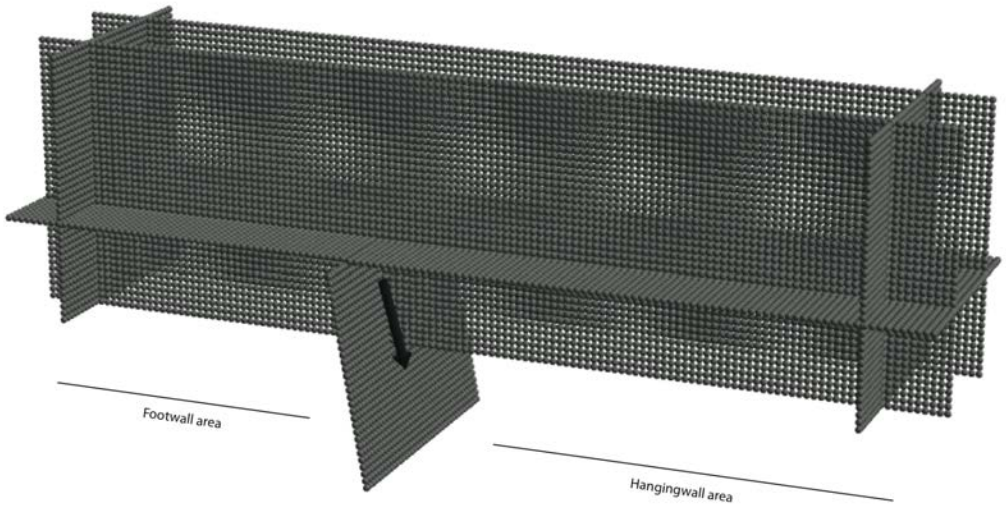

Figure 3.3.2. Bounding box of the DE assemblage with an 80 degrees dipping fault, used in the first example. The arrow shows the direction of relative movement of the hangingwall area (subsidence region) with respect to the footwall area.

Three different clastic sediment types are simulated in the model. They are characterized through their critical velocity for deposition and rate of settling as summarized in Table 3.3.1. These values are higher for coarse materials and lower for finer ones.

Table 3.3.1. Sedimentation parameters used for the first simulation considering an extensional fault.

Terrigenous sediment type	Settle Rate (m/d)	Critical Velocity (m/d)
Fine	0.003	2.5
Medium	0.004	4.0
Coarse	0.008	5.5

Inflow sediment rates are different for the different material types: they are smaller for coarser sediments than for finer ones. The inflow sediment nodes and rates are defined at a boundary node as can be observed in figure 3.3.3.

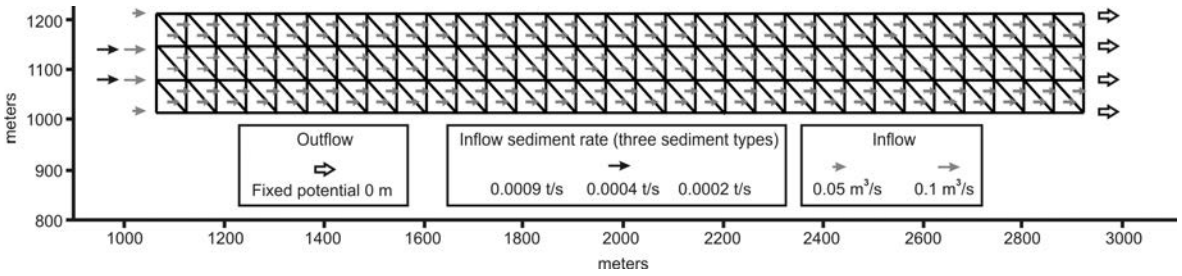

Figure 3.3.3. Finite element mesh used by SFM in the syntectonic sedimentation associated with an extensional fault example. The boundary conditions for the inflow of water and sediment, as well as the initial fluid flow velocity vectors are also represented.

The fluid flow boundary conditions for the finite element mesh reproduce uniform fluid movement from the left to the right with initial velocities that allow sedimentation of the three different sediment types from the start of the experiment.

3.3.2.2 Simulation results

Simulation results are summarized in figures 3.3.4, 3.3.5 and 3.3.6 where representative stages in the evolution of this example are shown. Each image in figure 6 shows the geometries of the DE model and the real topographic surface defined and used by the finite element mesh. Firstly we can see that four sediment transfers, from the SFM model to DEs, take place during the simulation (remember that transfer occurs as a function of the amount of sediment deposited and DE size). These new sediments are transformed into new layers of discrete elements that become an integral part of the DEM assemblage.

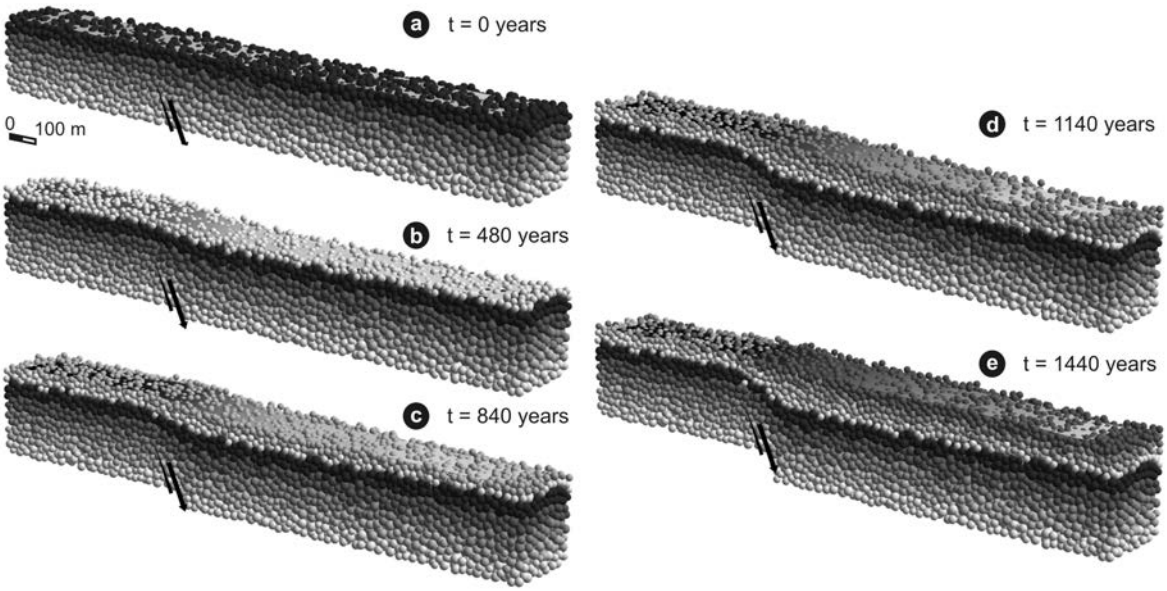

Figure 3.3.4. Simulation results showing the evolution of syntectonic sedimentation in an extensional fault. The different images are the model at the starting configuration and just after each sediment transfer between SFM and DEM. Four sediment transfers take place during the simulation, which are represented by the new whiter layers. Note how sedimentation takes place mainly in the footwall area where new accommodation place is created as consequence of the fault movement. The drawn surface is the real topography at each stage, which is result of tectonic movements plus sedimentation.

Focussing on the new layers (fig. 3.3.4 and 3.3.5), we can observe that in the earliest stage (480 y) sedimentation takes place along the entire model from the proximal area (located in the footwall) and decreases basinward due to sedimentation parameters and fluid flow conditions. Sedimentation in the footwall area drastically decreases during the next stage (840 y) and migrates basinward as a consequence of the water depth decrease and velocity increase due to sediment settling itself (fig. 3.3.5). In this time step (and the next ones), sedimentation becomes more prominent in the hangingwall area where new accommodation space is created due to the subsidence associated with the normal fault movement, and where fluid flow velocity decreases because of increasing water depth. As the simulation progresses (1140 and 1440 y), sedimentation is progressively restricted to the hangingwall area where accommodation space continues being created due to extensional fault movement.

In the hangingwall it is observed that, during the final part of the simulation, the model reaches an equilibrium phase between sedimentation and subsidence rates. As a result, the position of the topographic surface does not change considerably, and thus the fluid flow field does not change significantly.

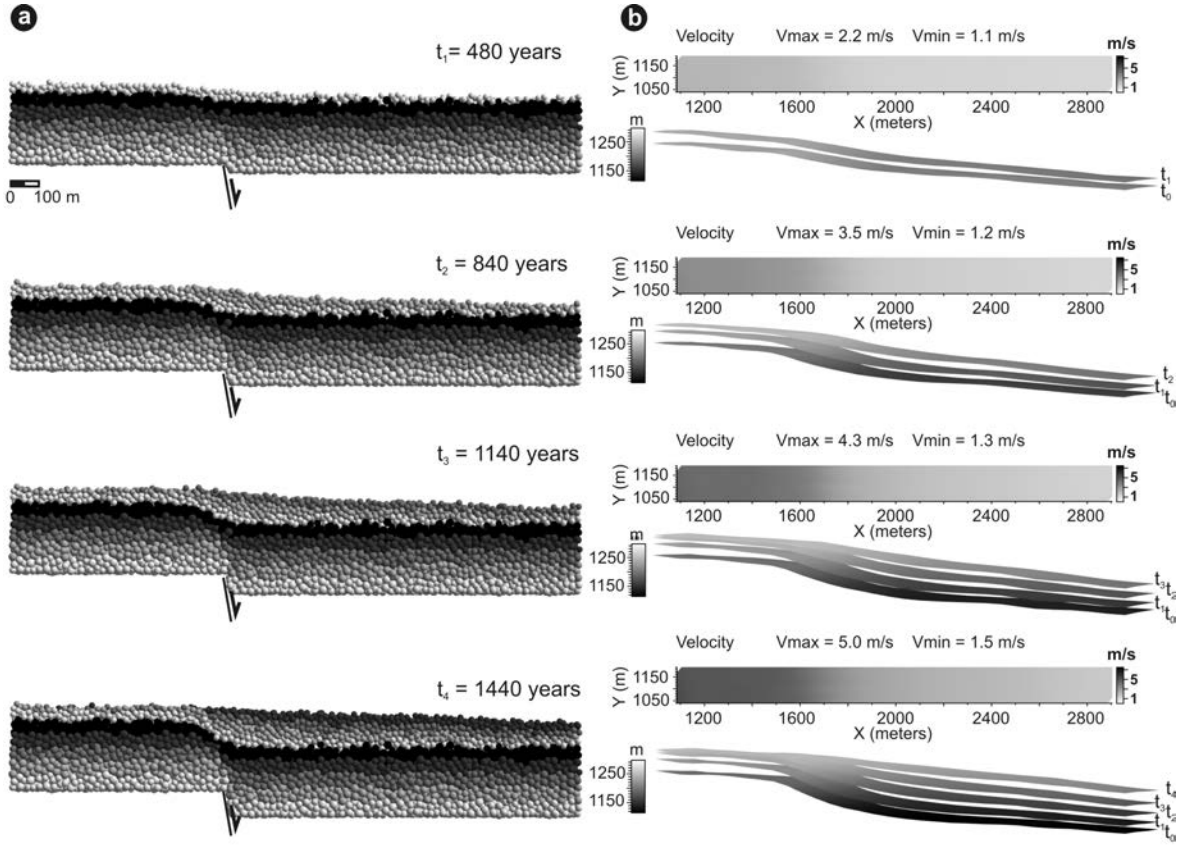

figure 3.3.5. Detailed representation of the evolution of the syntectonic sedimentation in an extensional fault in four different stages: a. Cross section showing the evolution of the DEM. b. Fluid flow map of the evolution of linear velocity at each stage. The evolution of the sedimentary geometries is represented through the current topographic surface and the current position of older surfaces. Maximum and minimum linear velocity is also indicated in each time step.

Different geometric architectures can be observed in pre and syn-extensional materials (fig. 3.3.4 and fig. 3.3.5). Pre-extensional materials shows a layer parallel pattern deformed near the fault area where a fault-propagation fold linked to an extensional fault system can be observed (cf. Jin and Groshong 2006). The fold is more evident in the later time steps. Looking at the syn-extensional sediments we can observe initial geometries resulting from the inflowing area, fluid flow system and accommodation space (as explained before). These initial geometries are deformed near the fault zone where the same fault propagation fold geometry can be observed. Bassal syn-tectonic layers are more deformed than the top one due to their existence during a longer time period. Deformation decreases upwards and away from the fault.

From the SFM model, each DE can store sedimentary properties such as percentage of each sediment type. Using these values, facies distribution can be obtained based on the most common sediment type at each DE (fig. 3.3.6). Only the coarsest and

the finest material are represented. This does not mean that the medium grain size material is not deposited; rather that this kind of sediment is not dominant at any location.

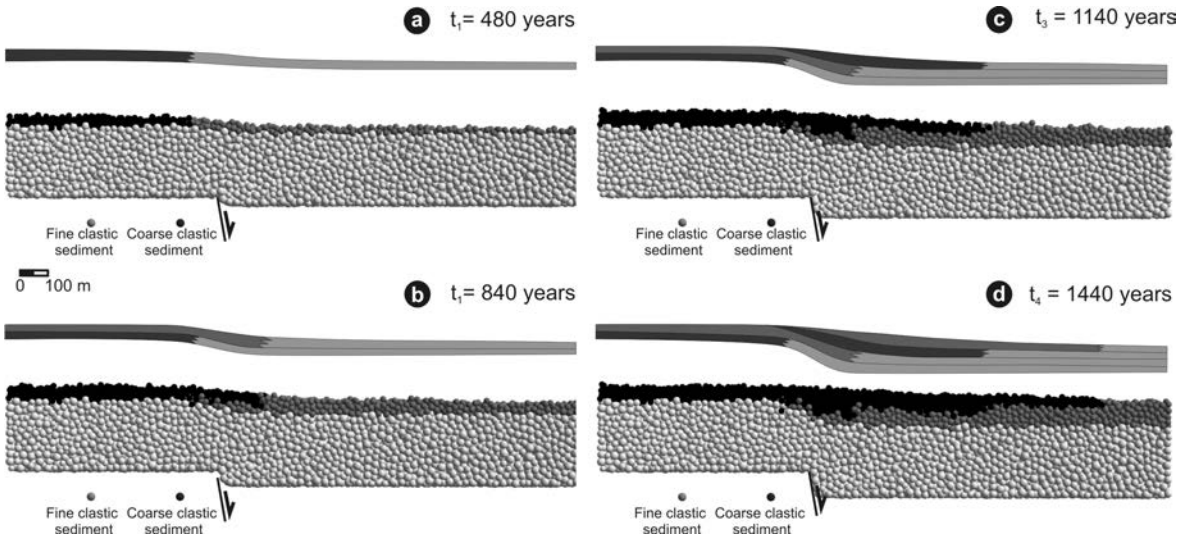

Figure 3.3.6. Representation of spatial distribution sediment at different stages during the evolution of the first simulation: (a) 480, (b) 840, (c)1140 and (d)1440 years. Different colours represent the material with a higher percentage in each discrete element: light grey for the finest material and deep grey for the coarsest one. A schematic facies distribution is also represented for each stage showing the sedimentary architecture propagation.

For the whole simulation, deposition of coarser material is concentrated in the more proximal area and passes laterally to the finer material basinward. Early stages show deposition of coarse sediments mainly in the footwall area. As a result fluid flow increases in the footwall region at subsequent time steps due a decrease in water depth. Deposition of both materials migrates to the hangingwall area where fluid flow has considerably decreased and more accommodation space is available due to the subsidence. As simulation time moves forward, coarse sediments overlap previously deposited finer sediments creating progradational geometries basinward.

3.3.3 Example 2: Syntectonic sedimentation and thrust fault propagation

3.3.3.1 Initial and boundary conditions

For the contractional sample experiment, a 45º dipping fault is defined in the bottom of the DE boundary box (fig. 3.3.7). The rate of displacement along the fault plane is defined as 0.03 $m.y^{-1}$ with a total displacement of 60 metres during the total simulation time (1800 y).

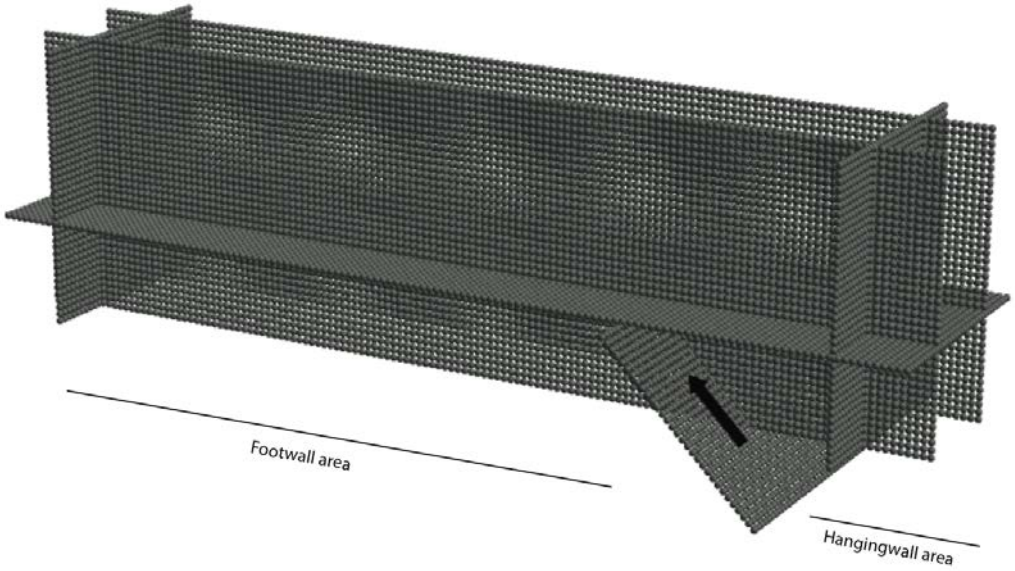

Figure 3.3.7. Bounding box of the DE assemblage with a 45º dipping fault, used in second example. The arrow shows the direction of the movement of the hangingwall area (uplifting region) with respect to the footwall area.

Three different clastic sediment types are also introduced in this example. Their critical velocity for deposition and their settling rates are summarized in Table 3.3.2. Figure 3.3.8 shows the boundary conditions for fluid flow. The inflowing boundary in this example has been defined on the right side of the model, reproducing a uniform flow from right to left with initial velocities that initially allow sedimentation of the three sediment types across the model.

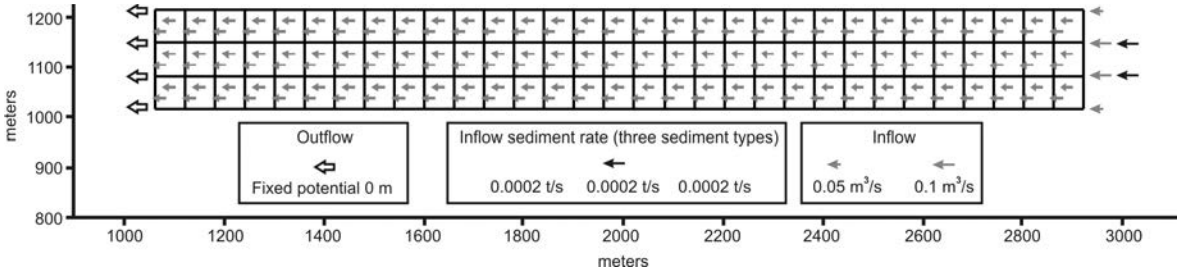

Figure 3.3.8. Initial mesh and boundary conditions for water and sediment inflow used by SFM in the second simulation. The initial fluid flow field is also represented.

Table 3.3.2. Sedimentation parameters used for the second experiment considering a thrust fault

Terrigenous sediment type	Settle Rate (m/d)	Critical Velocity (m/d)
Fine	0.004	3.5
Medium	0.006	4.5
Coarse	0.008	5.5

3.3.2.2 Simulation results

Representative simulation results are shown in figures 3.3.9 and 3.3.10 at four key stages (600, 1140, 1620 and 1800 y). In figure 3.3.9 the detailed evolution of the model is summarized using longitudinal slices of the DEM. In this example, three sediment transfers, from SFM to the DEM, take place during the evolution of the model. The four stages represented are immediately after these sediment transfers (three first stages) and the model at the final simulation time step (fig. 3.3.9).

The simulation results show how (as in the extensional example) sedimentation occurs during the first stage (600 y) in the inflowing region located on the hangingwall and how the thickness of this sedimentation decreases basinward. In the next time steps, sedimentation migrates into the basin because of the water depth decrease and fluid flow velocity increase due to sedimentation and the uplift of the hangingwall region. Consequently the locus of sedimentation is displaced to the footwall region where accommodation space is still available. This results in a progradation of sediments into the basin and a typical offlap geometry.

Using the methodology developed by Cardozo and Allmendinger (Cardozo and Allmendinger 2008) we can undertake a detailed analysis of the deformation in pre and syn-sedimentary materials (fig. 3.3.10). Maximum Shear Strain is calculated from the displacement of all DEs in the model. The shear strain is calculated between each stage.

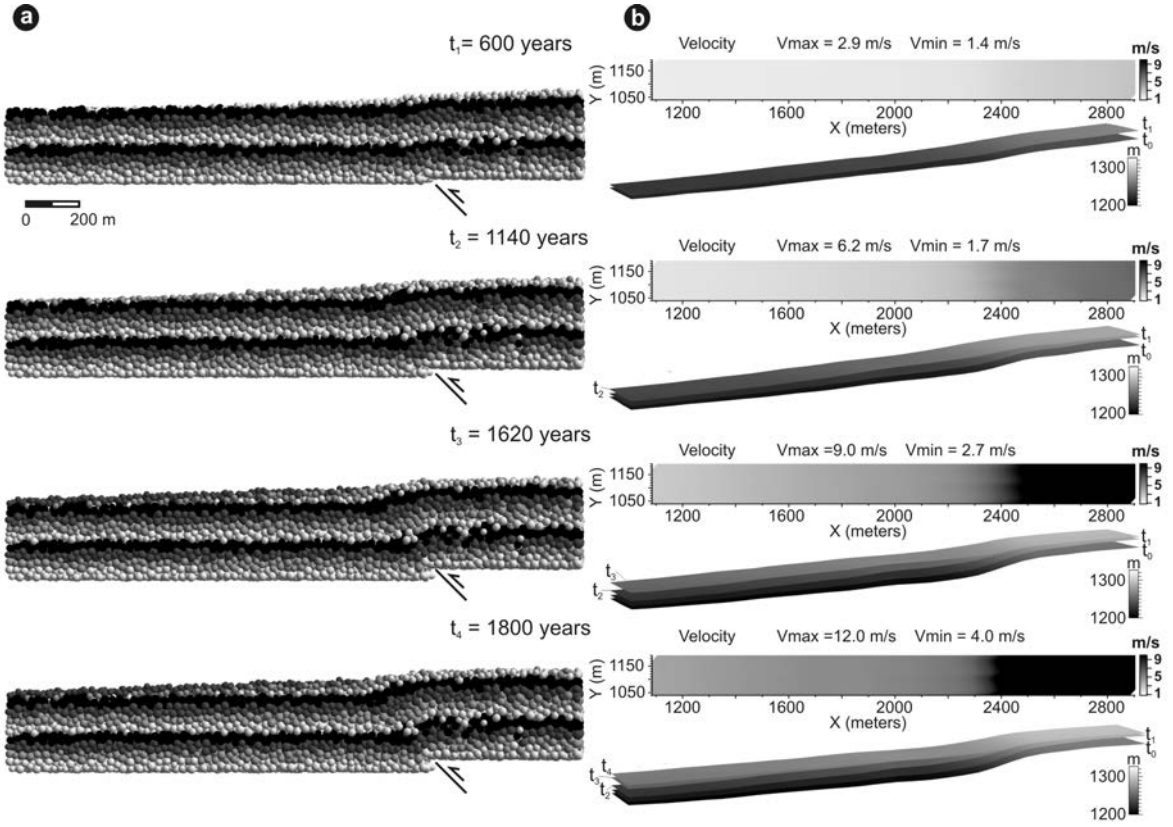

Figure 3.3.9. Simulation results for the second simulation: (a) longitudinal cross-section of DEM; (b) Syntectonic sedimentary geometries for four different stages. A fluid flow velocity map is also represented to facilitate the comprehension of the evolution of the sedimentation.

The represented time intervals in figure 3.3.10 have been chosen in order to show how the addition of the new sediments affects the evolution of the deformation in the model. Seven intervals have been selected: two for the time steps before the first transfer, two between each transfer and a last one after the last transfer.

The two first time intervals (up to 600 y) show how the propagation of deformation is concentrated above the fault zone where a fault-propagation fold linked to a contractive system has been developed. After the first sediment transfer from the SFM, we can see that the upward propagation of the deformation is firstly inhibited owing to the weight of the new material and it then is reactivated after a period of time. This effect occurs whenever new sediment is transferred and added, except during the seventh time interval when this effect is not so evident because new sediment is deposited farther away from the deforming region.

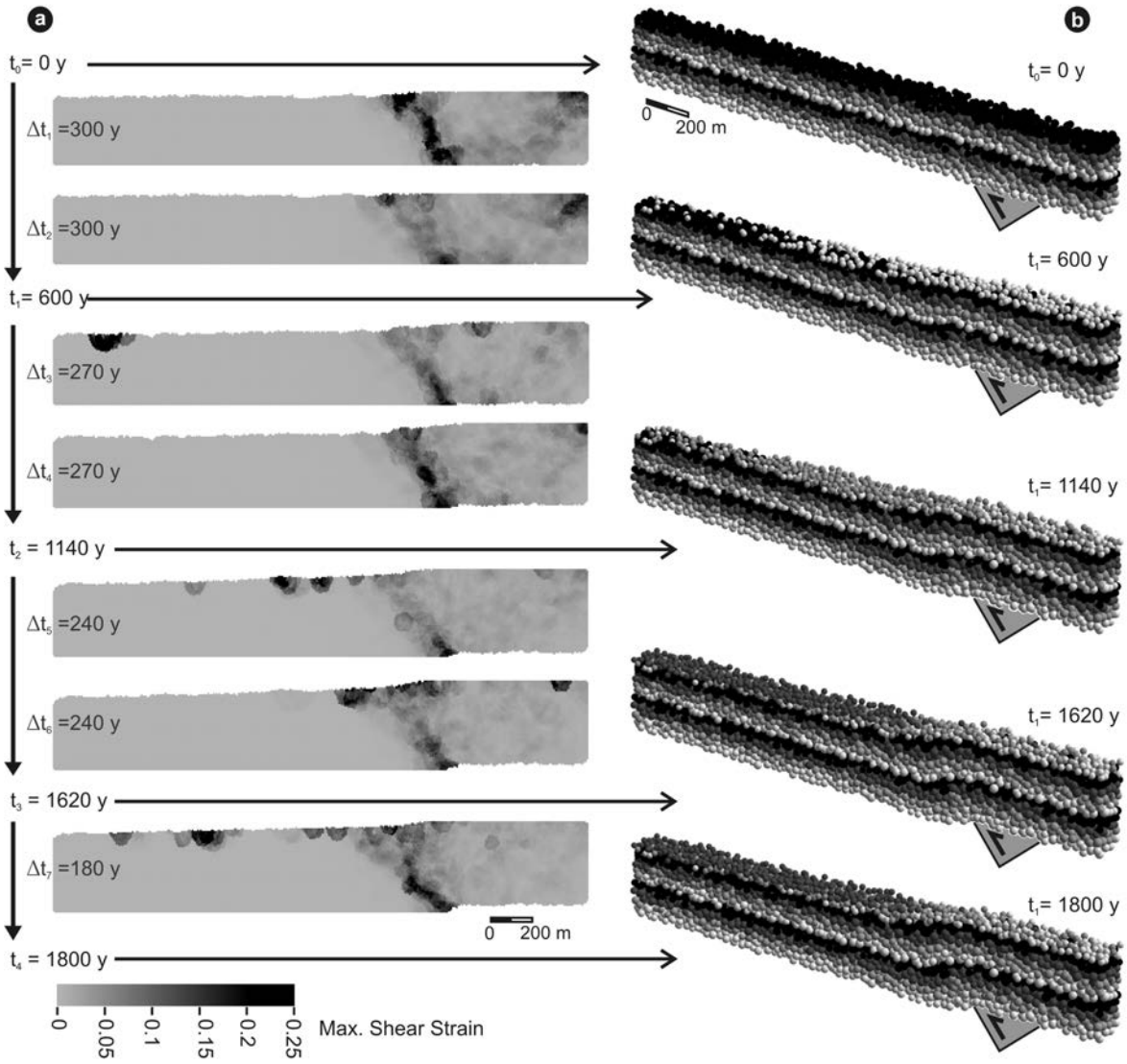

Figure 3.3.10. Evolution of deformation considering the syntectonic sedimentation in a thrust fault propagation example using SSPX program. Maximum Shear Strain is calculated from the displacement of all elements in the model. The shear strain is calculated between each stage. The analysis is divided en seven intervals (a). DEM images, sited on the left side of the figure (b), represent the stages among which the deformation study is performed.

CHAPTER 4

NEW FEATURES AND IMPROVEMENTS

4.1 NEW FEATURES IN SFM

A first merged version of SFM and DEM models was carried out using the previous version of SFM, called Simsafadim-Clastic and developed by Gratacós (2004).

While this coupling was being carried out, SFM was undergoing an important updating and upgrading (Clavera-Gispert et al. 2016, Clavera-Gispert 2016). The new improved version of SFM introduced new features such as (*i*) new sea-level changes curves; (*ii*) the possibility of the model to deal with subaerial nodes (and consider changing boundary conditions); and (*iii*) the possibility to treat a unlimited number of clastic sediments into the sedimentary system. Moreover, its code was upgraded to Fortran 90 and its algorithms were revised and restructured, which improved the computational efficiency of the code.

Since these new improvements and features would also be very advantageous in the merged SFM-DEM model, it was then considered to rebuild the merged model implementing the improved version of SFM.

Therefore, the process of translation of SFM into C language and the process of coupling the SFM and DEM code was redone. Despite the new features, however, the structure and workflow of the new SFM still allows applying the same previously described methodology to merge the models. In this sense, no new changes have been performed, apart from the introduction of the aforementioned new features of SFM.

The new version of SFM, translated from Fortran 90 to C language, does not imply any improvement in the model performance, since Fortran 90 have the same, or even more, of the advantages of C language, such as dynamic memory allocation or direct access of variables and vectors to the memory. Then, the SFM translation to C language only attends to reasons of practicality, since DEM and the auxiliary functions that interphase both codes were already programmed in C language.

Nonetheless, the process of rebuilding the new version of the code allowed a further revision of the code and auxiliary functions. The efficiency of some algorithms improved during this further revision.

The latest version of SFM also included an important update of the carbonate production and sedimentation model. However, carbonate sediment cannot be introduced yet as syntectonic sediments in the merged SFM-DEM model, since the new syntectonic DEs can be only considered cohesionless. Therefore the new carbonate production model is not introduced in this thesis but the reader is referred to the bibliography, already introduced in the chapter 2, for further information (Clavera-Gispert et al., 2012, Clavera-Gispert et al. 2016, Clavera- Gispert 2016). The reader is also referred to the cited works for a comprehensive description of the new features of the latest implementation of SFM model. Nonetheless, a brief description of these new features, which were introduced in the syntectonic sedimentary model, is provided below in order to better understand the capabilities of the new merged code.

4.1.1 Sea-level changes

The previous version of SFM only considers a static sea-level value or a linear trend defining a constant sea-level rise or fall. This can lead into limitations on the applicability of the code.

The upgraded SFM introduces a new feature that allows the model to introduce more complex sea-level variations. The sea-level changes are modelled through a function that combines five different trends: one linear and four sinusoidal. The pertinent definition of the different variables of this function allows activating any of these trends, or any combination of them (fig. 4.1.1). These trends can be modified at any time step.

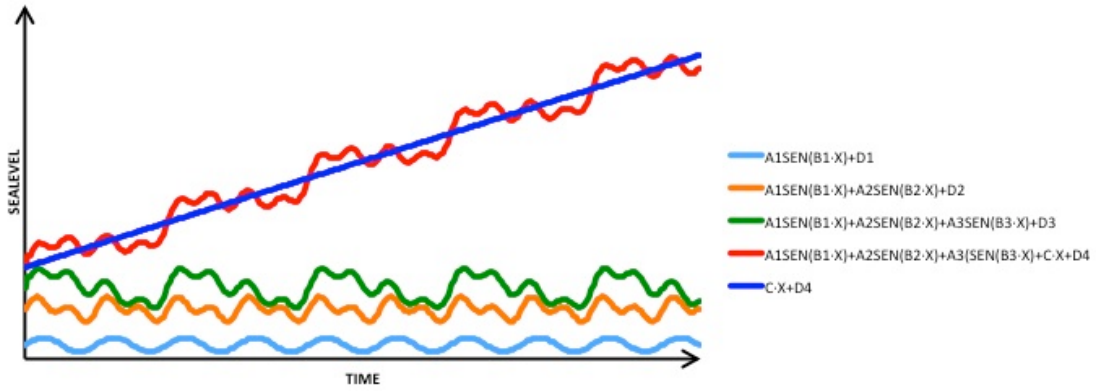

Figure 4.1.1 Plot showing five possible sea-level change functions that can be modelled by the new version of SFM: one linear trend function (dark blue line); a sinusoidal trend (light blue line); a function that combines two sinusoidal trends (orange line); another function combining three sinusoidal trends (green line); and a last one that combines three sinusoidal trends and a linear trend (red line).

The sea-level is calculated and applied at each time step. The sea-level variations modify the water depth on the entire basin, therefore sea-level changes affects directly the fluid flow velocities of the model and the sediment transport and deposition

4.1.2 Aerial nodes

In the previous version of SFM, the fluid flow and transport models cannot support aerial nodes because the equation solution systems have not been prepared to deal with them (i.e. numerical instability). Hence, the entire modelled basin must remain in subaquatic conditions during the simulation. This is a strong limitation because it is common that some parts of a basin emerge during its evolution due to sealevel changes or due tectonic movements. Hence, this was precisely one of the main improvements that had to be added in the new merged implementation of SFM-DEM code

The new version of SFM solves this limitation considering that when a node of the FE mesh changes from subaquatic to subaerial condition, the code considers that there is neither fluid flow nor transport processes nor sedimentary processes on it. If this node supports any defined initial or boundaries conditions, the nearest node with subaquatic settings assumes these conditions (fig. 4.1.2). If two or more nodes satisfy these conditions, the code randomly chooses one of them to transfer the initial and boundary conditions to this node.

4.1.3 Infinite number of clastic sediments

Finally, the improved version of SFM can introduce an unlimited number of clastic sediment types into the sedimentary system. The previous version of SFM only allowed the sedimentary system to deal with three different clastic sediment types. This limitation was mainly imposed by the architecture of the computing language used in that version, Fortran 77, which did not allow dynamic memory reservation, and the number of the clastic sediments had to be predefined in the code.

The syntectonic sedimentary model deals easily with this new feature. This updating will also be reflected in the new spheres added to the DEM model, which are representing the settled sediments by SFM. New syntectonic DEs now can represent any number of facies, as well as the properties of any number of clastic sediment type settled in the model.

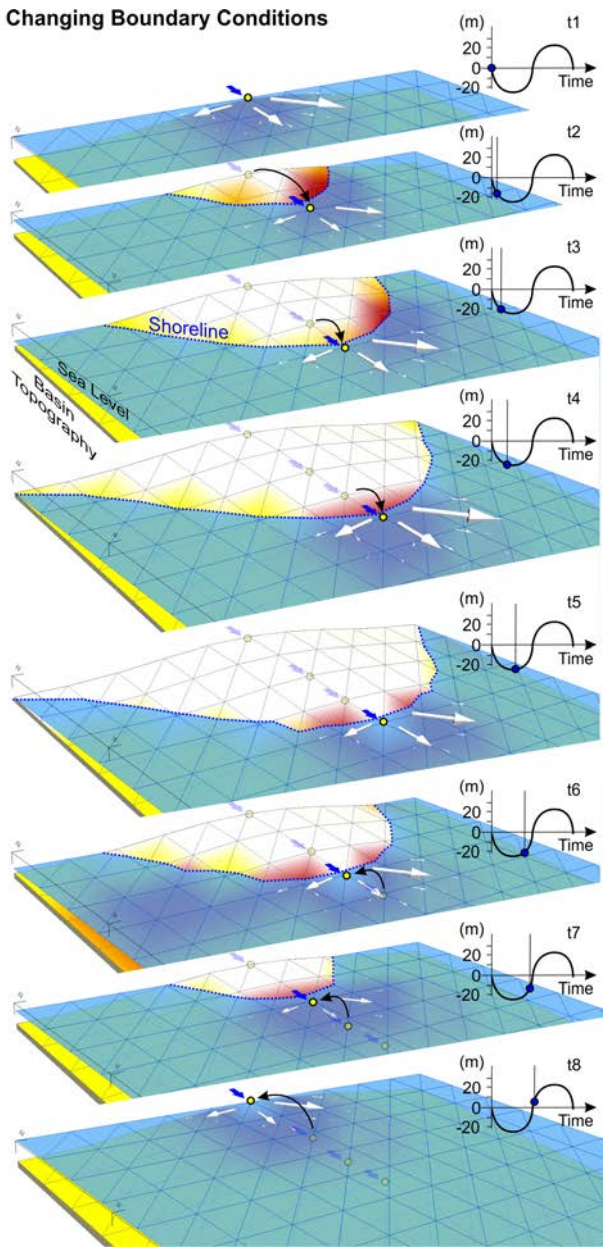

Figure 4.1.2. Evolution of a SFM example, which undergoes sea-level changes. The sea-level position follows a sinusoidal trend that causes regression/transgression episodes. During the regression periods, some nodes emerge, becoming subaerial nodes. The node supporting the boundary conditions changes accordingly the shoreline position, which migrates seaward. The new nodes supporting the boundaries conditions are always the closest to the original node but in subaquatic conditions. In the transgression periods when the sea-level rises again and the shoreline migrates inland, the boundaries condition returns to the shoreline nearest point.

4.2 PARALLELIZATION OF THE CODE IN OPENMP

As mentioned previously, one of the main problems of the new code is the long computational time required for some, most complete, simulations. The expensive consuming time in the new merged code is mainly due to DEM, as a result of that all the DEs of the assemblage has to interact among all of them to check potential neighbours and their interactions. One DE of the assemblage keeps its neighbours for a few time steps, but must to check them periodically to see if neighbours have changed. Therefore, the computing time almost increases exponentially with the number of spheres.

Despite the fact that the DEM is really time consuming due to the nature of their interaction, DEM is also the easiest code to parallelize. At one time step all the DEs of the

assemblage check their interaction forces with their neighbours and, consequently, they are moved to their new positions. At the next time step, this process is calculated again: the DEs reach their new positions according to the new interactions with the neighbouring spheres, which have, at the same time, modified their positions at the previous time step. This means that, at one time step, all the spheres are moved simultaneously to their new positions. And more important, the spheres only needs the information produced in the previous time step to reach their new positions at the current time step, so all previous information can be deleted. This last premise does not only make the parallelization easy, but also quite effective.

The parallelization of the code (only the part affecting to DEM) is performed in openMP (Open Multi-processing). OpenMP is a specification for a set of compiler directives, library, routines, and environment variables that supports multi-platform shared memory multiprocessing programming in Fortran and C/C++ programs. OpenMP can be used on most platforms, processor architectures and operating systems (e.g. Linux, OS X, and Windows).

The implementation of parallelization in OpenMP, together with the improvements and optimizations of the code, makes faster simulations in terms of computing time. To test the efficiency of the new parallelized code, a simple example is executed using a computer with 12 lines (i.e., twelve processors to share the tasks). The same example has been run with the old version without parallelization, also in the same computer, but just using one processor. The gain in terms of computing time is obvious: the example launched with the parallelized code took twelve hours to finish, while the example without parallelization spent seven days.

The improvements in computing time not only make more bearable to run an example, but it also open the doors to more complex and detailed new simulations. The case studies presented in the next chapter, would have been impossible to perform without the parallelization of the DEM code. With the implementation of the openMP parallelization, the limitations due to DEs size, introduced in the last chapter, are improved, but cannot be entirely eliminated and they still persist in real big models. Therefore it is worth to consider the implementation of other types of parallelization in the future (see section 'future tasks' in chapter 6).

4.3 A METHODOLOGY TO BUILD NEW DE ASSEMBLIES

In order to increase the geological scenarios where the new merged code will be applied, a methodology is developed to build any initial assemblage of DEs. This methodology allows building any assemblage of any size, and also choosing the radii and the number of different radii of the DEs.

To start to build a new assemblage of DEs, a simple code allocates randomly spheres of different radii into an initial box (fig. 4.3.1 A). Due to the initial assemblage of DEs will have high porosity values and needs to be compacted, it is important to define an initial box much bigger than the expected one. Once this initial assemblage of DEs is defined, the compaction process starts in 3D and its size is reduced considerably. As a general rule, it is recommended that this initial box will be, at least, three times higher and a quarter longer and wider than the desired final assemblage. This initial assemblage is the input for the DEM code. This code does not apply any boundary movements. Only the gravity is acting as an external force in order to reduce the porosity and increase the stability of the assemblage, until they reach an equilibrium situation (fig. 4.3.1A).

Once the compaction process is finished, some of the highest spheres of upper surface are removed in order to achieve the desired geometry or a regular surface, and also facilitate the next step. To achieve a properly compaction, the resulting assemblage is introduced again in a similar code changing the gravity direction to any other of the two space directions (x or y) (fig. 4.3.1 B). New wall boundaries are build accordingly the new gravity direction in order to prevent spheres falling off. The spheres are compacted again in the new gravity direction. The process of compaction is then repeated again for the third space direction (fig. 4.1.3 C). Finally, the assemblage of DEs is reduced to the desired size area and the compaction process is repeated once more time following the natural vertical gravity direction (z direction). After all, the DE assemblage can be modified to the desired height, if needed.

The possibility to work with different initial DEs assemblages also it had meant the adaptation of the DEM (and the syntectonic sedimentary code) to deal with any DE assemblage size. The new DEM code now is capable to read any initial DE box and to build their boundaries accordingly to the chosen initial movement conditions.

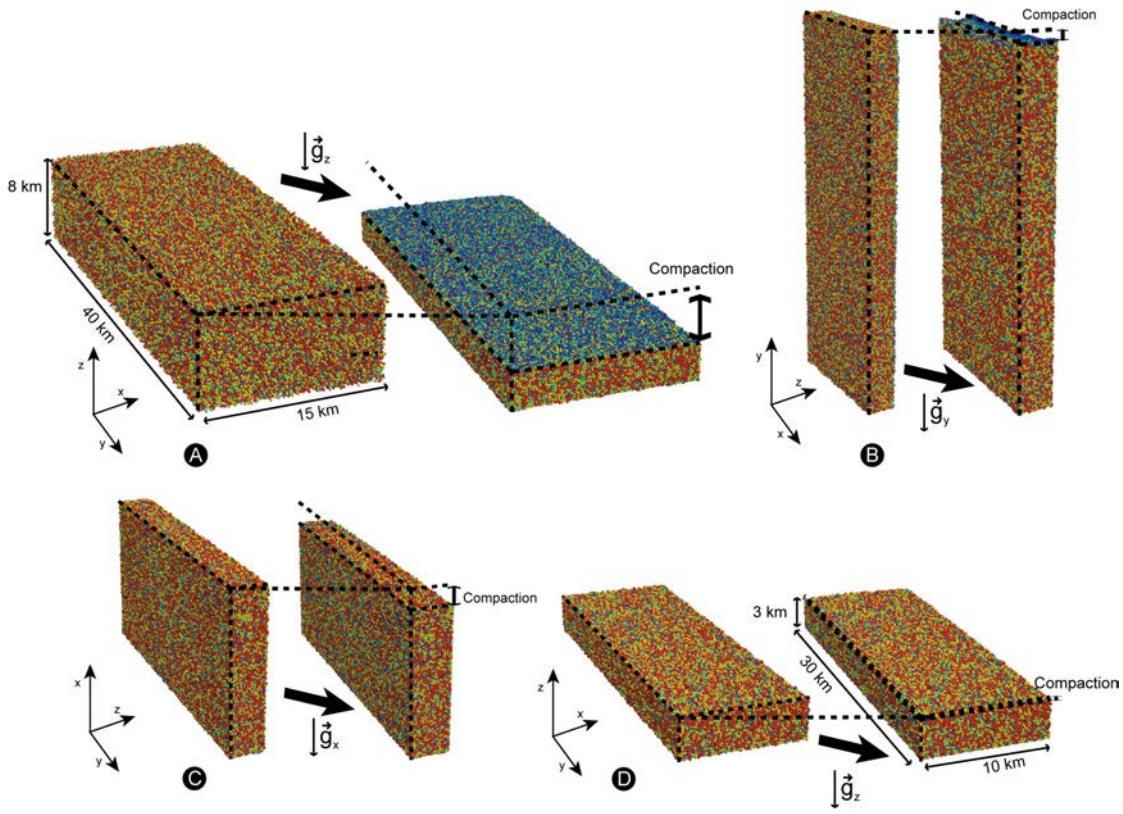

Figure 4.3.1. Four main steps to build a DEs assemblage: A- Initial DEs assemblage of 15x 40x 8 km, built with randomly allocated spheres of five different radii, 112m, 100m, 87,5m, 75m and 62,5m. Beside there is the same DEs assemblage after it has been compacted in the natural gravity direction (z axis direction). B- The same compacted DEs assemblage of the figure A where the direction coordinate system has been changed, in order to be compacted following the y axis direction. Beside there is the DEs assemblage after the compaction C- Same assemblage but now the compaction is defined along the x axis direction. D- Final DEs assemblage compacted, once more time, in the z axis direction. In this last compaction, the final area size of the DE assemblage is already defined, and only the height of the box is left to be determined after this last compaction.

CHAPTER 5

APPLICATION

5.1 NUMERICAL MODELLING OF SYNTECTONIC SUBAQUEOUS SEDIMENTATION: THE EFFECT OF NORMAL FAULTING AND A RELAY RAMP ON SEDIMENT DISPERSAL

5.1.1 Introduction

Transfer fault zones such as relay ramps are common in extensional systems and play a major role in the development of rift basins. The term relay ramp is normally used to describe the transfer zone between two overlapping synthetic extensional faults (Peacock 2002, Fossen and Rotevatn 2015) and can exhibit dimensions ranging up to tens of km. Relay ramps have been studied in many areas where they are well exposed, for example in the Canyonlands National Park in Utah (e.g., Trudgill and Cartwright 1994), the East African Rift (e.g., Morley et al. 1990), the rift in the Gulf of Corinth (e.g., Doutsos and Pipper 1990), and the Suez Rift in Egypt (e.g., Moustafa 2002).

The geometries of transfer zones, as well as their formation and evolution have been widely studied and analysed at all scales and involving different materials (Childs et al. 1995, Walsh et al. 1999, Nicol et al. 2002, Soliva and Benedicto 2004, Kristensen et al. 2008, Long and Imber 2011). Transfer zones and especially relay ramps play a significant role in sediment dispersal as they control the sedimentary pathways. It has been argued that in clastic systems, either terrestrial or submarine, relay ramps represent the fairways connecting adjacent extensional basins. As a consequence, they may control the location of sand and coarse-grained channel systems (Gawthorpe and Colella 1990, Gawthorpe and Hurts 1993). Normal fault growth, fault interaction and linkage processes drive the evolution of alluvial and fluvial drainage systems, river capture and channel incision, as well as the topography and accommodation created in the basin (Cowie et al. 2006). Therefore, together with other factors like sealevel variations and sediment supply, relay ramps are found to control the input of sediment into the basin, and the subsequent stratigraphy (Gawthorpe and Leeder 2000).

Different publications deal with the analysis and interpretation of case studies of syntectonic sedimentation in rift basins. These studies mainly focus on the understanding of the role of fault evolution on sediment dispersal and the synrift stratigraphic record. In

addition, these studies deal with fault growth and evolution patterns through studying these syntectonic sediments (Gupta et al. 1999, Dawers et al. 2000, Young et al. 2002, Rohais et al. 2007, Hemelsdaël and Ford 2014).

Numerical models have been proposed to understand and to study surface processes and deposition in extensional settings. They are able to reproduce sedimentation and deformation at the same time, treating their interaction in 2D and also 3D. These numerical approaches mainly deal with modelling of complex subaerial processes such as drainage network development and landscape evolution (Cowie et al. 2006), i.e. the evolution of the entry points and amount of sediment supply into the hangingwall basin and the consequent distribution of sediment. Moreover, some authors have also paid attention to coarse-grain delta formation and the evolution of stratal geometries under deformation (Hardy and Gawthorpe 2002, Gawthorpe et al. 2003).

The influence of relay ramps on sediment dispersal, both in subaerial and subaqueous settings, has been investigated in other studies. Athmer et al. (2010) presented a promising approach to study the impact of relay ramps on the pathways of turbidity currents by combining sandbox analogue modelling with numerical flow calculations. Other studies analysing the interplay between faulting and sedimentary infill at rifting margins were presented by Bruhn and Vagle (2005) and Athmer et al. (2011). A detailed review on the effect of relay ramps on sediment routes and deposition can be found in Athmer and Luthi (2011).

Nonetheless, the impact of subaqueous fault structures such as relay ramps on suspended sediment is less studied. However, these structures can also play a major role on the final deposition and grain distribution of suspended sediment dispersal into the basin. Bathymetric variations and changes of a rifting basin may significantly modify the velocity of the fluid flow of the subaquatic system, and therefore affect sediment dispersal.

In such subaqueous cases, numerical models could be a good approximation to analyse and to better understand syntectonic sedimentation. The main aim of this contribution is to give a qualitative insight on this topic by analysing the settling patterns of three different fine grain-size clastic sediments into the basin, related to the growth of two overlapping normal faults. In this study, a numerical program that combines realistic models of deformation and sedimentary processes in one single model is used (Carmona et al. 2010). This modeling approach allows performing a detailed study of the way sedimentation and tectonics interact in subaquatic systems. The model can reproduce not

only the evolution of the sedimentary bodies, but also the grain size distribution of these clastic sediments.

The variation of different parameters such as fault configuration, deformation rates, and discharge position of water and sediment into the basin will be treated in different examples in order to have a wider control on the impact of bathymetric changes on sediment dispersal.

Although the model does not yet consider isostatic subsidence or erosion, it is a promising tool to better understand suspended sediment dispersal and related facies distribution during the evolution of extensional basins. The program can include sealevel variations, but for this study the sea level has been considered constant during all simulations in order to focus on the influence of tectonic evolution on sedimentation patterns.

5.1.2- Experiment setup

5.1.2.1-Initial set-up, boundary conditions and experimental parameters

In order to study the effect of various fault configurations on syntectonic terrigenous transport and sedimentation in a subaqueous system, three main aspects are considered for the experiment set-up: **fault configuration**; **fault displacement rate**; and **source area**. Three different fault configurations are defined with three different fault displacement rates, resulting in 9 models. 4 different source area scenarios are added resulting in a total of 32 models. Focusing on the aim of this paper, only the most relevant experiments and results that provide key information are presented.

The initial experiment set-up defines both the DE box for deformation purposes of the pre-tectonic sediment (that will be used by the DEM program), and the FE mesh for the syn-kinematic terrigenous transport and sedimentation processes (used by SFM).

The pretectonic DE assemblage used in all experiments covers a volume of 7500 m x 5000 m x 1150 m and consists of 45,210 spheres of five different radii: 62.5 m, 56.25 m, 50.0 m, 43.75 m and 37.5 m (fig. 1A). These particles are assigned with cohesion, and with a breaking separation threshold of 0.001R, where R is the equilibrium separation between the particles. This breaking separation threshold is defining a weak sedimentary cover for the pretectonic material according to the results obtained by Finch et al. (2004). Coloured layers (fig. 1B) are used for better visualization purposes of the deformation; they do not show any mechanical property.

The related FE mesh for the sedimentary model is conditioned by the size of the DE, and it is discretized in 216 nodes (374 triangular elements). The FE mesh is located above the DE assemblage surface (fig. 1A). An initial regular bathymetry of 100 m is defined in the basin. Sea level is set constant during the evolution of the experiments; therefore, changes in bathymetry obey only to sedimentation and deformation processes.

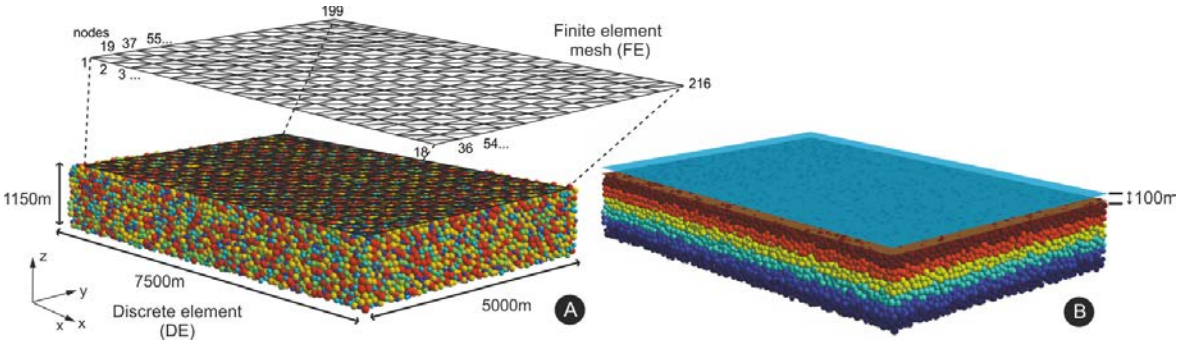

Figure 5.1.1. A- The discrete element (DE) assemblage coloured by size, and the related finite element (FE) mesh used in all experiments. B - DE assemblage, coloured by layers and an upper blue surface representing the sea level position related to the initial bathymetry.

5.1.2.2-Fault configuration and fault displacement rates

Bearing in mind the main objective of this paper, three different boundary conditions are imposed onto the initial DE assemblage in order to represent (1) one normal fault in two different basin locations (experiment 1 and 2; figs. 5.1.2 A and 5.1.2 B), and (2) two overlapping normal faults linked by a relay ramp (experiment 3, fig. 5.1.2 C). To compare the models, the position of the faults in experiment 3 coincide with each fault in experiments 1 and 2, i.e. at 2500 m and 4000 m, respectively (fig. 5.1.2). In all experiments, faults are dipping 80º towards the basin.

In order to understand the effect of the deformation velocity on sediment dispersal and sedimentation, three different dip-slip fault displacement rates, 2 cm/y, 5 cm/y and 10 cm/y, are applied to the different fault configurations. Spanning a total simulation time of 6000 years, split into 60 time steps -*jti*- of 100 years, these deformation rates produce a total displacement of 120 m, 300 m and 600 m, respectively, at the end of simulation (fig 5.1.2 D).

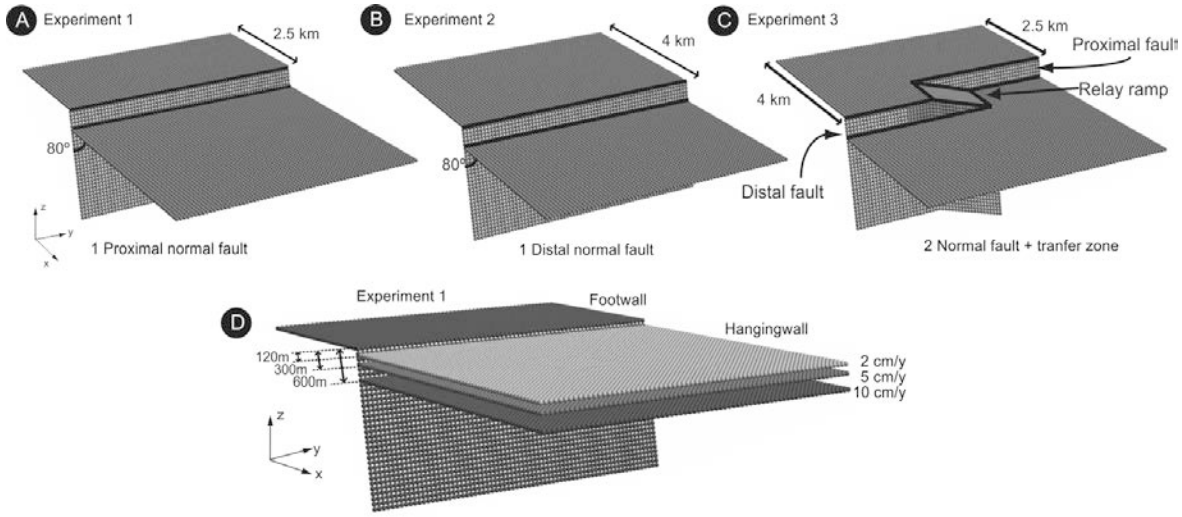

Figure 5.1.2. Fault configuration for the rigid basement of the defined DE boundaries for the experiment 1 with one proximal normal fault (A); experiment 2 with one distal normal fault (B); and two normal faults with a relay ramp (C). Final stages of the DE boundaries for the three different displacement velocities are also included, in this case for the first experiment (D).

5.1.2.3-Source area

Regarding the sedimentary model, two different boundary conditions are applied for the incoming water and sediment source area (fig. 5.1.3): a regional source boundary defined in all nodes of a FE mesh boundary sited in the footwall (fig. 5.1.3 A); and a punctual source, defined in two single boundary mesh nodes and located at three different basin positions (figs. 5.1.3 B, 5.1.3 C and 5.1.3 D). In the following, these two different boundary conditions will be referred in the text as RSBE (Regional Source Boundary Experiment) and PSE (Punctual Source Experiment). In both cases, the total amount of inflowing water and sediment remains constant. The inflowing water rate is chosen to be 12 m^3/s. The incoming sediment comprises three different terrigenous sediment types. Even though the different sediment types, all types are fine-grained sediments (those that can be transported by suspension such as sand, mud or silt). Nonetheless, they will be referred as coarse-, medium-, and fine-grained sediments in the text to distinguish among the three grains types of sediments. The three types of sediment are introduced simultaneously. The sediment types differ among each other from their critical velocity for sedimentation and their settling rate (Gratacós et al. 2009), i.e. the maximum velocity below which sediment can be deposited, and settles as a function of the theoretical settling velocity and the fluid flow velocity. The sediment supply rate for each sediment, as well as the different parameters that define each sediment type, are given in the table below (table 5.1.1). Under these initial conditions for the sedimentary model, together with the settling

properties defining each sediment type, an overfilled sedimentary system is obtained in all the simulations.

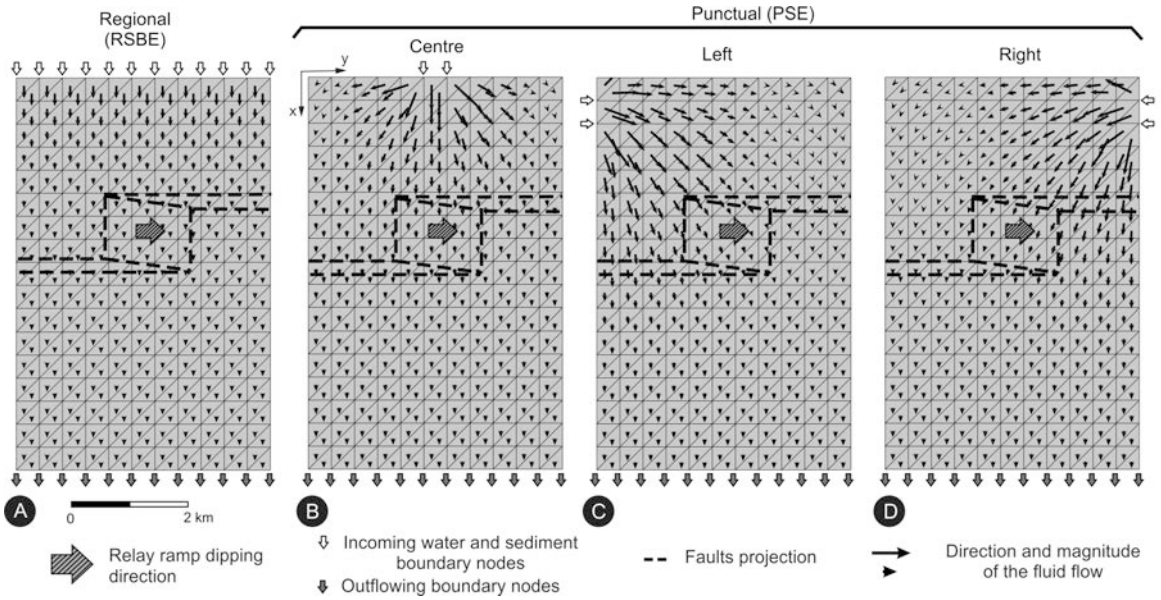

Figure 5.1.3. Boundary conditions for the sedimentary processes defined as: regional (RSBE) (A); or punctual (PSE) (B, C and D) thereby representing the third experiment with two overlapping normal faults linked by a relay ramp. The obtained fluid flow is also represented through black arrows. Note the greater velocities close to the inflowing nodes in PSEs than the RSBE experiment due to the same water discharge definition for all experiments.

Table 5.1.1. Parameters used to define the three terrigenous sediments in the experiments. Following Gratacós (2004), the critical velocity for deposition is a threshold value below which sediment can settle. Longitudinal and transversal dispersivity are defined as a function of the FE mesh discretization in order to avoid numerical errors solving the transport equation. In turn, the FE mesh is defined in function of the expected heterogeneity (Gratacós 2004).

Terrigenous sediment type	Sediment supply: Fixed Rate (T/s)	Settle Rate (m/d)	Critical Velocity (m/d)	Longitudinal dispersivity (m)	Transversal dispersivity (m)
Fine	0.16	0.1	4.0	400	400
Medium	0.08	0.5	4.5	400	400
Coarse	0.04	2.0	5.0	400	400

5.1.3- Experiment Results

5.1.3.1-Experiment 1: one proximal normal fault

The simplest structural configuration (one normal fault in its more proximal position, fig. 5.1.2 A) is used to analyse the effect of fault displacement rate on sediment distribution. In this case, the incoming water and sediment boundary conditions are defined as regional through all the nodes of the upper boundary of the FE mesh (RSBE, fig. 5.1.3 A). The fault is located 2500 m from the source area, and the three fault displacement rates 2, 5 and 10 cm/y are used (figs. 5.1.2 A and 5.1.2 D).

Under these conditions, and focused on the deformation obtained in the pretectonic sediments (fig. 5.1.4), the model results at the end of the simulation time are in agreement with the predictions of the trishear kinematic model related to a fault propagation fold (Erslev 1991, Hardy and Ford 1997, Allmendinger 1998, Finch et al. 2004). In such model a triangle deformation zone with a significant layer thinning and thickening can be observed. Maximum shear strain is calculated using the SSPX program (Cardozo and Allmendinger 2009), which is an application to compute strain from displacement/velocity data in two and three dimensions. Here, maximum shear strain is calculated from the displacement between the particles from time step 1 to time step 60. Maximum deformation rate is located in the trishear zone linked to the normal fault, and also in the hangingwall. Deformation in the hangingwall area is interpreted as a result of two factors: due to the tectonic extension, which can produce a relocation-accommodation of the pretectonic material in this area; and due to the weight of the new deposited sediments. This kinematic deformation model results in a monoclinal fold in the pre-tectonic sediments and a smooth topographic profile from the footwall to the hangingwall, conditioning the geometry and the evolution of the syntectonic sedimentation. Considering the different displacement rates, the fold is more or less developed.

When investigating the sediment distribution, two main deposition areas can be observed (fig. 5.1.5). The first one is located on the footwall close to the inflowing water and sediment boundary where no subsidence occurs. Deposition in this area takes place during the first time steps (from time step 1 to 4), infilling the available accommodation space and showing clearly progradational geometries with coarse deposits passing rapidly into medium and fine sediments (fig. 5.1.5 C). Due to the sediment input definition (table 1) the finest-grained sediment is the most common sediment type settling during the first time steps. Coarse and medium-grained sediment are also present but mainly close to the inflowing boundary (fig. 5.1.5 C). Evidently, due to the fact that deformation is not creating

accommodation space in the footwall area, this sediment distribution pattern is the same in the three models (considering 2, 5 and 10 cm/y).

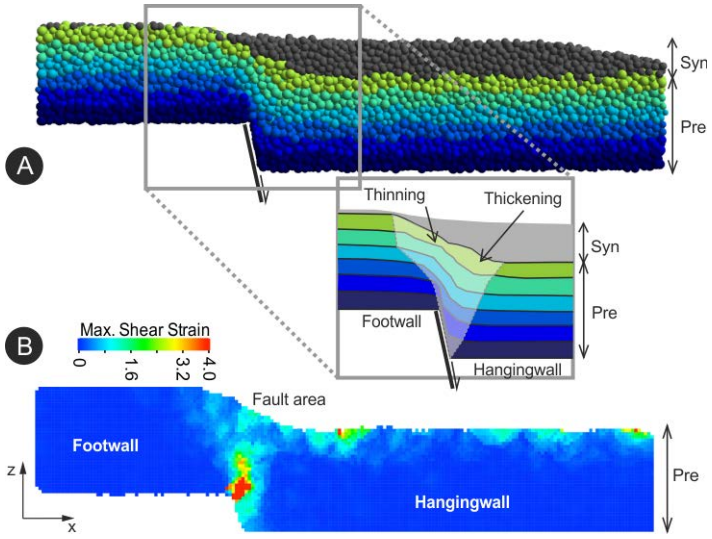

Figure 5.1.4. Deformation in the pretectonic sediments obtained at the end of the simulation time considering one normal fault: A. Final stage and the interpreted fault area for the first sample experiment with a 10 cm/y deformation velocity. The pretectonic discrete elements are coloured by layers only for visualization purposes. B. Maximum Shear Strain in the pretectonic sediments between jti 1 and 60 using the SSPX program for the same sample experiment. The "trishear" fault propagation fold, and the deformation in the hangingwall can be observed in both representations.

The second deposition area is located basinward and is related to the hangingwall subsidence. While in the footwall areas sedimentation does not show clear differences among all models, in the hangingwall area some variations can be highlighted mainly controlled by the different displacement rates (figs. 5.1.5 A, 5.1.5 B and 5.1.5 C). In general, differences in the dominant sediment type distribution can be observed. The distribution trends are wider due to less accommodation space with lower displacement rates, which causes higher fluid flow velocities in the hangingwall area (fig. 5.1.6) and far transport distances of the different clastic sediment types (figs. 5.1.5 B, 5.1.5 C and 5.1.5 E). Analysing the different fault displacement rate results separately (fig. 5.1.5 C), a general progradational trend can be observed that evolves into aggradational and even retrogradational. The lowermost part of the infill shows a highly basinward progradational trend with a minor aggradational component (time step 1 to 6) while the initial accommodation space is filled. When the accommodation space decreases and becomes dominated by tectonic subsidence, this trend evolves into a more aggradational pattern (from time step 7 to 30). Afterwards, the trend is mostly aggradational with a slight retrogradational component in the uppermost levels.

Comparing the dominant sediment type distributions in the different deformation velocities models, some differences can be observed (fig. 5.1.5C): for the 2 cm/y velocity model, coarse-grained sediment is the most representative, and the finest one (and part of the medium) is mostly outflowing the model; for the 5 cm/y a basinward transition from coarse- to medium-grained deposits is observed; while for the 10 cm/y the gradation includes also the finest sediment in the distal parts, and foresets are recorded.

Considering the most detailed example (10 cm/y, fig. 5.1.5C), a detailed study is done for some characteristic nodes in the basin (fig. 5.1.5D): on the footwall (node 92) ; in the fault zone (node 96); and in the hangingwall (in a proximal (node 99) and distal (node 106) position). Comparing the evolution of subsidence (defined by the distance between the top of the pretectonic sediments and the sea level position) and water depth (defined by the distance between the basin floor and the sea level position), an initial similar behaviour between subsidence and water depth can only be observed near the fault and hangingwall area (nodes 96, 99 and 106). During this initial period, bottomset beds are recorded in each node, except in the footwall area (node 92) due to time step discretization and a rapid progradation. When water depth decreases as a result of clastic sedimentation and basinward progradation (see the water depth line chart decrease in fig. 5.1.5D), foreset beds are recorded in the stratigraphic logs. When the water depth remains constant, due to the equilibrium between subsidence and sedimentation, also topset beds are observed. Considering this, the lower part of the succession (see the stratigraphic log for the node 99 as an example in fig. 5.1.5E) records clinoforms with a more sigmoidal geometry and with higher delta front slopes infilling the initial accommodation space. Due to less accommodation space, mainly controlled by the subsidence rate (sediment supply is defined as constant), fluid flow velocities are higher and the fluid flow profile, from proximal to distal parts, is smoother. Therefore, sedimentary bodies on the upper successions are more tabular, and lower delta front slopes develop (fig. 5.1.5E). Mainly for this upper part succession, the distribution of the dominant sediment type in the hangingwall area shows some slightly retrogradational and progradational trends. These trends are related to small vertical tectonic spheres movements, which are a consequence of two factors: the extensional deformation also affecting hangingwall pretectonic materials; and the new sediment load and their post-deposition accommodation (see white arrows indicating variations in subsidence and water depth in fig. 5.1.5D, and the deformation that can be observed in the hangingwall in fig. 5.1.4B).

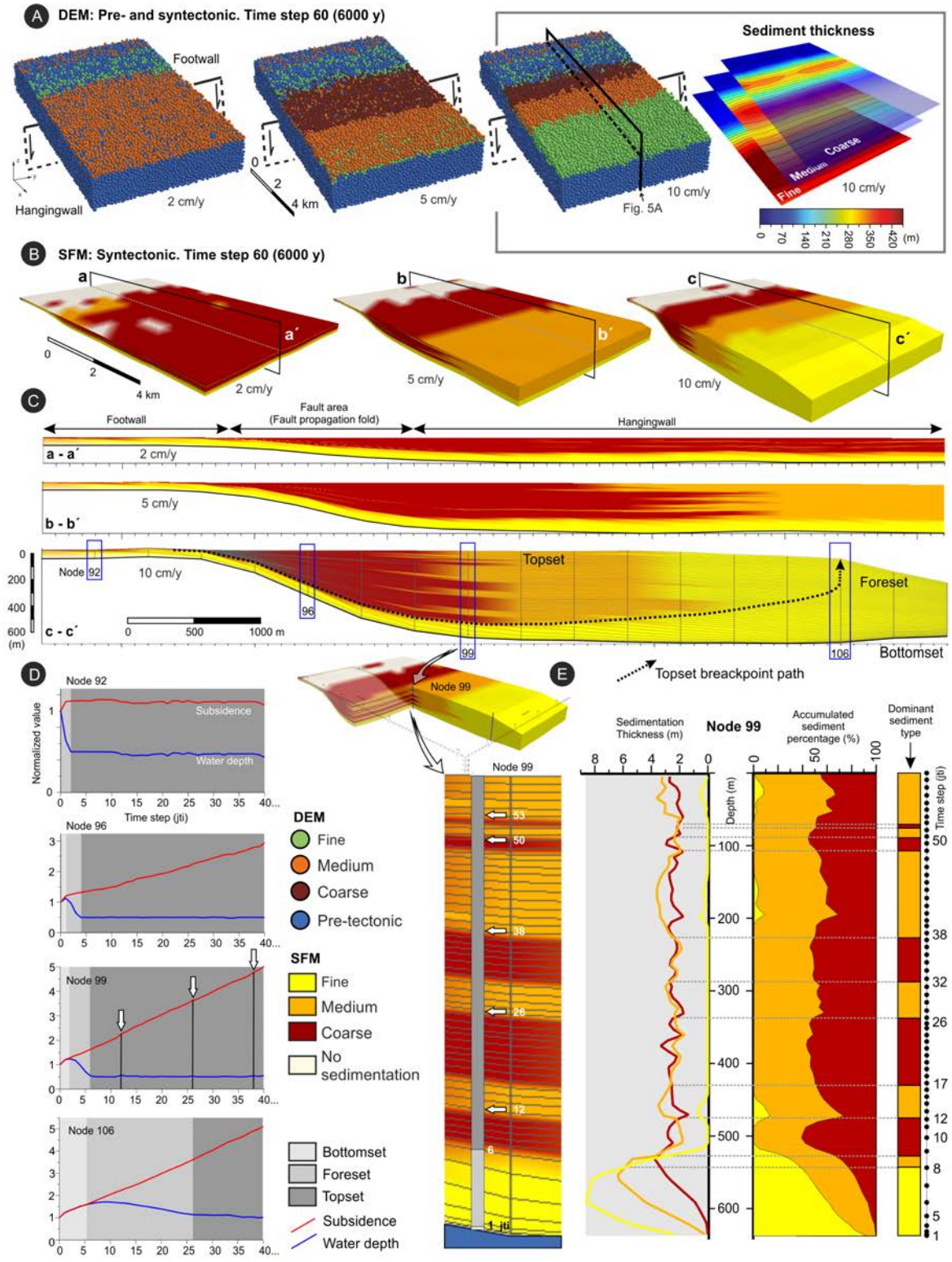
A DEM: Pre- and syntectonic. Time step 60 (6000 y)
Footwall
Hangingwall
2 cm/y
5 cm/y
10 cm/y
4 km
Fig. 5A
Sediment thickness
Fine
Medium
Coarse
(m)
B SFM: Syntectonic. Time step 60 (6000 y)
C
Footwall
Fault area
(Fault propagation fold)
Hangingwall
a - a´
b - b´
c - c´
Node 92
Node 96
Node 99
Node 106
Topset
Foreset
Bottomset
D
Normalized value
Subsidence
Water depth
Time step (jti)
DEM
Fine
Medium
Coarse
Pre-tectonic
SFM
Fine
Medium
Coarse
No sedimentation
Bottomset
Foreset
Topset
Subsidence
Water depth
E
Topset breackpoint path
Sedimentation Thickness (m)
Depth (m)
Accumulated sediment percentage (%)
Dominant sediment type
Time step (jti)

Figure 5.1.5. (Figure in the left page.) Experiment results for the first example with one proximal normal fault and a RSBE. A. DE model showing the pretectonic and syntectonic materials coloured by the dominant sediment type obtained for the three different fault displacements: 2, 5 and 10 cm/y. B. 3D oblique view for the syntectonic package considering the three displacement rates represented using de SFM numerical results and coloured according to the dominant sediment type. C. Cross-sections from the same models. Grey lines in the c-c' cross-section are represented to show the sedimentary architecture for each time step (jti). D. Line charts with the evolution of the subsidence (defined by the distance between the top of the pretectonic sediments and the sea level position) and water depth in different points of the basin (see location in the previous cross-sections). Note the normalized value for the Y coordinate and the different scales per node. Time steps from 40 to 60 are not represented due to a constant behaviour. E. Stratigraphic log and the related sediment thickness deposited in the node 99 located in the hangingwall, near the fault. Accumulated sediment percentage, and the most common sediment deposited are also represented (facies). Arrows indicate time steps with an anomaly increment in water depth and subsidence (due to punctual vertical tectonic movements) causing a retrogradation.

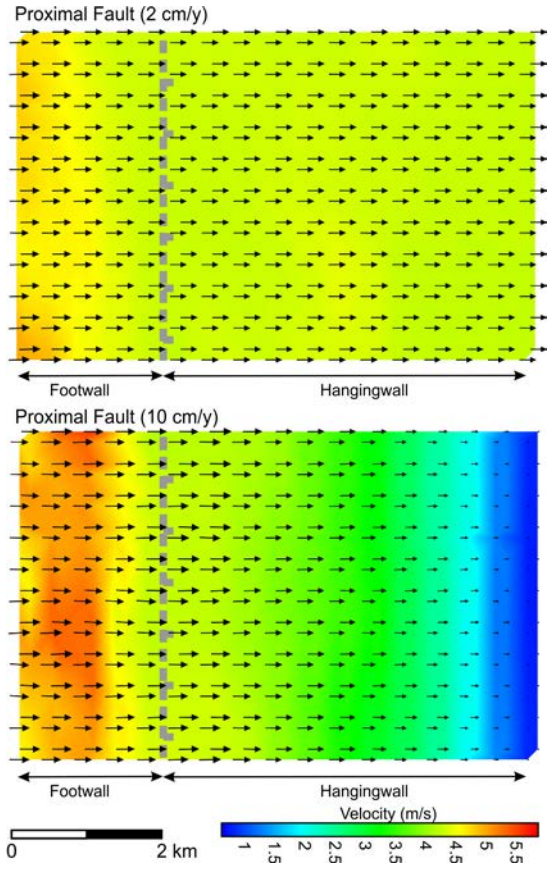

Figure 5.1.6. Fluid flow velocity maps at the end of the simulation time for the first example with one proximal normal fault and a RSBE considering two deformation rates (2mm/y and 10mm/y). Note the higher fluid flow velocities in the hangingwall area for the lower deformation rate due to less accommodation space. The example with lower deformation rates shows also a more constant basinward velocity, while for higher deformation rates, the velocity decreases basinward due to the increase of accommodation space. These differences in the velocity in the hangingwall area between both examples result in noticeable differences in their sedimentary patterns (see figure 5A and 5B).

Four representative time steps for the 10cm/y model are represented in figure 5.1.7 (*jti* 11, 25, 36 and 53 corresponding with 1100, 2500, 3600 and 5300 years respectively). These time steps represent the moments when new spheres are added to the DEM in response to the syntectonic sedimentation obtained by the SFM, in order to introduce the

new sediments into the mechanical model. These new elements (fig. 5.1.7A) are coloured in function of the dominant sediment type and are a mixture of the sediment settled in the corresponding time steps. More detailed results can be represented trough SFM results (figs. 5.1.7B and 5.1.7C). As noticed before, the same stratigraphic trend can be observed, with a basal, dominantly fine-grained stratigraphic unit (jti 11, fig. 5.1.6B, and the fine-grained sediment percentage in fig. 5.1.7C) characterized by the sedimentation of sigmoidal, mainly progradational, sedimentary bodies. At subsequent time steps, more aggradational and tabular sedimentary bodies are obtained, showing a basinward transition from coarse- to fine-grained sediment type (figs. 5.1.7B and 5.1.7C).

new sediments into the mechanical model. These new elements (fig. 5.1.7A) are coloured in function of the dominant sediment type and are a mixture of the sediment settled in the corresponding time steps. More detailed results can be represented trough SFM results (figs. 5.1.7B and 5.1.7C). As noticed before, the same stratigraphic trend can be observed, with a basal, dominantly fine-grained stratigraphic unit (jti 11, fig. 5.1.7B, and the fine-grained sediment percentage in fig. 5.1.7C) characterized by the sedimentation of sigmoidal, mainly progradational, sedimentary bodies. At subsequent time steps, more aggradational and tabular sedimentary bodies are obtained, showing a basinward transition from coarse- to fine-grained sediment type (figs. 5.1.7B and 5.1.7C).

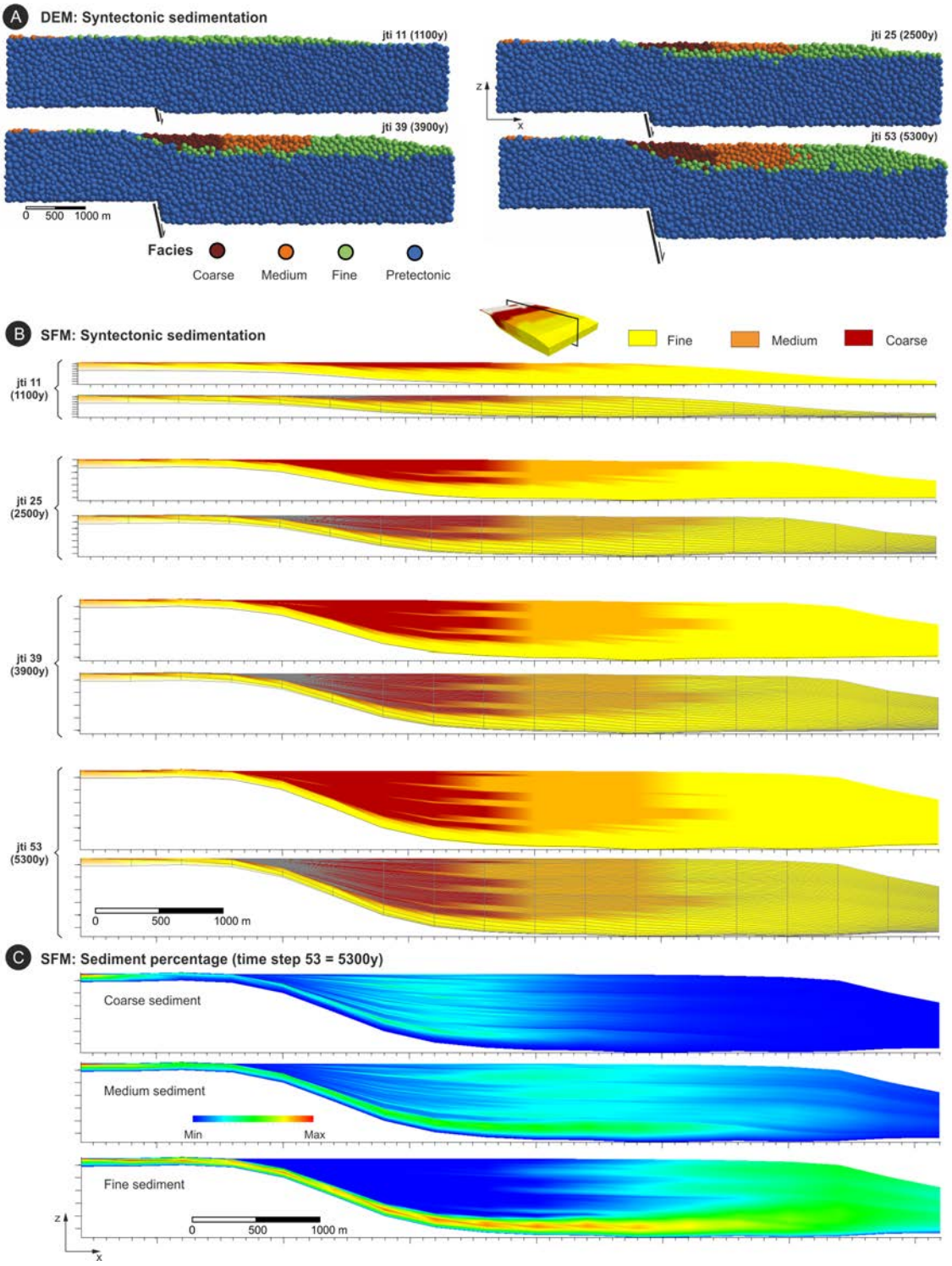

Figure 5.1.7. Cross-section showing the evolution of the syntectonic sedimentation, for the one-fault configuration model with a deformation velocity of 10cm/y, summarised in four representative time steps (jti): 11 (1100 y); 25 (2500 y); 39 (3900 y); and 53 (5300 y). A. Syntectonic sedimentation in the different time steps using DEM and coloured in function of the dominant sediment type (see cross-section position in fig 5A). B. Visualization using the SFM model results for the syntectonic sedimentation and coloured also by the dominant sediment type. Two cross-sections are represented per each time step in order to show the sedimentary architecture. C. Deposited sediment percentage at time step 53 per each clastic sediment type.

5.1.3.2-Experiment 2: one distal normal fault

In the second experiment, a distal normal fault located 4 km away from the boundary source area is defined (fig. 5.1.2B). The same deformation and sediment parameters as in experiment 1 are used for DEM and SFM. Under these conditions, sample experiment results (fig. 5.1.8) show dominant sediment type distributions that are similar to the ones obtained from the first experiment. Only the model with a deformation velocity of 10 cm/y is summarized in this contribution because it is the most complete and detailed, and hence can be better compared to othet experiments.

The dominant sediment type distribution in experiment 2 has a similar width pattern like in experiment 1, but is located in a more distal part. The same behaviour in the progradation-aggradation trend is obtained. In experiment 2, the footwall area is larger than in the first experiment, and the hangingwall is narrower, which leads to less accommodation space. Therefore the fine-grained sediment type has less representation compared to the first experiment as it is outflowing the model. Like in the previous experiment, no significant changes in sediment distribution can be observed parallel to the fault strike.

Deformation is also comparable to experiment 1, and a trishear deformation zone can be observed basinward near the fault (fig. 5.1.8A). Small tectonic deformation events in the hangingwall are also present and produce similar retrogradation / progradation / aggradation cycles in the sedimentary record.

5.1.3.3-Experiment 3: two overlapping normal faults linked by a relay ramp

The third experiment considers two overlapping normal faults linked by a relay ramp. The normal faults are located 2.5 and 4 km from the inflowing boundary (see configuration in fig. 5.1.2C). They overlap for 2 km and are separated by a distance of 1.5 km. The same sedimentary parameters and deformation velocities (2, 5 and 10 cm/y) as in experiments 1 and 2 are applied.

The experimental results are summarized in fig. 5.1.9, showing the dominant sediment type distribution for each deformation velocity in three different time steps (from 0 to 20; 20 to 40; and 40 to 60). It can be observed that the sedimentation pattern in the footwall is the same as in the previous experiments, with a narrow strip close to the inflowing boundary dominated by the medium-grained terrigenous sediment type and grading to the finest one basinward. Therefore, the analysis mainly focuses on sedimentation in the hanginwall. In this third experiment, the transition between the

footwall and the hangingwall in map view shows a left-stepping faults arrangement, which is recorded in the syntectonic sediments.

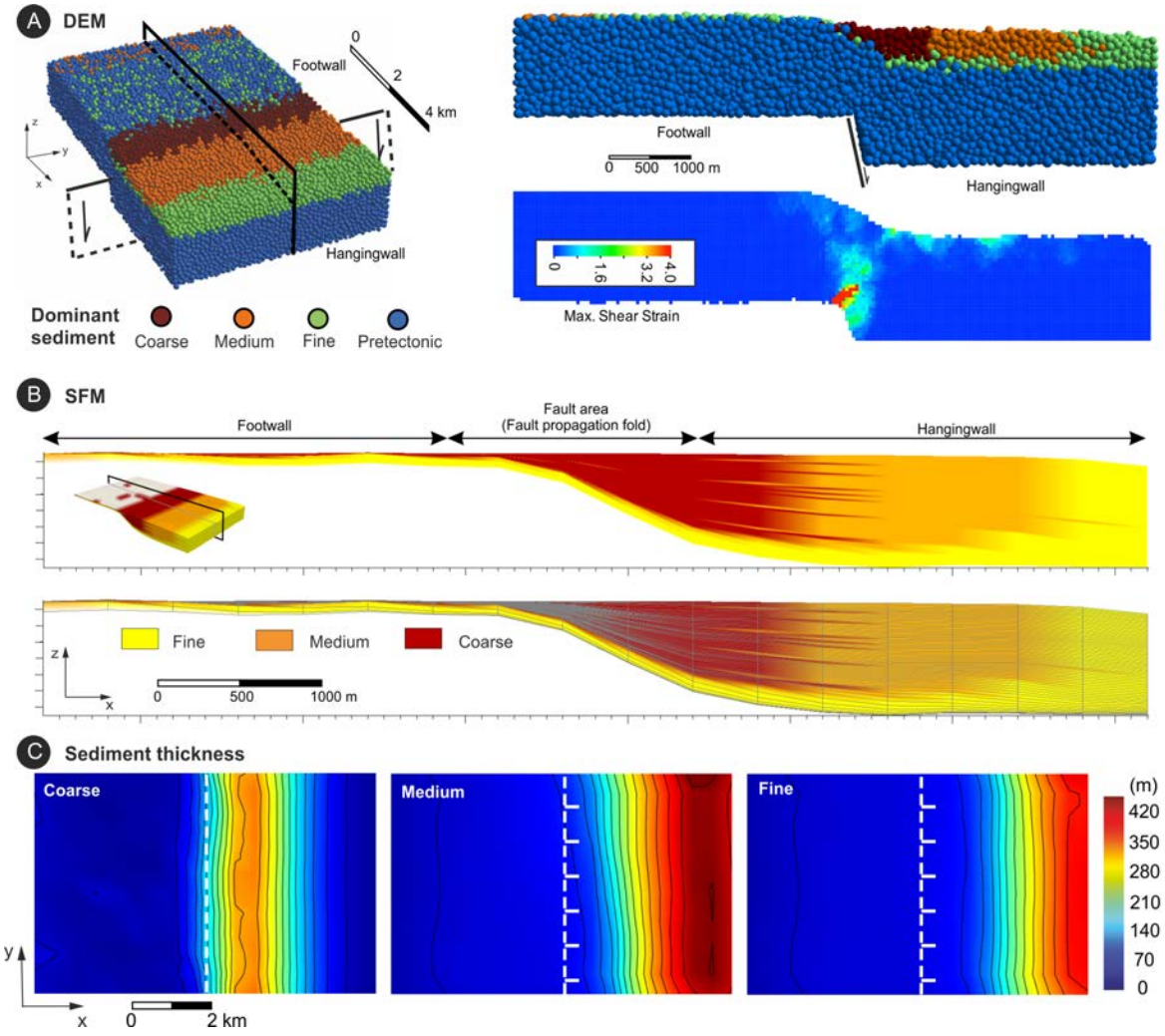

Figure 5.1.8- Second experiment results considering a one distal normal fault. A. DEM results in a 3D oblique view and a cross-section coloured by the dominant sediment type. Maximum shear strain is also included showing the trishear deformation zone and the deformation in the hangingwall. B. Equivalent SFM results for the syntectonic sedimentary infill showing the dominant sediment type distribution.

Considering the lowest deformation rate of 2 cm/y (fig. 5.1.9A), most of the fine- and medium-grained sediment just settles during the first time steps in a prograding trend, infilling the initially available accommodation space. Once filled, sedimentation is transferred to the hangingwall area and is controlled by the subsidence rate that allows a mainly medium to coarse-grained sedimentation. Low deformation velocity rates imply less available accommodation space and high fluid flow velocities that transport the fine-grained and a part of the medium-grained sediment out of the model. No dominant lateral changes of sediment type are observed. Since sedimentation takes place mainly in the first

time steps infilling the initial available accommodation space, the normal faults configuration and the presence of the relay ramp is not reflected clearly in sediment distribution of the finest sediment, while medium- and coarse-grained distribution is. Once the deformation velocity controls the accommodation space, medium- and coarse-grained sediments show an asymmetric distribution parallel to the faults strike and are controlled by the tectonic setting which reflects the presence of the normal faults.

For the 5 cm/y deformation velocity configuration (fig. 5.1.9B), sedimentation of the fine-grained sediment also takes place mainly in the first time steps, but, the higher deformation velocity produces more available accommodation space in the hangingwall during the same time interval (from 0 to 20). This allows for an increase of deposition volume towards the distal area. The sedimentation of the medium- and coarse-grained materials also reflects the asymmetric deposition geometry of the hangingwall. This asymmetry is more evident in the coarse-grained sediment deposition area sited close to the normal faults. Even taking into account these differences, in this model, a lateral dominant sediment type change can be observed basinward from coarse- to medium-grained sediment type (see 3D oblique view for the DEM results in fig. 5.1.9B), but describing a linear trend nearly parallel to the inflowing boundary without reflecting the presence of the normal faults.

In the simulation with a deformation rate of 10 cm/y (figs. 5.1.9C and 5.1.10A), the dominant sediment type distribution broadly follows the same arrangement like in the previous models. The sedimentation pattern, however, is now more clear and defined. The dominant sediment type trend is less wide and proximal, two lateral grain-size changes from coarse-grained to medium- and fine-grained sediment are obtained in the hangingwall, and the stratigraphic record is more complete. Parallel to the fault strike, maximum sediment thickness shows great differences in respect to the sediment grain-size, ranging from a more linear trend parallel to the faults for the finest one, and a localized one for the coarser mainly near the proximal fault (fig. 5.1.9C and the stratigraphic logs SL1 and SL2 in fig. 5.1.10A). This result in slightly left-stepped parallel to fault trend for the coarse- to medium-grained dominant sediment type transition (fig. 5.1.10A, *lfc1*), and a linear trend for the medium- to fine-grained transition (3D oblique view in fig. 5.1.9C and fig. 5.1.10A, *lfc2*). Note that both transitions are not reflecting the real fault geometry.

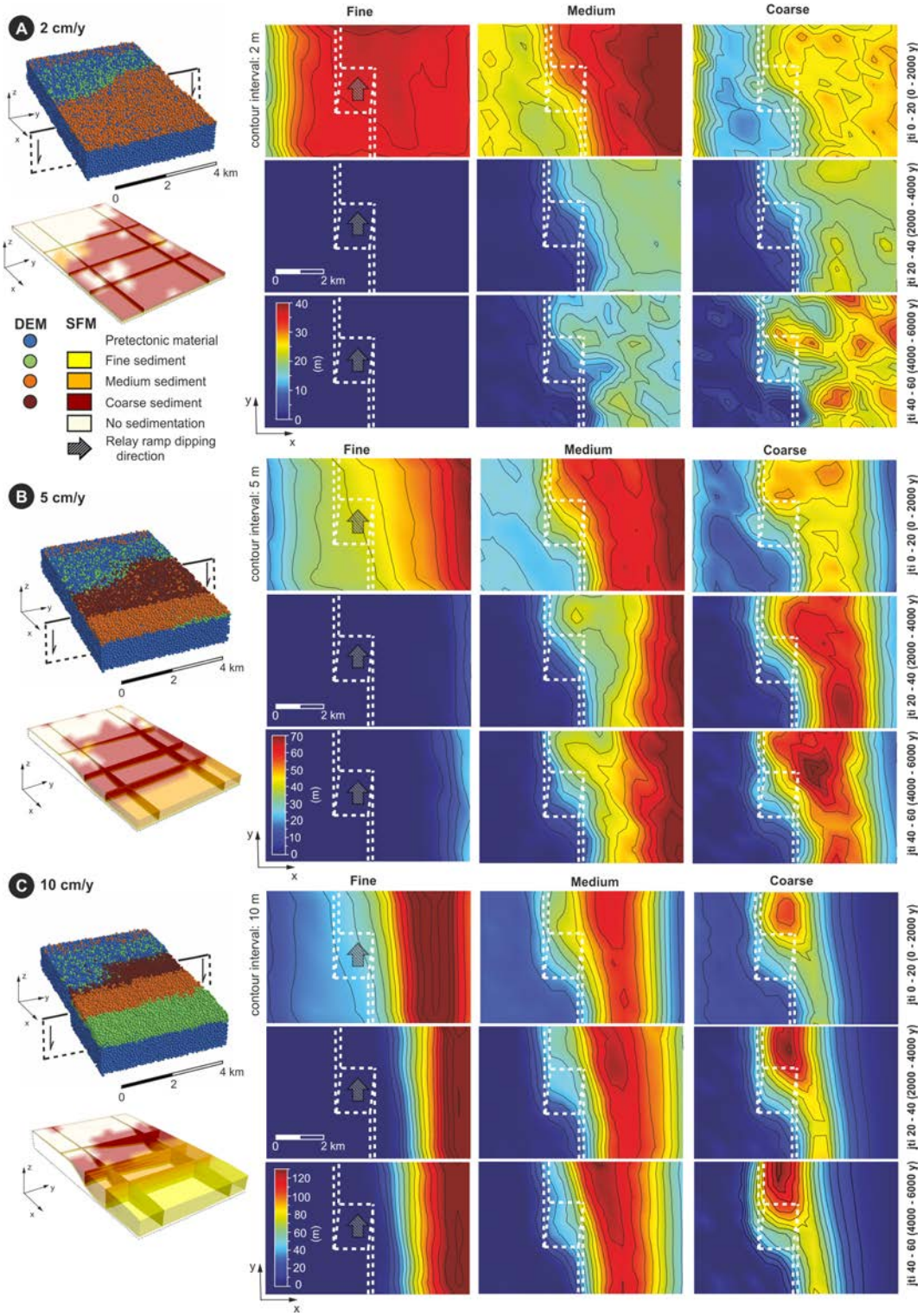

Figure 5.1.9- Sediment thickness for each fine-, medium- and coarse-grained sediment type deposited (map view) in three different time intervals (0-20; 20-40; and 40-60) under the deformation velocity of: 2 cm/y (A); 5 cm/y (B); and 10 cm/y (C) considering the third experiment with two normal faults and a relay ramp. An oblique view of the final stage for DEM and SFM (with some cross-sections) are also represented and coloured by the dominant sediment type. Fault geometry is also projected in map view in order to stand out the relationship between fault geometry and sediment distribution. Note the different scales and contour interval for sediment thickness.

The maximum shear strain is also calculated in the pretectonic sediments for this third experiment (fig. 5.1.10B). The maximum deformation is concentrated along the trishear deformation zone located above each normal fault. The deformation above each normal fault decreases towards the centre of the model where faults are overlapped in the relay ramp. Deformation in the hangingwall is also present and produces the same stratigraphic arrangement (progradation/retrogradation/aggradation) that can be observed in the previous experiments.

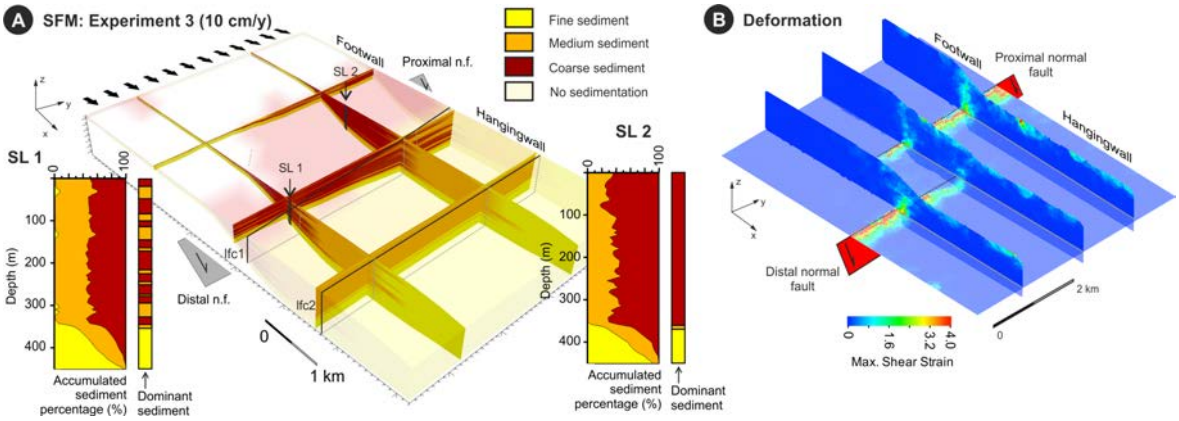

Figure 5.1.10- Final stage for the third sample experiment considering a deformation velocity of 10 cm/y. (A) Dominant sediment type distribution for the syntectonic sediments, showing the basinward transition from coarse- to medium- and fine-grained sediment with a grain-size lateral trend transition following a slightly parallel to fault linear trend for the first one (lfc1 coarse to medium) and a strictly parallel to fault linear trend for the second one (lfc2 medium to fine). Two stratigraphic logs (SL1 and SL2) located at the same distance basinward from each fault (1 km) are also included in order to compare the sediment percentage. Note that SL1 has less coarse-grained sediment than SL2 and rapidly decrease basinward. At the same structural position, coarse-grained sediment is settled mainly near the proximal fault while in the distal fault coarse-grained sediment is located in a narrow strip close to the distal fault area. (B) Cross-sections for the maximum shear strain showing the trishear deformation zone related to each normal fault and decreasing towards the centre of the model where faults overlap. As in the previous experiments, deformation is also obtained in the hangingwall.

5.1.3.4-Comparison of all experiments

In order to compare the sediment distribution of the three experiments, the results obtained by the deformation velocity of 10 cm/y are considered for each configuration. Since the models with a deformation velocity of 10 cm/y produce the most pronounced sediment distribution patterns, only the results of those experiments are compared. The figure 11 shows the sediment distribution of each sediment type, coarse-, medium- and fine- grained material, for each experiment. In this figure, the sediment distribution is represented through the percentage contribution of each sediment type in the stratigraphic record. It can be noticed that the main difference in sediment distribution is found in the

third experiment, in which the medium- and coarse-grained sediments are distributed non-parallel to the strike faults distribution (see the grey rectangle in fig. 5.1.11C).

Taking into account the results of the experiment 1 and 2 (figs. 5.1.11A and 5.1.11B), an equivalent grain-size distribution in the hangingwall area in front of each normal fault for the third experiment would be expected. The resulting dominant sediment type trends in the third experiment (fig. 5.1.11D) would be expected to be parallel to each faults strike, with a similar width in each fault, and a basinward transition from coarse- to medium- and fine-grained sediment. Due to the overlapping normal faults, and the presence of the relay ramp, another dominant sediment type trends would be also expected on the relay ramp. These new sediment type trends would show an oblique to normal fault strike direction (see OB in fig. 5.1.11D), joining both previous, parallel to the faults, trends.

In contrast, this is not observed, but differences in sediment percentage parallel to faults are obtained, mainly for the coarse- and medium-grained sediment type due to its more proximal deposition. Thus, a different sedimentation pattern is obtained in the hangingwall area in front of each normal fault. The maximum percentage of coarse- and medium-grained sediment close to the proximal fault is 75% and 65% respectively, while at the distal fault both sediments types decreases to values around 50%. This is as a consequence of the relay ramp geometry, which produces a substantial decrease of the accommodation space in the hangingwall area close to the proximal fault. This leads to higher fluid flow velocities in this region than in the hangiwall area of the distal fault (fig. 5.1.12). The higher velocities facilitate the sedimentation of the coarse-grained sediment, while the sedimentation of medium-grained material is moved basinwards in relation to the position of the proximal fault. The deposition of fine-grained sediment shows no clear differences, because its sedimentation takes places mainly basinwards where the fluid flow velocity profile is not affected by the normal faults configuration.

Moreover, the dominant sediment type trends for this third sample experiment (upper oblique 3D view in fig. 5.1.11C) are effectively parallel to the normal faults but the coarse-grained facies practically disappears from the proximal to the distal normal fault. The medium-grained dominant sediment type trend is also linear and does not show lateral differences parallel to the fault strike (e. g. compared with the second experiment). In general, dominant sediment type trends are not clearly reflecting the presence of the relay ramp (only the boundary close to the faults that separate the footwall and the hangingwall), but the faults position and the relay ramp strongly determines the final coarse- and medium-grained sediment deposition area.

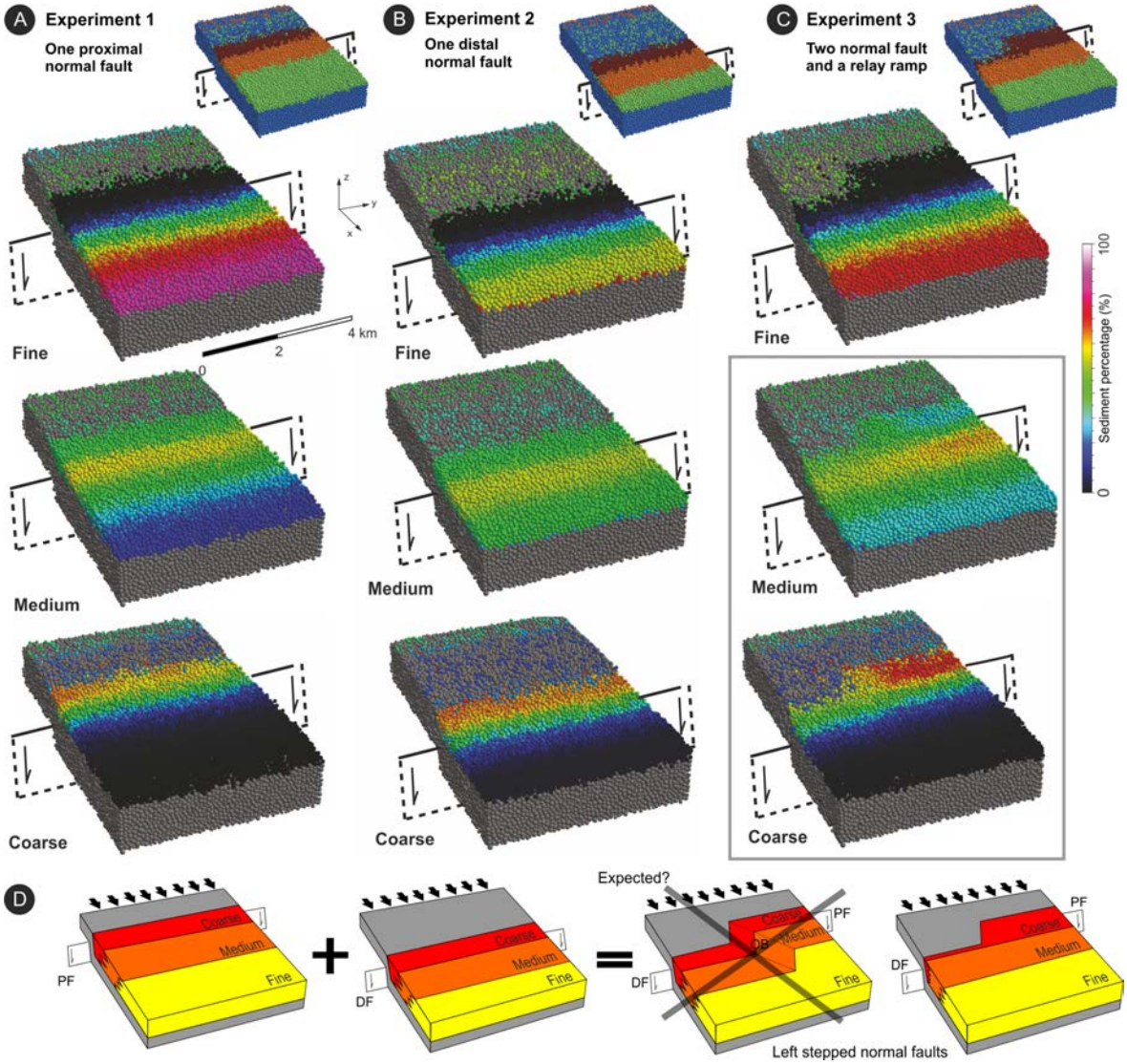

Figure 5.1.11- Sediment thickness (in percentage) for each sediment type (fine, medium and coarse), at the end of the simulation time and considering the 10 cm/y deformation velocity option, for the three configurations: one proximal normal fault (A); one distal normal fault (B); and two overlapped normal faults linked by a relay ramp (C). The dominant sediment type trends are also included in the upper 3D oblique view (see legend in the previous figures). Grey rectangle marks the parallel to fault maximum differences in sediment deposition for the medium- and coarse-grained sediment. An expected dominant sediment type trends from the different fault configuration and the obtained one are also designed (D). PF: Proximal normal fault; DF: Distal normal fault; OB: Oblique band for the dominant sediment type trend expected on the transfer zone.

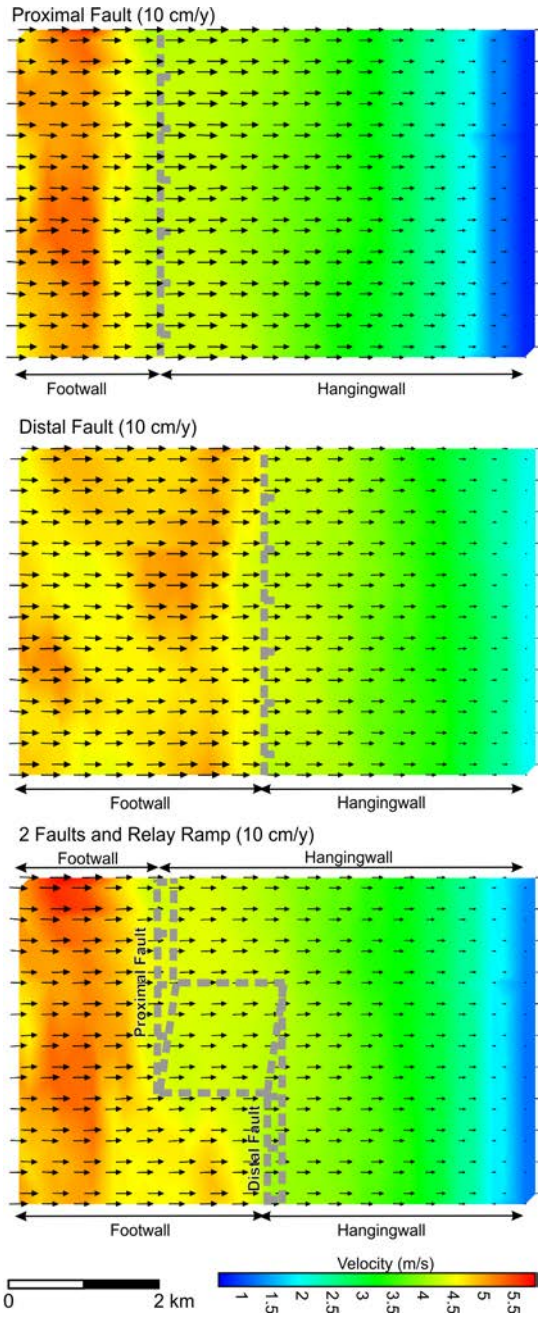

Figure 5.1.12- Fluid flow velocity maps at the end of the simulation time for the three different configurations: one proximal normal fault; one distal normal fault; and two overlapping normal faults linked by a relay ramp. The three configurations are considering the higher deformation rate (10 cm/y). Fluid flow velocities for the proximal and distal fault configurations show similar values in the hangingwall area for both configurations, regardless of the position of the fault. In contrast, in the two faults configuration, different velocities can be observed in the hangingwall area in front of each normal fault: these velocities are higher close to the proximal fault than in the distal fault. This difference is as a consequence of the relay ramp geometry, and facilitates the deposition of mainly the coarse sediment in front of the proximal fault rather than the distal fault. Therefore, an asymmetric grained-size sediment distribution is obtained on the hanging wall area in front to each normal fault.

5.1.3.5-Changing the source area

To study the effect of the relay ramp on sedimentation, the position of the source area is changed from regional to punctual (PSE) while water and sediment supply remains constant. The 10 cm/y deformation velocity used in the previous setups is also used as a fixed parameter in this case, as the experiments with this velocity results in the most complete stratigraphic record.

The new positions represent: in one case, river inflow transverse to the normal faults (centre PSE, fig. 5.1.3 B), and in the other two cases river inflow parallel to the faults, from opposing sides (left PSE and right PSE, figs. 5.1.3 C and 5.1.3 D respectively). The

results of the point source experiments (PSEs) are shown in figures 5.1.13 and 5.1.14, along with the results of the experiment with regional source boundary (RSBE) for comparison.

On the footwall, the main difference that can be observed between the PSEs and the RSBE is that sedimentation in the PSEs is less close to the inflowing points than in the RSBE (striped area in fig. 5.1.14 A). This is a consequence of higher fluid flow velocities ahead of the point sources compared to the front of the regional source boundary, as water discharge is concentrated in fewer nodes instead of a boundary (fig. 5.1.3). Sediment distribution on the footwall of the PSE also differs from the distribution in the RSBEs. Maximum sediment accumulation is defined by roughly radial map patterns for the PSEs, whereas the RSBE outputs a more linear map patterns (fig. 5.1.14 A1). The outputs of PSEs show that sediment accumulation and grain-size distribution relate in their position to the source point location (figs. 5.1.14 A2, A3 and A4).

In the hangingwall and the relay ramp area, the main difference in the dominant grain-size maps can be observed in the left and right PSEs (figs. 5.1.13 C and 5.1.13 D), showing curved patterns by contrast to the linear patterns of the centre PSE and RSBE (although its different source area definition) (fig. 5.1.13 A and 5.1.13 B).

Regarding to the centre PSE, and taking into account the sediment accumulation for each sediment type (fig. 5.1.14A2), the coarse- and medium-grained sediments deposition show some differences when compared to the results obtained in the RSBE, despite that both experiments show the same dominant grain-size trend. In the centre PSE, coarse-grained sediment is settled mainly on the relay ramp, representing almost 100% of sediment settled (see the stratigraphic log in fig. 5.1.14 B2), while in the RSBE coarse-grained sediment on the relay ramp is lesser (60%) and shows a maximum near the proximal fault (see figs. 5.1.14 A1 and B1). For the fine-grained sediment that settled in distal areas, the same distribution for both experiments can be observed. For the right and left PSEs, and also considering the sediment accumulation in the hangingwall (figs. 5.1.14 A3 and A4), a roughly radial map pattern and a grain-size distribution from the source area is obtained. However, higher and more concentrated accumulation values are obtained in the right PSE and near the source area (fig. 5.1.14 B3) compared to the left PSE (fig. 5.1.14 B4). Even so, the dominant sediment type distribution pattern of both, left and right PSEs, are similar (but, obviously, in a symmetric position).

Cross-sections perpendicular to the relay ramp for the two experiments with a right and left source area location, show a common basal stratigraphic unit with rather homogeneous and fine-grained dominant sediment type, overlain by a thick and coarser-

grained unit with differences in dominant sediment type distribution (figs. 5.1.15 A and B). Both PSEs have most of the coarsest sediment deposits in the hangingwall area closer to the inflowing point, e.g. at the foot of the relay ramp, adjacent to the proximal fault, for the right PSE, and adjacent to the distal fault for the left PSE. The overall geometry of the basin fill remains similar. Other differences arise in detail during the following time steps:

- Time interval 0 - 4 (400 y):

A progradation (and aggradation) pattern to the left (right PSE) or to the right (left PSE) can be observed in both experiments (figs. 5.1.15 A and 5.1.15 B). Sigmoidal sedimentary body geometries are obtained and typical backset, foreset and bottomset geometries can be observed. A short topset bed transition is only observed in the right PSE. A basinward grain-size transition from coarse- to medium- and fine-grained sediment in each time step is recorded in both experiments.

- Time interval 4 - 9 (500 y; total simulated time is 900 y):

In this time interval, the left PSE follows with an apparent aggradation-progradation (or a lateral migration, since the cross-section is parallel to the faults) due to the larger subsidence in the distal area to the source, where, consequently, more accommodation space is available. Topsets develop in this interval, and new sigmoidal bodies are thinner than the precedent ones. A change in the topset breakpoint path can also be observed, i.e. the path is dipping less than in the first time steps, marking higher progradation rates. On the other hand, in the right PSE, the stratigraphic pattern shows two apparently opposing lateral migrating bedsets. The bedset on the right, close to the source, is a backset (fig. 5.1.15C) and it is coarser-grained than the bedset on the left (more distal to the source), which is a foreset. The development of the coarse-grained backset is favoured by the locus of maximum subsidence near the inflowing source area. Finer-grained sediment is transported away, to be laid aside of the depositional topography created during time interval 0-4.

- Time interval 9 - 60 (5100 y; total simulated time is 6000 y):

In this time interval, sedimentation is mainly located on the hangingwall and on the relay ramp. As subsidence progresses, the new sedimentary infill records an expansion from the footwall to the hangingwall where a maximum expansion exists and tilted clinoforms can be observed in both experiments. In the left PSE, backsets, topsets and foresets are recorded (perpendicular or parallel to fault strike). In the right PSE, topsets and backsets are recorded parallel to the fault orientation, while foresets occur only basinwards perpendicular to the fault strike (fig. 5.1.15 C, time step 60). It is important to highlight that

the basal stratigraphic unit (time steps 0 to 9) undergoes rotation and deformation, changing the initial sedimentary geometry. While at the end of the simulation time the left PSE continues recording the same relationships, in the right one, an unexpected termination occurs, expressed by strata within sedimentary trends (fig. 5.1.15 B, time step 60). Here, an onlap and a truncation are observed where initially a downlap and toplap respectively had been recorded at the top of the relay ramp. Moreover, basinward no downlap terminations are observed compared to the left PSE.

Considering the dominant grain-size distribution, an expected distribution can be observed in the left PSE and a basinward transition from coarse- to medium- and fine-grained sediment can be observed, with the medium- and fine-grained sediment settled where maximum subsidence exists. In the right PSE, and considering only the basin geometry, an erroneous left source area location could be deduced. Adding the lithological information obtained in the experiment (fig. 5.1.15B) to this basin geometry, an unexpected (and an opposite) sedimentation pattern could be observed, with the coarse-grained sediment settled where maximum subsidence exists and grading to the finest one upwards.

Fluid flow paths for the right PSE (fig. 5.1.15C, lower fig 3D oblique views) show a great influence of the fault configuration and the related main subsidence areas. Changes in magnitude and direction can be found to control the resulting sedimentation pattern.

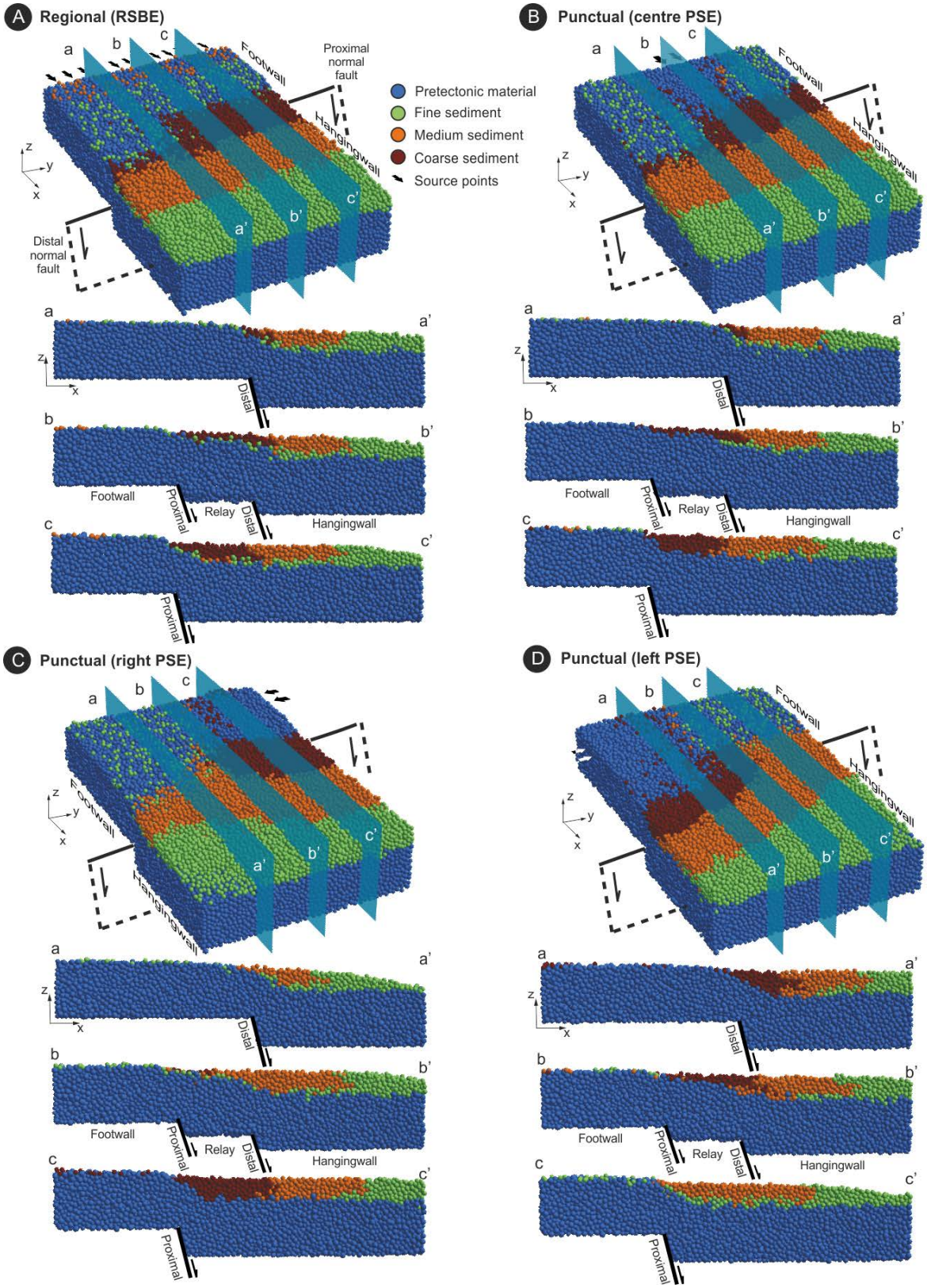

Figure 5.1.13- Oblique 3D view for the dominant sediment type distribution from DEM for the syntectonic (coloured particles) and pretectonic sediments (blue particles) obtained for the third sample experiment (considering a deformation velocity of 10 cm/y) where source area location is changed (from A to D). Three perpendicular to faults cross sections are also included for each one.

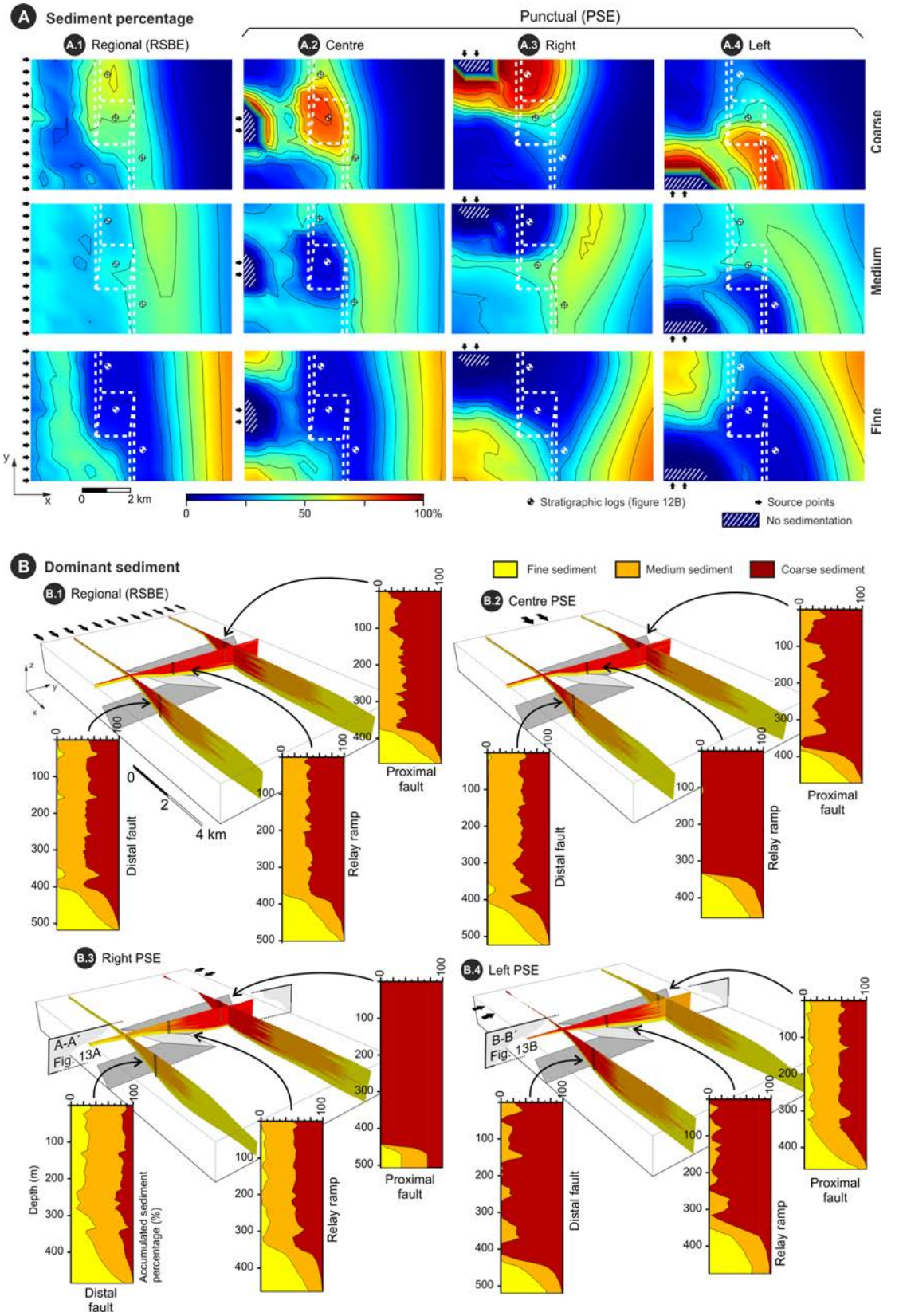

Figure 5.1.14- A. Sediment thickness (in percentage) of the syntectonic sedimentation from SFM for the third sample experiment (two normal faults with a relay ramp and considering a deformation velocity of 10 cm/y) changing the source area location (from A.1 to A.4, see black arrows). B. Oblique view for dominant sediment type distribution and some stratigraphic logs (showing the accumulated sediment percentage) in the proximal, distal and the relay ramp area (see location in A), for the different source area location (from B.1 to B.4).

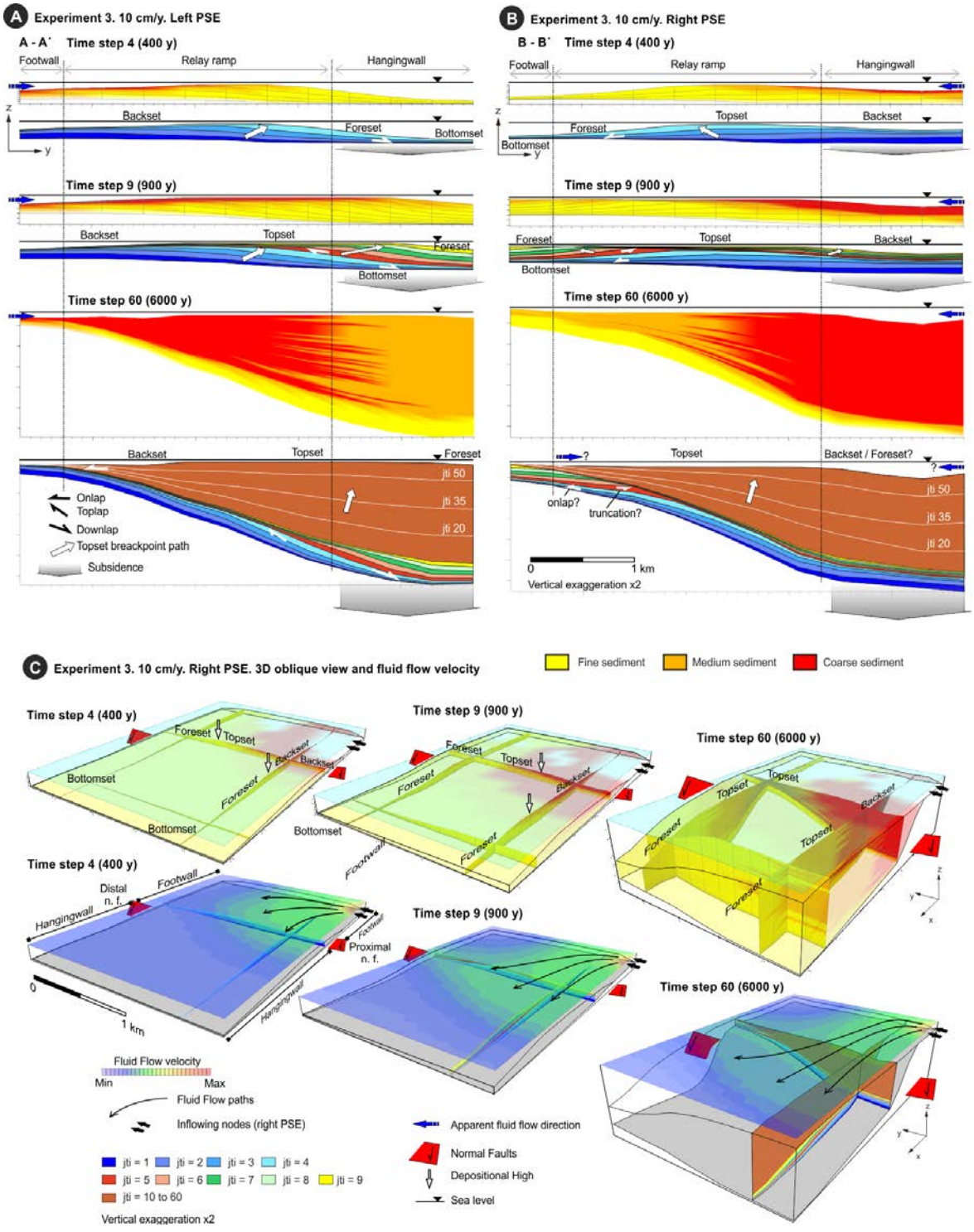

Figure 5.1.15- Evolution in three characteristic time steps (4, 9 and 60) for the third sample experiment with two normal faults and a relay ramp considering a left PSE (A) and right PSE (B). A parallel to faults (and perpendicular to the relay ramp) cross-section coloured with the dominant sediment type (and its interpretation below in function of the time step) is represented (see location in fig 14 B3 and B4). C. 3D oblique view for the right PSE at the same time steps with an interpretation and a fluid flow evolution below (see coloured contour map). See the text for a more detailed explanation. Vertical exaggeration x2.

5.1.4- Discussion

In this contribution, the first two experiments have been performed to study the facies distribution and sedimentary geometries with a simple normal fault configuration. The sedimentary conditions are fixed and three different fault slip rates are applied. Considering that sedimentation parameters define an overfilled sedimentary system, the modelling results show a sedimentary infill that covers the extensional faults and the relay ramp. Thus, the resulting basin bathymetry, which controls the fluid flow system, is a combination of the extensional system, and the sedimentation. Deposition takes place mainly in the hangingwall area where more accommodation space is created and a basinward progradation and transition from coarse- to medium- and fine-grained sediment type is obtained (figs. 5.1.5, 5.1.7 and 5.1.8). The sedimentary infill is mainly controlled by the deformation rate, and the most complete syntectonic succession is obtained with higher fault slip rates (figs. 5.1.5 B and C). The deformation rate also controls the facies trends width and the geometries of the sedimentary bodies (e.g., as described by Athmer et al. 2011), obtaining larger-scale clinoforms with the lower slip rate fault value (fig. 5.1.5 C).

The presence of overlapping normal faults linked by a related relay ramp (experiment 3) produces differences in the sedimentation pattern compared with the previous experiments. These differences are lager and more obvious when high fault slip rates are considered. The presence of the left-stepped normal faults produces a distribution non-parallel to fault strike, and an asymmetrical deposition of the different grain-size materials (fig. 5.1.9, 5.1.10 A). These asymmetries are more evident in the coarse-grained sediment (fig. 5.1.9 C) because it settles near the faults in the hangingwall area. Thus, the sedimentation of the coarse-grained sediment type between both faults reflects the position of the relay ramp. Coarse-grained sedimentation is more relevant over the relay ramp area and in the area adjacent to the proximal fault (foot of the relay ramp) than in the area close to the distal fault. This is justified by the left-stepped fault geometry and the relay ramp position, which strongly controls and produces maximum differences in the fluid flow velocity in the hangingwall area in front of each normal fault (fig. 5.1.12). The relay ramp produces a substantial decrease of accommodation space in the hangingwall area, close to the proximal fault. This results in higher fluid flow velocities in this region in relation to the hangingwall area adjacent to the distal fault. These higher velocities facilitate mainly the sedimentation of coarse-grained sediment in this area, and also force a basinward progradation of medium-grained sedimentation in this region. As a result, another

asymmetry in the sedimentation pattern is obtained when comparing the hangingwall area of the proximal fault with the hangingwall area of the distal fault.

The distribution of the finest sediment shows fewer differences compared to the experiments 1 and 2 due to its deposition in the more distal parts of the basin, far away from the fault influence. Although these differences between each normal fault can be clearly noticed, e.g. for the coarse sediment in the 10 cm/y fault slip rate, the dominant sediment type distribution trends are (almost) parallel to the fault strike (fig. 5.1.10 A), without reflecting the presence of the overlapping normal faults linked by a relay ramp.

Smaller fault slip rates produce less accommodation space, which results in a higher (and more constant along the strike fault direction) fluid flow velocities. Considering that the inflowing sediment amount remains constant in each experiment, more sediment is spread basinward, and the lateral differences of the settling pattern of the different sediment types are less noticeable (e.g. the finest-grained sediment type flows out of the model in jti 20-60, fig. 5.1.9 A, or coarser-grained sediment type has similar settling patterns near both faults for lower deformation rates). Hence, the influence of the geometry of overlapping normal faults linked by a relay ramp geometry on deposition of different grained-size materials decreases with lower fault slip rates.

With regard to the source area location (PSEs), sediment distribution is mainly conditioned by the extensional faults configuration and available accommodation space in relation to the source area position (fig. 5.1.14). Thus, the deposition of the coarse-grained sediment type is located mainly in the hangingwall area of the proximal or distal fault or on the relay ramp as the PSE is defined as right, left or centre depending on the position of the source point (fig. 5.1.14 A). The grain-size arrangement is also produced according the transport direction. Therefore, it is also remarkable differences in the dominant sediment distributions on the hangingwall area among the different PSEs; the dominant sediment trends are nonlinear for the lateral PSEs (figs. 5.1.13 C and D), while the centre one (fig. 5.1.13B) shows the same linear and parallel to fault strike trend as can be observed in the regional one (fig. 5.1.13 A.) Great differences between each experiment are observed on the footwall, where sediment distribution is dominantly controlled by the source area location and the available accommodation space during the first time steps.

Due to the presence of a relay ramp during syntectonic sedimentation, initial depositional sedimentary geometries can be deformed and rotated as the deformation progresses (as pointed out by Gupta et al. 1999), loosing initial, and sometimes geologically coherent, relationships. This, combined with incomplete or poor information, may result

into erroneous interpretations when analysing other data such as seismic profile, e. g. the initial downlaps and toplap that could be interpreted as erroneous onlap and truncation in an hypothetic seismic profile corresponding to the final stage in experiment 3 (fig. 5.1.15 B).

The experiments presented in this contribution may differ from other experimental studies (Athmer et al. 2010) or field case studies (Young et al. 2001, Bruhn and Vagle 2005, Fugelli and Olsen 2007) because here sediment deposition is not related to gravity flows. A more proximal situation of extensional faults in relation to the sediment source area is studied, and an overfilled sedimentary system with high sedimentation rates and low deformation rates is considered. As pointed out by Athmer and Luthi (2011), this situation can be related to the later stages of the rift evolution.

Even though the presented experiments may be relatively simple compared to real, natural cases (such as in the Corinth Rift, the Gulf of Suez Rift, the Aptian-Albian Basque-Cantabrian basin), they can provide better understanding of some parts of these geological systems. Future work can include other configurations and parameters (e. g., changing fault overlap or fault distance, adding footwall uplift, including sediment discharge variations, or different eustatic curves), in order to increase the geological complexity and the comparison with more realistic examples or analogues.

5.2 THE EFFECT OF SYNTECTONIC SEDIMENTATION ON FOLD GEOMETRY: INSIGHTS FROM NUMERICAL MODELLING.

5.2.1 Introduction

Syntectonic sediments and their internal architecture have been widely studied to understand the kinematic mechanics and evolution of different geological systems and structures. In compressional environments, deformation factors such as axial surface activity, fold uplift or limb rotation, together with the sedimentation, control growth strata patterns. Taking this into an account, several kinematic (Shaw et al., 2004) and numerical models (Cooper et al., 2003), have been proposed to associate the different syn-sedimentary growth strata to different styles of fold geometries, (e.g. fault-bend folds, fault propagation folds, fixed limb length decollement folds), in 2D (Storti and Poblet, 1997), and also in 3D (Salvini and Storti, 2002, Bernal and Hardy, 2002).

On the other hand, the syntectonic sediment deposition can also influence the evolution of the deformation in compressional systems, since the final structures are consequence of the interplay between orogeny and surface processes. Nonetheless, the effect of new sediments in the structure style or on fold geometry is more complicate to determine, because it practically impossible to have direct access to this interaction, as only the final stage can be observed. Therefore, it is complicated to derive conclusions directly from the geological record. For this reason, analogues (Barrier et al., 2002, Duerto and MacClay, 2009) and numerical models (Fillon et al., 2013), are useful tools to investigate the effect of syntectonic sedimentation in compressional environments, since these models allow a direct interaction in the evolution of the geological system along the simulation time.

Considering this, the numerical model presented in this thesis is used to study the effect of syntectonic sedimentation on fold geometry, specifically related to a deltaic progradation surrounded by two growing anticlines.

The present numerical model has various advantages over other models and contributions for studying the effect of syntectonic sedimentation on fold geometry. First, it is a 4D model, which gives a proper 3D image evolution over time, i.e., geometry, internal architecture, and growth strata in 3D over time. Second, the model has the reciprocal interaction deformation-sedimentation where each process receives the feedback from the complementary process (see chapter 3), therefore the final structure is a result of both processes together. And third, since the sedimentary model is a process-based model, the

sediments settle in the model as a consequence of processes of the fluid flow, transport and sedimentation. Therefore, new sediments are affecting different areas of the emerging structures in different stages of the deformation, according to the sedimentary processes, which gives a complete sense to a 3D model.

5.2.2 Sample experiment application - Experiment setup

5.2.2.1 Initial set-up, boundary conditions and experimental parameters

The initial experiment set-up is built by an initial DE assemblage formed by 116950 spheres of four different radii: 200m, 175m, 150m and 125m, which are allocated in a volume of 30000m x 30000m x 3000m (fig. 5.2.1 A). The particles are defined with initial cohesion, with a breaking threshold value of 0.01R, where R is the equilibrium separation between the particles. A thin layer with a breaking threshold value of 0.0001R is also defined at the base of the model, in order to simulate a detachment level (fig. 5.2.1 B). 930 nodes and 1740 triangular elements configure the FE mesh used to solve the equation that manages the different sedimentary processes. The separation between nodes is 1000m (fig. 5.2.2). The initial model is initially tilted 1.6 degrees with an increasing water depth in ***y*** direction ranging from 51 to 861 m. (fig. 5.2.1 C). The total simulation time is 800ky and the information is saved every 8ky giving a total of 100 time steps *jti*.

5.2.2.2 Displacement and shortening rates

In order to deform the pretectonic unit and to obtain different fold uplift rates, different shortening rates are defined using a pushing wall movement perpendicular to *y-axis* and from right to left (hereinafter *shortening direction*). Moreover, at the bottom, two velocity discontinuities perpendicular to the shortening direction are defined (fig 5.2.1 D). These two discontinuities act as breaking points that unleash in the formation of two folds. The relative shortening rates over the discontinuities at the bottom defines the fold uplift.

Four different shortening rates of 0.2mm/y, 1mm/y, 2mm/y, and 4mm/y are considered over each discontinuity (V_1 i V_2 in figure 5.2.1D), in order to obtain the following fold uplift rates: 0.1mm/y, 0.5mm/y, 1mm/y, and 2mm/y respectively.

Moreover, two particular cases have been considered for the 2mm/y and 4mm/y shortening rates, where one fold has been inhibited for the initial 240000 years of the simulation time. This facilitates the formation of the other fold for the initial time steps. This case has been applied for each fold and for each deformation rate (the 2 mm/y and 4mm/y shortening rates); hence, four more deformation cases are added to the initial four.

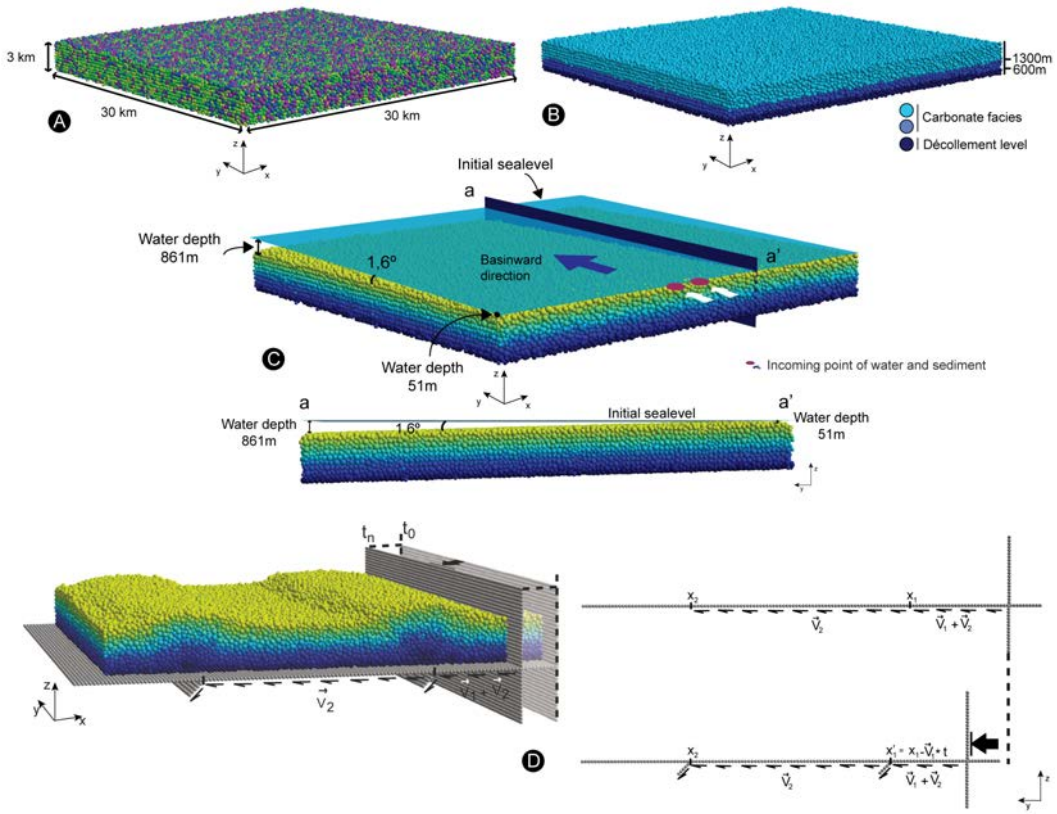

Figure 5.2.1. Initial experiment set up. A- Initial DEM coloured by element size. B- Initial DEM coloured by facies (mechanical properties). C- DEM coloured by layers and tilted 1,6º. The reddish dots indicate the incoming point for water and sediment for the sedimentary model. The initial position of the sea-level is also indicated, showing the initial bathymetry of the model. D- Boundaries of DEM illustrating the shortening direction and the discontinuities in the bottom.

5.2.2.3 Source Area and sea-level variations

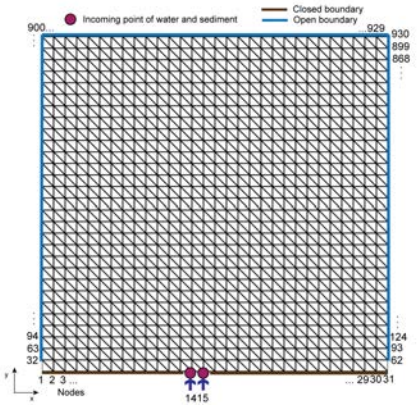

Figure 5.2.2. Finite element mesh used by the sedimentary model in the experiments. Red dot indicates the incoming point of water and sediment (source area position).

The boundary conditions simulating the source areas location (incoming points for water and sediments) are defined as a punctual through two nodes of the mesh (figs. 5.2.1C, 5.2.2 and 5.2.3). The nodes are located in the middle of the boundary with the lowest bathymetry (fig. 5.2.1C), approximately in the position of the future syncline that will be located between the two folds. The total amount for the incoming water and sediment is the same in all the experiments. Three different sediment types are introduced in the model, simulating the behaviour of fine-grained sand, silt

and clay respectively (see table 5.2.1 for the different parameters defining the amount of incoming sediment and the sediment type).

Table 5.2.1. Parameters used to define the three terrigenous sediments. Following Gratacós (2004), the critical velocity for deposition is a threshold value below which sediment can settle. Longitudinal and transversal dispersivity are defined as a function of the FE mesh discretization in order to avoid numerical errors solving the transport equation. In turn, the FE mesh is defined in function of the expected heterogeneity.

Terrigenous sediment type	Sediment supply: Fixed Rate (T/s)	Settle Rate (m/d)	Critical Velocity (m/d)	Longitudinal dispersivity (m)	Transversal dispersivity (m)
Fine	0.01	0.8	2.0	1000	1000
Medium	0.004	0.002	6.0	1000	1000
Coarse	0.001	0.0002	10.0	1000	1000

Two different lineal trends of sea-level rise rates (0.25mm/y and 0.5mm/y) are considered for each deformation rate experiment, leading to 16 experiments. Finally, one more experiment for each deformation rate is also considered, but without sedimentary processes. These last experiments without sediments are important, since they are ***reference*** models to compare with the ones with sedimentation in order to highlight the main differences. The set of experiments finally consists of 24 simulations (summarized in Table 5.2.2). In the next section, only the experiments with significant results are described, but all the results are summarized in the Appendix A.

	Wihtout sediments (reference model)			With sediments		
Shortening (mm/y)	Left Fold priority	Right Fold priority	No priority	Left Fold priority	Right Fold priority	No priority
0.2			✓			✓
1			✓			✓
2	✓	✓	✓	✓	✓	✓
4	✓	✓	✓	✓	✓	✓
	x1			x2 (Sea-level 0.25 and 0.5mm/y)		

Table 5.2.2. Set of experiments performed to study the effect of syntectonic sedimentation on fold geometry

5.2.2.4 Terminology when analysing the experiments results

For a better understanding of the results, both folds of the model will be referred as right-side anticline and left-side anticline as shown in the figure 5.2.s. Note that the shortening direction is from right to left. The terminology *backlimb* and *forelimb* is used to characterize both limbs of the anticlines in relation to the shortening direction.

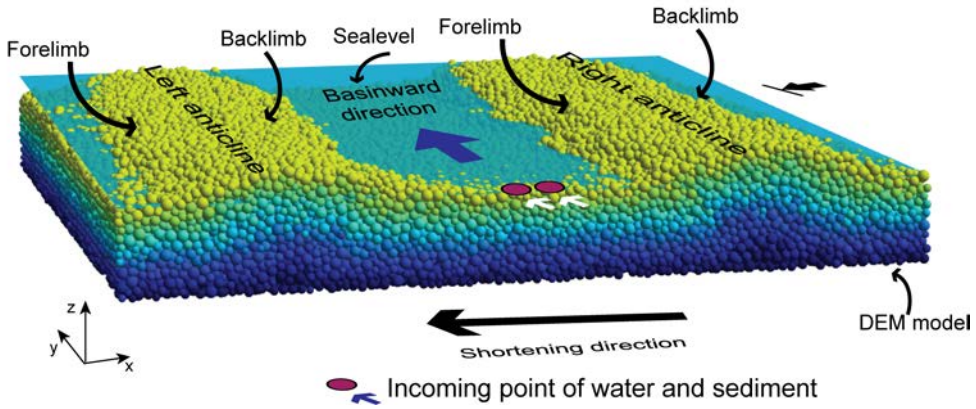

Figure 5.2.3. Figure to illustrate the terminology used in this section to explain the results in the models.

5.2.3 Results

This section analyses three experiments considering a fold uplift rate of 1mm/y: (1) without sediments; (2) with syntectonic sediments and a sea-level rise of 0.25mm/y; and (3) with sediments and a sea-level rise of 0.5mm/y. Although all the 24 experiments show interesting results, the relation between sedimentation and deformation are more well expressed in the experiments with a fold uplift rate of 1mm/y.

Evolution of the deformation

The evolution of each experiment is summarized in the figures 5.2.4, 5.2.5, 5.2.6, 5.2.7 and 5.2.8. For each experiment, three cross-sections in the right-left direction are represented in order to analyse the deformation in the proximal area (a-a'), in the intermediate area (b-b') and in the distal area (c-c'). Each cross-section shows the evolution of the DEM and the analysis of the strain (using the program SSPX). The position of the top of the pre-tectonic and syntectonic units has also been included in order to analyse the differences between the example without and with sediments.

jti 1-20 - In this initial steps, the deformation is mainly localized in the detachment level and no big differences arise between experiments (fig. 5.2.4). In the experiments considering sedimentation, the sediments are settled in the proximal area and only show slightly differences in the position of the top of the pre-tectonic unit (fig. 5.2.4D).

jti 20-40 - As deformation progress, deformation is focused on both pre-defined basal discontinuities, where the two detachment folds stars to grow (fig. 5.2.5A). Both anticlines show conjugate shear-zones and a box-fold geometry. Since the shortening direction is defined from right to left, the right-side anticline has a slightly higher uplift than the left-side anticline; therefore, its box-fold geometry is more appreciable. Considering the experiments with sedimentation, first structural differences arise when comparing with the

reference experiment. Both experiments with sedimentation present an asymmetric evolution of the left-side anticline (also with less uplift than the right-side anticline). Looking at the strain, a slightly inhibition of the deformation occurs in the left-side anticline, mainly in the proximal area (cross section a-a' fig. 5.2.5B and C) due to sedimentation is focussed on that part. The inhibition is more evident in the backlimb of the left-side anticline. Although both anticlines show deformation, it is observable how the left-side anticline has no topographical expression in the experiments with sedimentation in the proximal and middle areas (cross- sections a-a' and b-b') in comparison with the experiment without sediments. Looking at the top of the pre-tectonic unit (fig 5.2.5D, vertical exaggeration x12.5), it can be observed the inhibition of the left-side anticline. This effect is lower basinwards and disappears in the c-c' cross-section.

jti 40-60 - In this time interval, the reference experiment (fig. 5.2.6A) shows symmetric shear bands in both sides, which indicate the formation of two symmetric box-fold anticlines. Considering sedimentation (fig. 5.2.6B and C), the inhibition of the deformation in the backlimb of the left-side anticline is more evident, and now deformation is only focused in the forelimb. This inhibition results in fault propagation fold rather than a detachment fold (cross-section b-b' in fig. 5.2.6 B and C). Regarding to the right-side anticline, the forelimb of the 0.5mm/y experiment (cross-section b-b' in fig. 5.2.7 C) shows a slightly inhibition compared with the reference experiment. In this time step, it is also noticeable that the influence of sediments in the deformation of the pre-tectonic unit progress basinward. Thus, in the cross-section c-c' it can also be observed the inhibition of the deformation in the backlimb of the left-side anticline. These differences between the reference experiment and experiments with sedimentation, result in a different vergence of the obtained structures. In this sense, the reference experiment shows symmetric anticlines with no vergence of the structures, while the experiments with sedimentation, the left-side anticline clearly verges towards the left, and the right-side structure slightly verges towards the right (e.g. cross-section b-b' in fig. 5.2.6 B, C, and D).

jti 60-80 - The same deformation patterns, and differences, than in the previous time interval *jti 40-60* can be observed for the three experiments (fig. 5.2.7). Moreover, during this time interval, the sediment delta front progrades basinward and now the totally inhibition of the deformation in the backlimb of the left-side anticline can also be observed in the c-c' cross-section (fig. 5.2.7 B, C and D).

jti 80-100 - At the end of the simulation time, the analysis of the deformation for the three experiments shows the same pattern than in the previous time intervals (fig. 5.2.8).

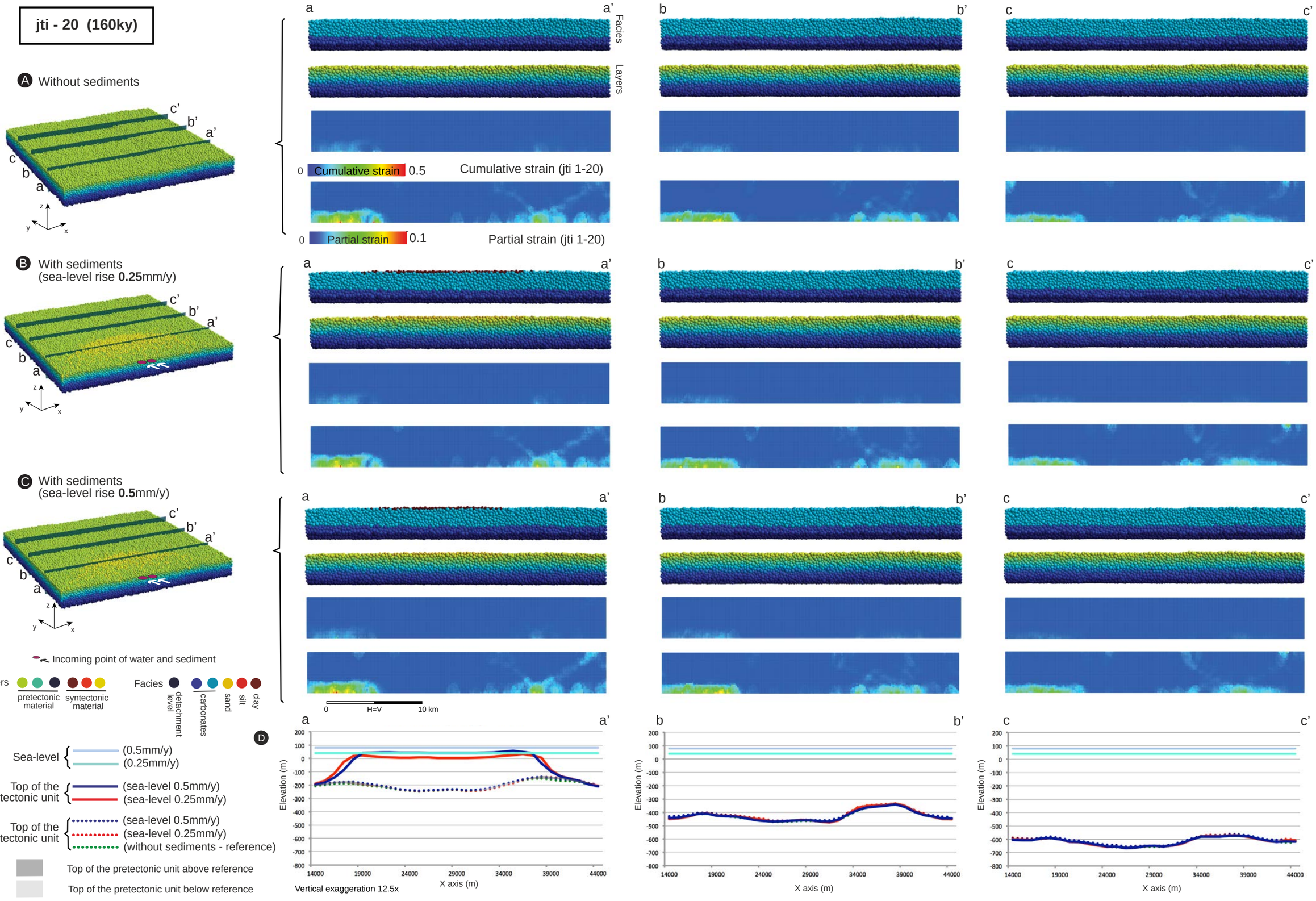

Figure 5.2.4- Results for the time step 20 (160ky). Cross-sections a-a', b-b' and c-c' for the three experiments: A- without sediments (reference experiment); B- with sediments and a sea-level rise rate of 0.25mm/y; C- with sediments and 0.5mm/y of sea-level rise rate. For each cross-section, DEM is represented coloured by layers, and by facies. The layers in the pretectonic unit do not represent any mechanical property, and they only have a visualization purpose. Yellow and reddish layers represent the syntectonic sediments added by SFM. The maximum strain for the pretectonic unit is also computed using the SSPX program. The maximum strain is calculated twice: taking into an account the entire period of deformation in order to visualize the structure (cumulative maximum strain); and for an interval time of 20 main time steps jti (160ky), in order to visualize the evolution of the deformation for a period time (partial maximum strain). Also a graphic for each cross-section has been added, with the position of the top of the pretectonic units and syntectonic units of the three examples is also added (D). In this time step few differences arise between the experiments. Deformation is mainly concentrated in the detachment level for the three experiments. See the text for a detailed explanation.

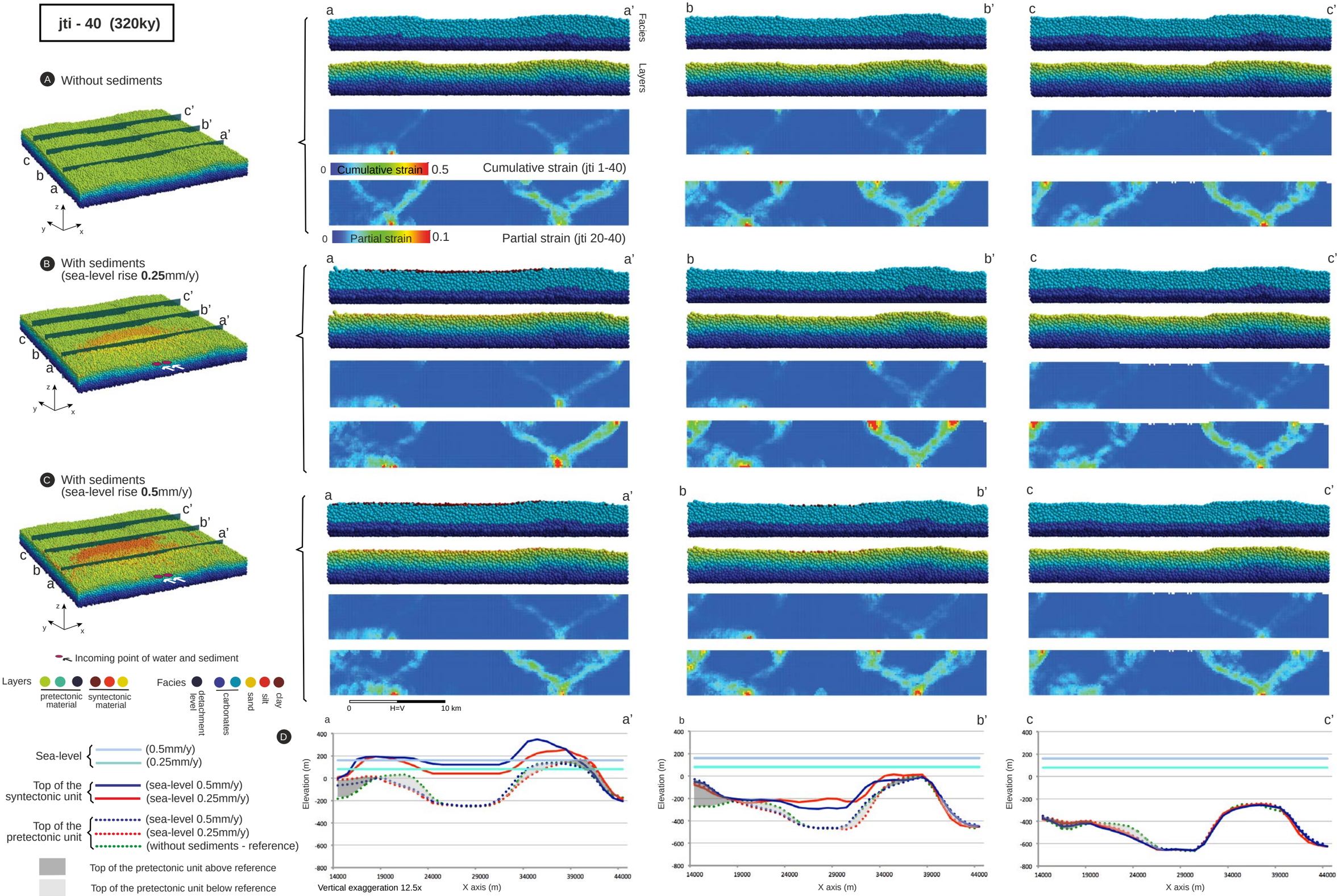

Figure 5.2.5- Re*sults for the time step 60 (320ky). Cross-sections a-a', b-b' and c-c' for the three experiments: A- without sediments (reference experiment); B- with sediments and a sea-level rise rate of 0.25mm/y; C. with sediments and 0.5mm/y of sea-level rise rate. For each cross-section, a graphic with the position of the top of the pre-tectonic and syn-tectonic units of the three examples has been added for their comparation (D). First differences between experiments start to be noticeable. Main difference arises in cross-section a-a' and b-b' where deformation in the backlimb of the left-side fold for both experiment with sedimentation is inhibited if compared with the experiment without sedimentation. This difference can be appreciated also in the surface of the pretectonic units, which suggest that the fold geometry is displaced towards the left for the experiments with sedimentation.*

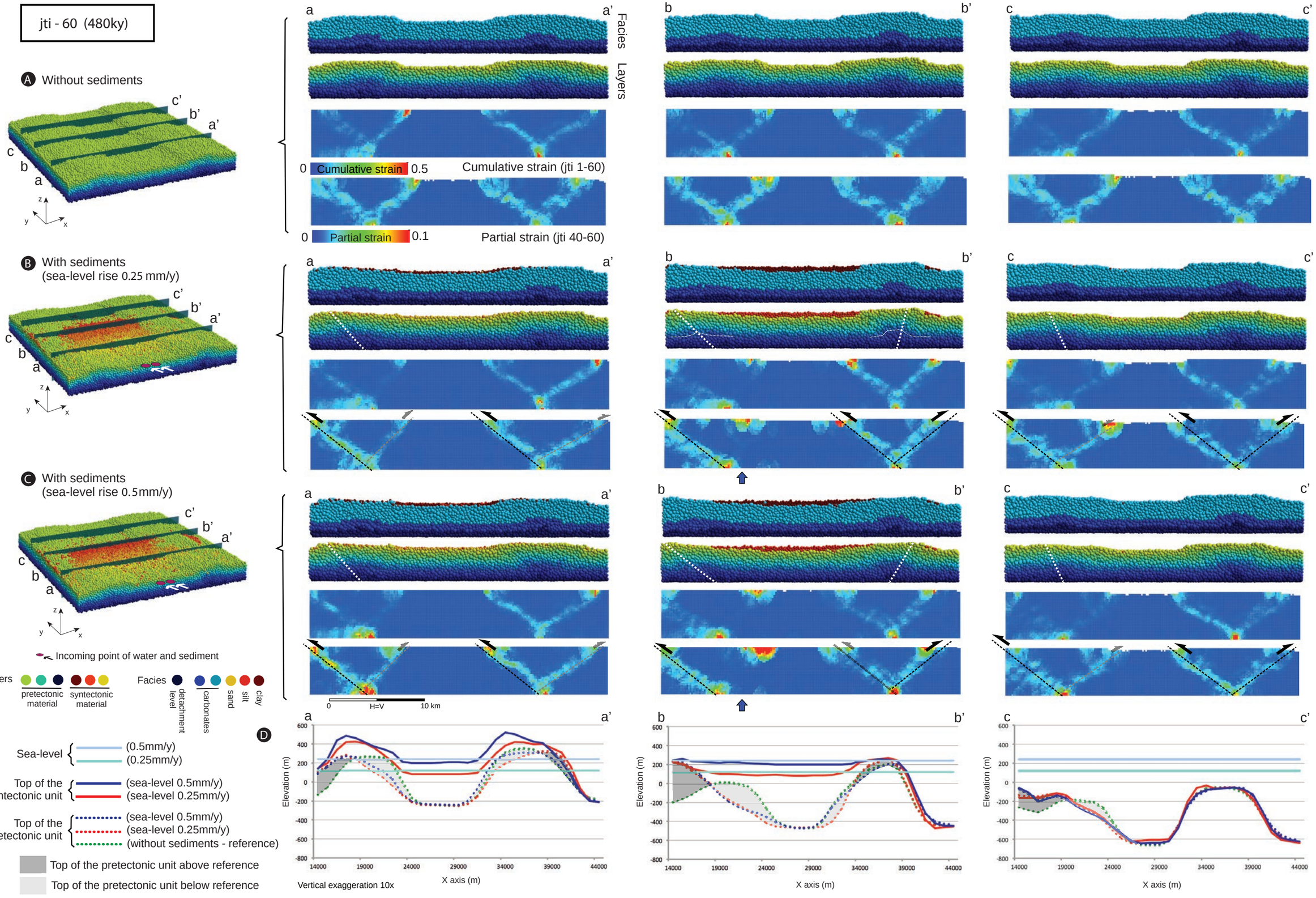

Figure 5.2.6- Results for the time step 60 (480ky). Cross-sections a-a', b-b' and c-c' for the three experiments: A- without sediments (reference experiment); B. with sediments and a sea-level rise rate of 0.25mm/y; C. with sediments and 0.5mm/y of sea-level rise rate. For each cross-section the DEM model and the maximum strain are represented. A graphic with the top of the pre-tectonic and syn-tectonic units for the experiments is also added for each cross-section (D). Note the difference between experiments considering sediments or not (reference model). These differences are larger in the b-b' cross-sections where deformation in the backlimb of the left-side anticline (blue arrow) is hindered and results in a fault-propagation fold rather than a detachment fold with a box-fold style. The dashed white line shows the vergence of the structures. See the text for a more detailed explanation.

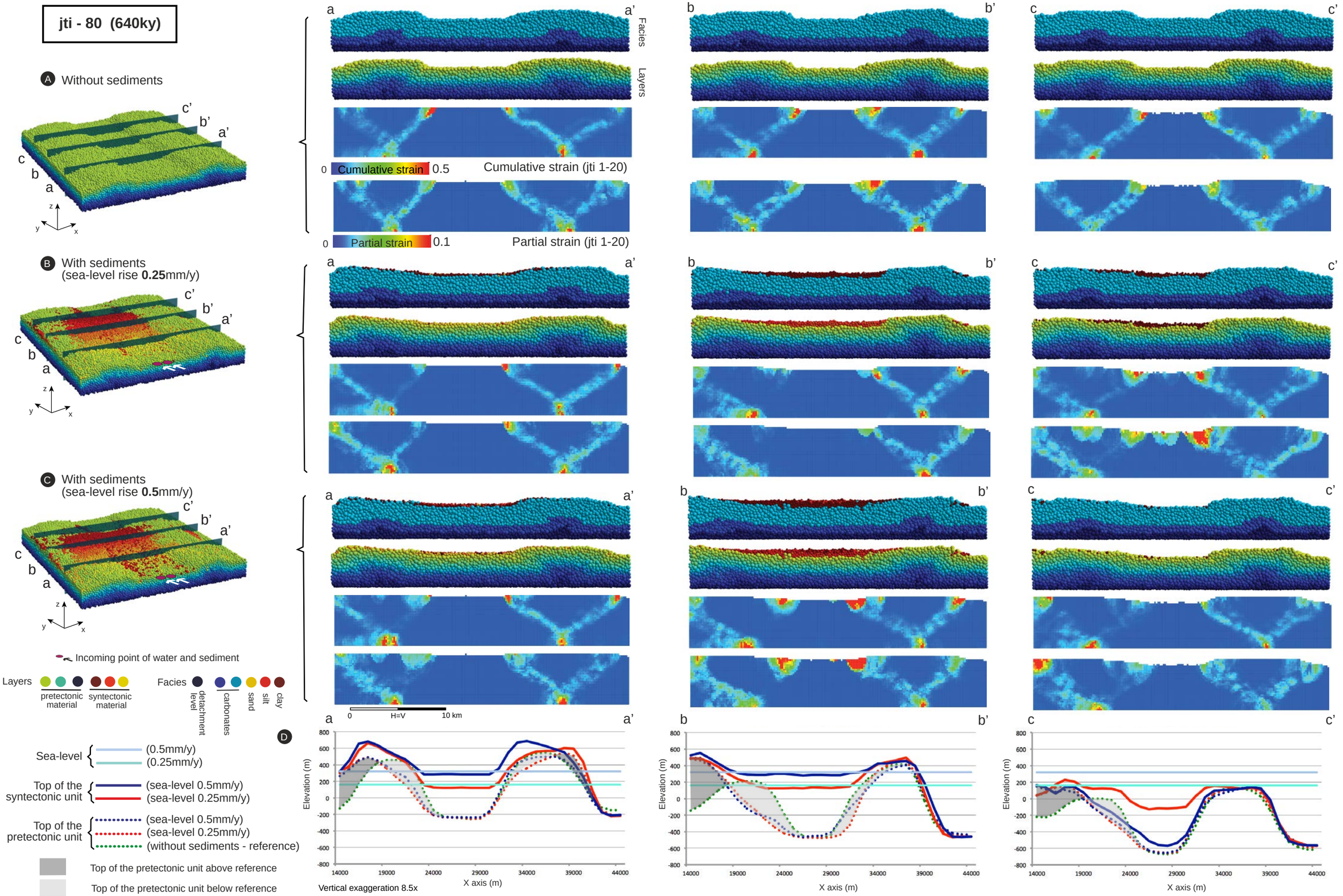

Figure 5.2.7- Results for the time step 80 (640ky). Cross-sections a-a', b-b' and c-c' for the three experiments: A- without sediments (reference experiment); B- with sediments and a sea-level rise rate of 0.25mm/y; C- with sediments and a sea-level rise rate of 0.5mm/y. The graphic, to compare the position of the top of the pre-tectonic and syn-tectonic units for the three experiments, is also added for the three cross-sections (D). In this time step, the same differences between experiments considering sediments (reference model) or not, are noticeable again: the deformation in the backlimb of the left-side anticline (blue arrow) is hindered and results in a fault-propagation fold rather than a detachment fold with a box-fold style. The dashed white line shows the vergence of the structures. See the text for a more detailed explanation.

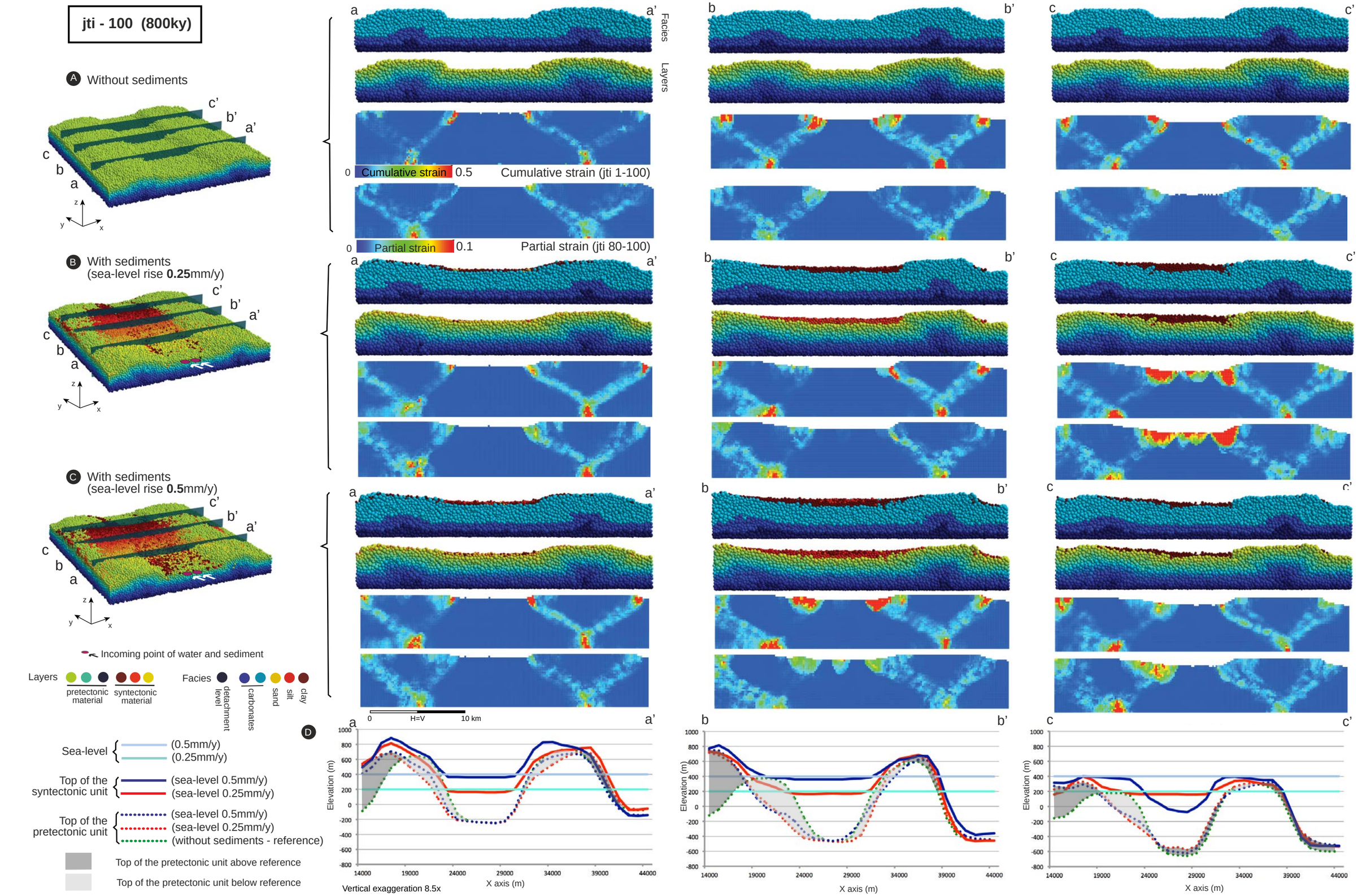

Figure 5.2.8- Results for the time step 100 (800ky). Cross-sections a-a', b-b' and c-c' for the three experiments: A. without sediments (reference experiment); B. with sediments and a sea-level rise rate of 0.25mm/y; C. with sediments and a sea-level rise rate of 0.5mm/y. The comparison between the top of the pre-tectonic and syn-tectonic units are also added in the lower part (D). The same deformation pattern than in the previous times steps is observable; therefore, also the same differences between experiments with sediments and without sediment are noticeable again. See the text for a more detailed explanation.

Therefore, the main differences between the experiments with and without sedimentation can also be observed. Thus, in the experiments considering sedimentation, the left-side structure evolves as a fault propagation fold rather than a detachment fold and it verges strongly to the left. On the other hand, the right-side structure is a detachment fold with asymmetric box-fold geometry, slightly vergent to the right. This relationship is more evident in the middle of the model (cross-section b-b') where it can also be observed the extent of the syncline, being wider than in the reference experiment. The synclinal has the widest transversal extension in the cross-section b-b' for experiment with a sea-level rise rate of 0.5mm/y.

The structural maps obtained for each experiment at the end of the simulation time (fig. 5.2.9A) show the above-mentioned differences in map view. In the reference experiment, the position of the hinge of both anticlines shows a linear trend perpendicular to the shortening direction. On the other hand, in the experiments with sedimentation, the position of the hinge of the left-side anticline shows a curved trend. The maximmum displacement of the hinge occurs in the middle of the model where also a maximum sediment spreading takes place. Progressively, the hinge position returns to its original position basinwards where there is no sedimentation.

The maps of the figure 5.2.9B highlight the main geometric difference between the experiments without and with sedimentation through a comparison of the position of the top of the pretectonic unit between of each experiment. Again, it can be observed that the bigger differences between experiments are located in the left-anticline, while the right-side anticline only shows lower differences in the forelimb.

The dip maps shown in the figure 5.2.9C also emphasize the differences between the structures developed in each experiment. In the experiments considering sedimentation, it could be observed how the syntectonic unit (superimposed black contour isopach map) strongly influences the dip of the limbs. This influence is mainly expressed in the backlimb of the left-side anticline where low dip angles are obtained in both experiments (due to the inhibition of the deformation, fig. 5.2.9 C2 and C3). For the experiment with sea-level rise rate of 0.25mm/y, the presence of the syntectonic sediment in the forelimb of the right-side anticline produces high dip angles basinwards, while lower dips are obtained in the proximal part. On the other hand, lower dips angles are obtained for the experiment with sea-level rise rate of 0.5mm/y, mainly in the middle of the model (fig. 5.2.9 C3).

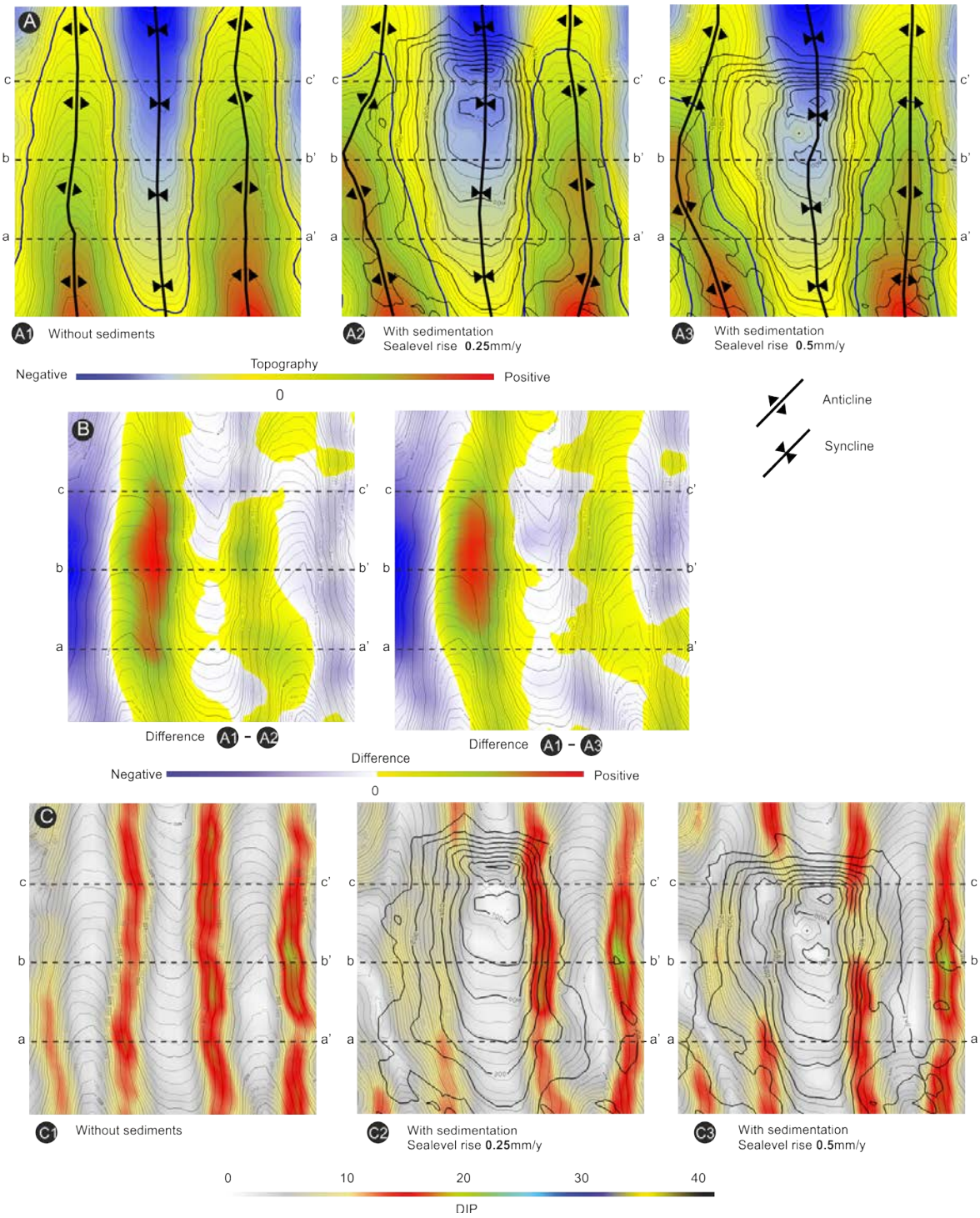

Figure 5.2.9. A. Map view for the top of the pre-tectonic unit for the three experiments analysed. An isopach map (contour lines) of the syn-tectonic unit has been superimposed to each map. B. Two maps showing the differences in the position of the top of the pre-tectonic unit between the reference experiment (without sedimentation) and the two other experiments considering sedimentation. The maps highlight the structural difference between the experiments without and with sedimentation. C. Dip map of the top of the pre-tectonic unit for the three experiments.

Regarding to the sedimentation pattern (fig. 5.2.10), the sedimentary infill of the related basin, placed between both anticlines, records a deltaic system with clinoforms prograding basinwards. This progradation is bigger in the experiment with a lower sea-level rise rate (fig. 5.2.10 A) than in the other experiment, where the aggradational component is higher (fig. 5.2.10 B) due to a higher increase accommodation space (fig. 5.2.11. The coarse sediment is mainly deposited in the proximal area and the deposited sediment type passes laterally basinward from coarse to medium-grained, and finally to finest-grained sediment. This last sediment type is mainly deposited in the distal part of the deltaic system. In the first time-steps, with the onset of the contractional structures, sediment can be settled on the entire basin without restrictions, but, as deformation progress, deltaic system is restricted to the syncline. Thus, the sediments that are finally located in the crestal area of the anticlines are deposited in the initial time-steps and they are subsequently exposed above the final sea-level position. The interplay between sediment input, sea-level rise rate and deformation produce a complex sedimentation pattern and depositional architecture.

Figure 5.2.11 shows the evolution of the top of the pretectonic and syntectonic units along the syncline (cross-section d-d') for the three experiments analysed. There are not large differences in the position of the upper limit of the pretectonic unit between the experiments, since this cross-section d-d' is sited in the syncline between the deformation areas. The evolution and height of the deltaic system for the two cases with sedimentation can be appreciated in this figure. Both deltaic systems prograde basinward. The aggradiatonal component is higher for the experiment with a sea-level rise rate of 0.5mm/y since the sea-level position creates more accommodation space than the experiment with a sea-level rise rate of 0.25mm/y. On the other hand, the deltaic system for the lower sea-level rise rate (0.25mm/y) experiment progrades quicker basinward due to the same reason.

The results obtained in the rest of the experiments are summarized in the appendix A, in order they can be checked or analysed (see discussion chapter).

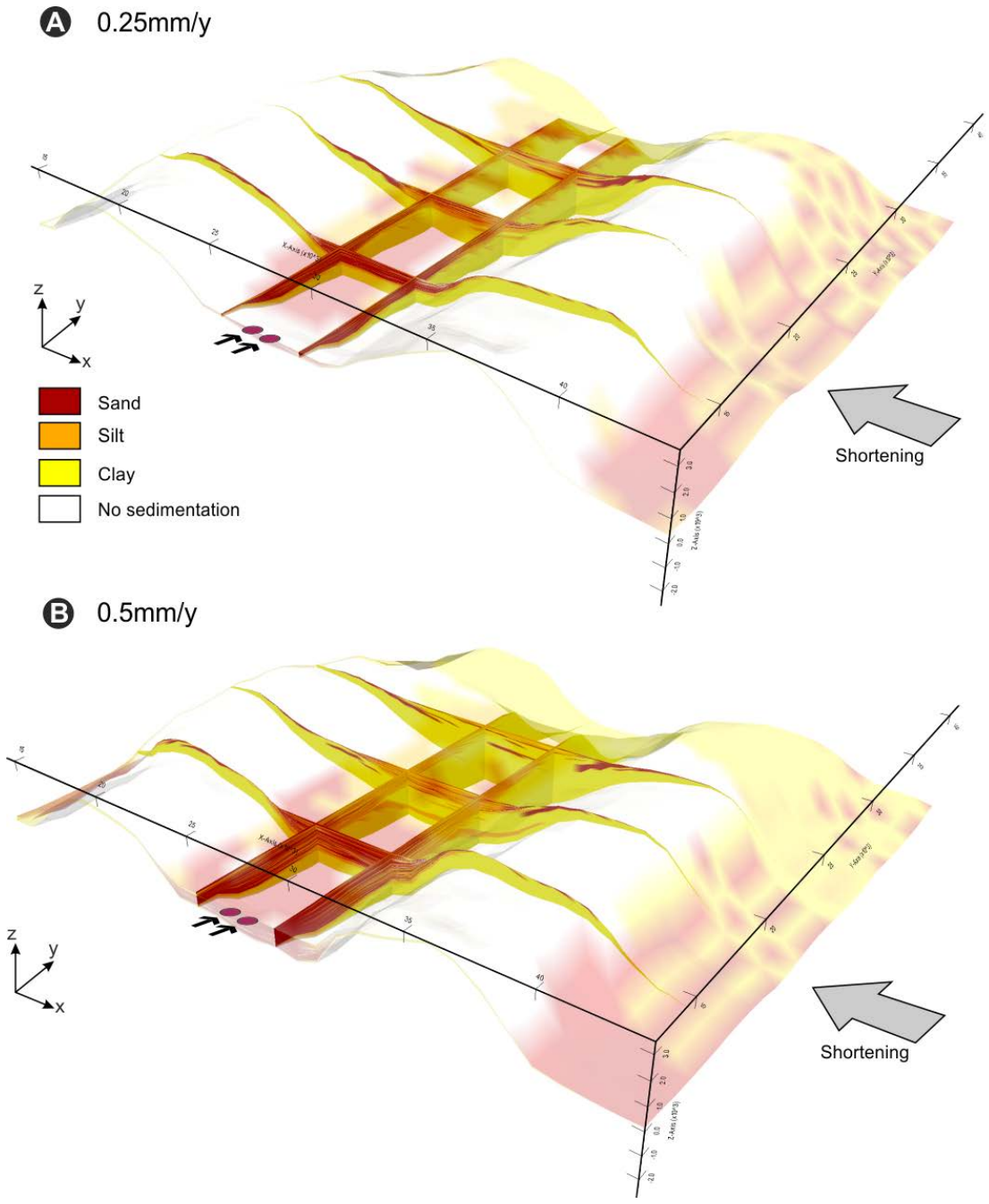

Figure 5.2.10 - Syntectonic sedimentary bodies obtained in the experiments with sedimentation, for the two sea-level rise rate considered: A- 0.25mm/y sea-level rise rate and B -0.5mm/y sea-level rise rate. The new sediments are coloured according the most representative sediments type in the area.

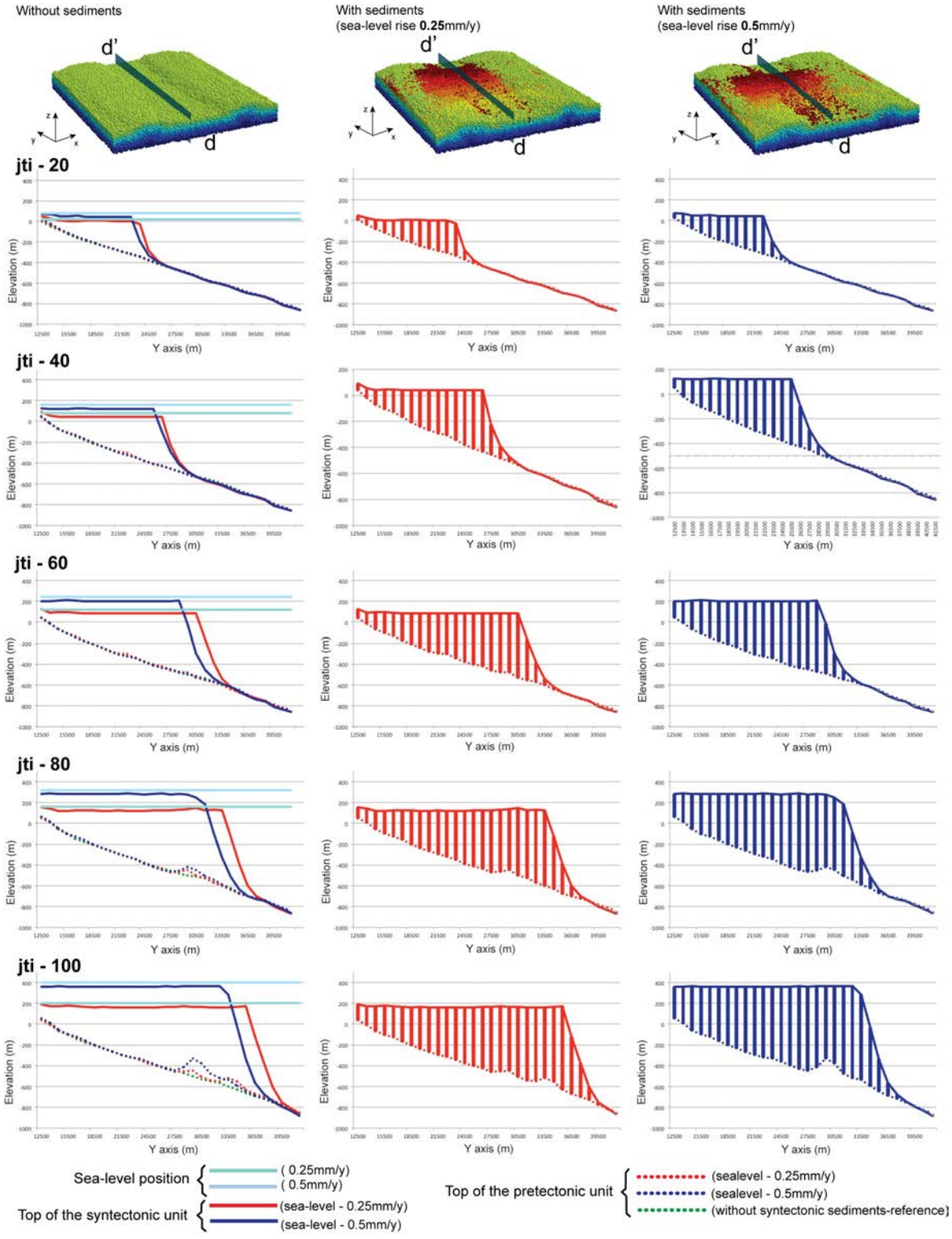

Figure 5.2.11 - Evolution of the top of the pre- and syn-tectonic unit for a longitudinal cross-section d-d' along the syncline for the three experiment analysed. The evolution is represented through five time steps: jti 20 (160ky), jti 40 (320ky), jti 60 (480ky), jti 80 (640ky) and jti 100 (800ky). The position of the transversal cross-sections, a-a', b-b' and c-c' are also included.

5.2.4 Discussion

The analysis of the results shows clear structural differences in the geometry of the anticlines between the reference experiment (without sediments) and the experiments considering syntectonic sedimentation. These differences suggest an influence of the syntectonic sedimentation over the final geometry of the fold, therefore also an influence in the mechanism of deformation of such structures.

In the reference experiment the deformation reproduces two detachment folds with a symmetric box fold shape over the basal discontinuities. This geometry is longitudinally constant along the fold axis (figs. 5.2.4 A, 5.2.5 A, 5.2.6 A, 5.2.7 A, 5.2.8 A). The analysis of the deformation shows the typical conjugates shear zones for this type of the structure.

Considering syntectonic sedimentation and a sea-level rise rate of 0.25mm/y, it can be appreciated how the left-side anticline changes its geometry, being now asymmetric with a vergence towards the left. This change suggests that the deposition of the new sediments is conditioning clearly the final geometry of the left-side anticline. Moreover, the internal structure and analysis of the strain show a clear shear band on the forelimb, while in the backlimb this shear band is less clear or nonexitent (cross-section b-b'). Thus, this anticline evolves basinward from a detachment fold to a fault propagation fold, and returns to a detachment fold in the distal areas. The cross-section where the geometry of fold has a major asymmetry, is the same cross-sections with the maximum amount of new sediment deposited (cross-section b-b' in fig. 5.2.4B, 5.2.5B, 5.2.6B, 5.2.7B, 5.2.8 B and fig 5.2.10). The last strengthen the suggestion that the syntectonic sedimentation is changing the final fold geometry.

In the experiment with syn-tectonic sedimentation and sea-level rise rate of 0,5 mm/y, the same effect of the new sediments over the geometry of the left-side anticline, in the b-b' cross-section, can be appreciated again. Moreover, the effect of the sedimentation over the left-side fold geometry can also be appreciated in the proximal area (cross-section a-a' fig. 5.2.4C, 5.2.5C, 5.2.6C, 5.2.7C, 5.2.8C). This is as a consequence of the increase of the accommodation space, which allows subaquatic conditions in these areas for a longer time interval. The effect of sedimentation over the fold geometry decreases basinward in distal parts of the basin (cross-section c-c'), where no sedimentation occurs or the sediment settles at the end of the simulation time. Regarding to the geometry of right-side anticline in this experiment, a slightly vergence towards the right can also be appreciated, mainly in the middle of the model (cross-section b-b') in line with the maximum sediment deposit thickness.

The wider amplitude of the syncline is obtained for the experiment with a rate of the sea-level rise of 0.5mm/y, which is the experiment with larger vergence of the left-side anticline towards the left, and the perceptible vergence of the right-side anticline towards the right. It is worth to note that the syncline is narrower in the proximal area, where less amount of sediment can settle, and its amplitude widen basinward as bathymetry increases. Thus, the amount of settled sediment also increases basinward. Therefore, and as a consequence of the effect of the sedimentation on the fold geometry and its vergence, the syntectonic sediment also has an indirect influence over (i) the basin geometry, (ii) the amplitude of the syncline and (iii) the dimension of the sedimentary deltaic system itself.

As it can be observed, the right-side anticline starts to develop before the left-side anticline for all the three experiments analysed. Although geologically consistent, this could be an unexpected behaviour since the discontinuity of the velocities over each breaking point has the same value and mathematical definition. This early uplift of the right-side anticline can be as a result of a mix between the boundary wall position, which is forcing the early development of the fold, and the shortening direction (from the right to left), which could favour the development of the right anticline first.

This earlier develop of the right-side anticline may be one reason (1) to explain why syntectonic sediment has a larger effect on the geometry and structure of left-side anticline than in the geometry of the right-side anticline. Since the left-side anticline structure evolves later, the sediment can be initially distributed from the syncline towards the left-side area. Meanwhile, the sediment cannot settle towards the right-side area, where the right-side anticline confines the sedimentation towards the synclinal since early time steps. Therefore the sediments are more likely to be effecting the left-side anticline than the right one, since their presence is bigger in this area.

Another reason (2) could be the position of the sediment deposition in relation to the anticline geometry and the shortening direction (from the right to left). Thus, when sediment is deposited over the backlimb of the left-side anticline, the hinge of the anticline can migrate towards the left, while in the right-side anticline the sediments settles in the forelimb of a structure with a relative more structural relief.

When comparing the results of the rest of the experiments (see Appendix A), between the cases with and without sedimentation (reference experiment) and with the same deformation rate, it can be inferred the same behaviour in the effect of the sedimentation on deformation style of the folds. Nonetheless, and in order to verify the real effect of sedimentation on the fold geometry and also to ensure that the shortening

direction is not determinative, the experiment with the right-side anticline inhibited for the first time-steps is briefly analysed. When considering sedimentation, these experiments shows a clear right-vergence fold, while the left-side anticle shows a slightly box-fold shape. In these experiments the left-side anticline starts to develop earlier than the right-side anticline, which uplift is inhibited during the first time steps. Therefore, the sediments are allowed to settle in this right-side area before the deformation starts. In this experiments the sediment has the opposite effect on the final structures: the right-side shows a strong asymmetry with a vergence towards the right (cross section b-b'), while the left-side anticline is less affected by the sediments.

Comparison with a real example

This set of experiments is consistent with the main goal of this study and interesting conclusions has been obtained about the effect of syn-tectonic sedimentation on fold-geometry (see next section). However, in order to be compared with real examples, other parameters and more complex experiments needs to be added. Nonetheless, a first comparison can be done in order to obtain first insights from the numerical modelling.

Under this premise, and considering the experiment setup used in the previous section, the results of these experiments can be used as an approximation to be compared with the Sobrarbe fold system. The Sobrarbe fold system is sited in the Ainsa Basin, South-central Pyrenees. In general, the Sobrarbe fold system consists of two major N-S anticlines, which, from East to West, are named Mediano and Boltaña (fig 2.5.12). Between both anticlines, it is placed the Buil syncline, as well as, other minor structures (the Olsón and the Añisclo anticlines). The attention will be centred in the Buil syncline, and the two anticline that fringe this structure in E-W direction: the Mediano (East or right-side in model coordinates) and Boltaña anticline (West or left-side anticline in model coordinates).

Following the description of Muñoz et al. (2013), the Mediano anticline is defined as a detachment fold. The Boltaña anticline is the most prominent anticline in the Sobrarbe system and it is related to the propagation of the westward verging Boltaña blind thrust. The structural differences between these two folds are mainly attributed to the difference in the thickness of the Triassic detachment level.

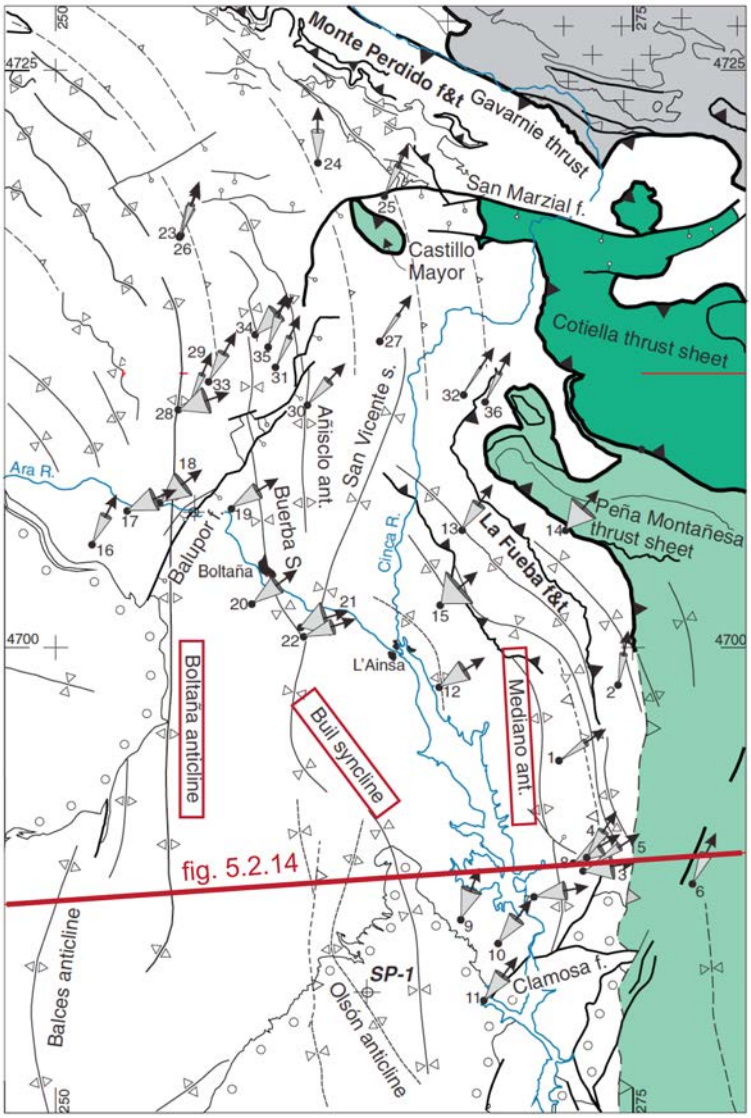

Figure 5.2.12 - Structural map of the Ainsa Zone sited in the central Pyrenees. It can be seen the placing of the four main structures of the Sobrabe fold system, Mediano, Olson, Añisclo and Boltaña anticlines as well as the Buil syncline.

Poblet et al. (1998) presents a kinematic evolution of the Mediano anticline using forward modelling (fig 5.2.13 A), which has similar uplift and sedimentation rates that the ones proposed in the previous numerical experiments (uplift rate for Mediano 0.7mm/y). Poblet considers that the fold growth occurs by limb rotation and hinge migration, according to the data obtained from reverse modelling of decompacted growth strata. In this study the syntectonic sediments have a passive role, and they are used to study the kinematic deformation of the fold structure. Even the initial situation is not the same, (Mediano anticline has already started to develop when considering the synteconic sedimentation) the evolution and the final structure show a vergence of the Mediano anticline towards the East. This geometry is also obtained in the right-side anticline of the experiment with a sea-level rise rate of 0.5mm/y (see the close view of the evolution of the right-side anticline in the figure 5.2.13 B). The geometry of both anticlines is very similar with a vergence to the opposite direction than the shortening direction (from east to west for Mediano setting, and form right to left for the experiment presented here).

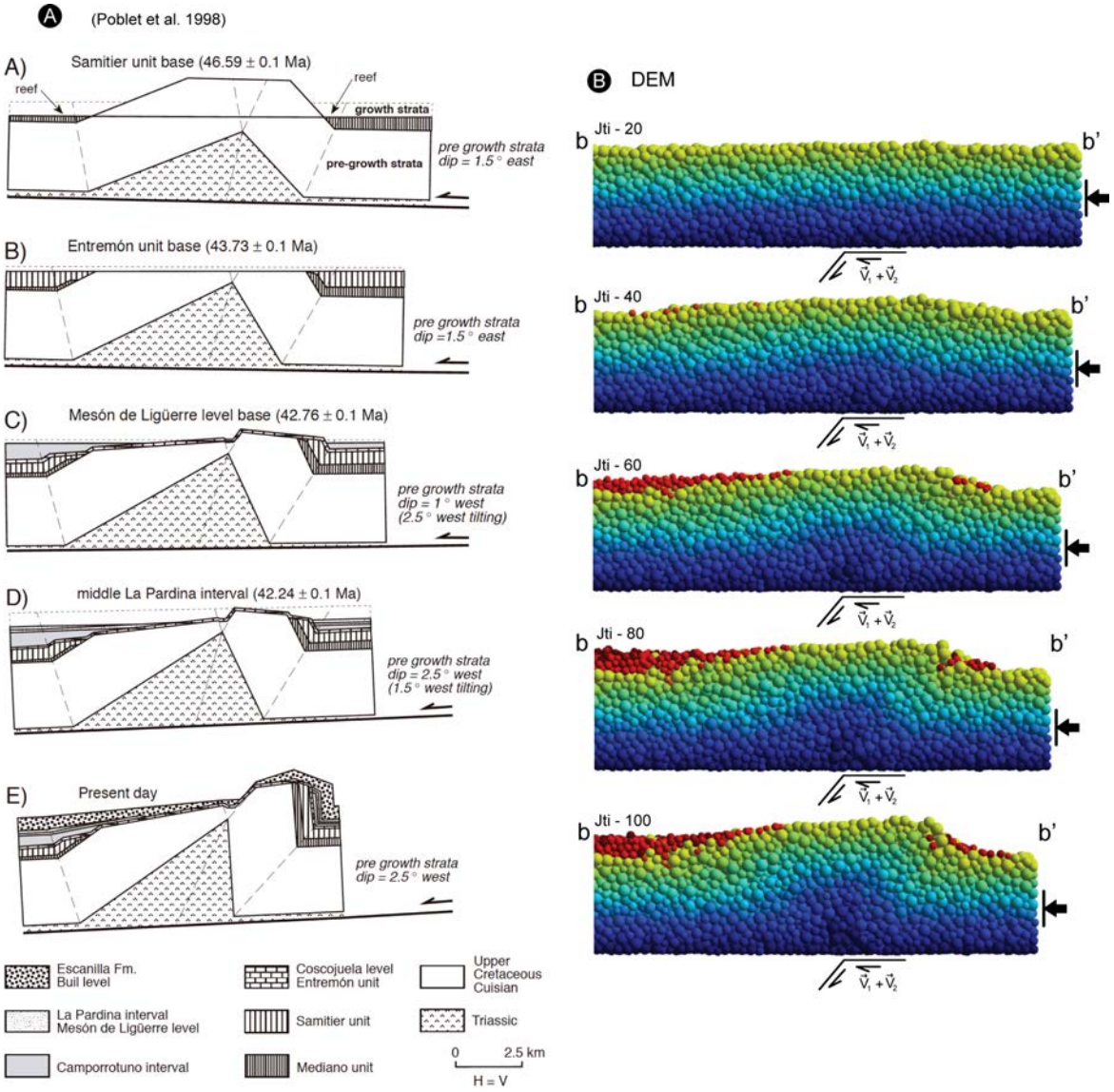

Figure 5.2.13 A- Evolutionary model (kinematic reconstruction using forward modelling) of the Mediano anticline. The upper continental sediment is not represented (Poblet et al. 1998). B. Close view of the evolution of right-side syncline through five time steps (DEM), considering the sea-level rise rate of 0.5mm/y, coloured by layers (no mechanical properties) for a better visualization of the deformation.

To understand the kinematics of the Ainsa fold system (fig 5.2.12), Muñoz et al. (2013) performs a study integrating sedimentological, structural and paleomagnetic data. In this study, growth strata are mainly studied to characterize the uplift of the structures and, together with the paleomagnetic data, to determine the timing and kinematics of such deformations.

Nonetheless, in this type of studies the effect of sedimentation in the final structure is underestimated, and the growth strata have a passive role in the characterization of this final structure (as in Poblet et al. 1998).

Obviously, this real geological setting is more complex than the experiments presented here; and, as concluded by Muñoz et al. 2013, its kinematics involves along strike diferential shortening and rotational events. Also the timing of deformation and sedimentation differs from the timing of deformation and sedimentation in the numerical experiments: Mediano anticline start to develop before than the considered syntectonic sediment deposition (Poblet et al 1998) and it also starts to develop before than Boltaña anticline. Nonetheless, part of the evolution of these structures, Mediano and Boltaña, coincide in time, with similar deformation and sedimentation rates that the ones used in the numerical simulations (Poblet et al. 1998).

If we focus in the Sobrabe fold system (fig 5.2.14 B), and specifically in the cross-section formed by the structures of Mediano, Buil, and Boltaña (figure 5.2.14 B1, modified from Muñoz et al. 2013) we can appreciate huge similarities with the numerical experiments presented here and specifically with the cross-section b-b' for a sea-level rise rate of 0.5mmy.

The left-side anticline of the experiment (fig 5.2.14 A) shows a fault propagation fold, similar to the Boltaña anticline structure, which also shows the same internal deformation mechanism. The right-side anticline of the experiment (fig 2.5.14 A) shows an asymmetric right-vergent detachment fold, similar to Mediano anticline.

According to the interpretation of the numerical model, and translating them to the real geological setting, the Boltaña anticline starts to develop later on, so it would be more susceptible to be affected by the sedimentation of the syntectonic units than Mediano. Boltaña is also the one that shows a high vergence towards the left, and a clear mechanism of formation related to a fault propagation fold.

This comparison, or reflexion, does not pretend to give any affirmation about the possible effect that the syntectonic sediments can have in the development and the final structure of Mediano and Boltaña. As commented before, the differences in the thickness of the detachment level is thought to be the main mechanism for such structural differences between Mediano and Boltaña. Moreover, other factors can be involved in the formation of Sobrarbe fold system and can get a strong influence in the final geometry of Mediano and Boltaña. Nonetheless, it is remarkable the similitude of the final geological structures of the Mediano and Boltaña and the numerical experiments presented here, which are achieved by a relative simple setup with a tilted layer-cake model and a simple deformation setting. Since the numerical experiments are clearly suggesting that syntectonic sediments can also play an important role in the final geometry and in the kinematics of such

structures, it is worth to consider its possible effect when reconstructing and interpreting such structures in real geological settings like the Sobrarbe fold system. Therefore, the experiments performed gives new tools and insights that can be included in order to to decipher the evolution of such structures.

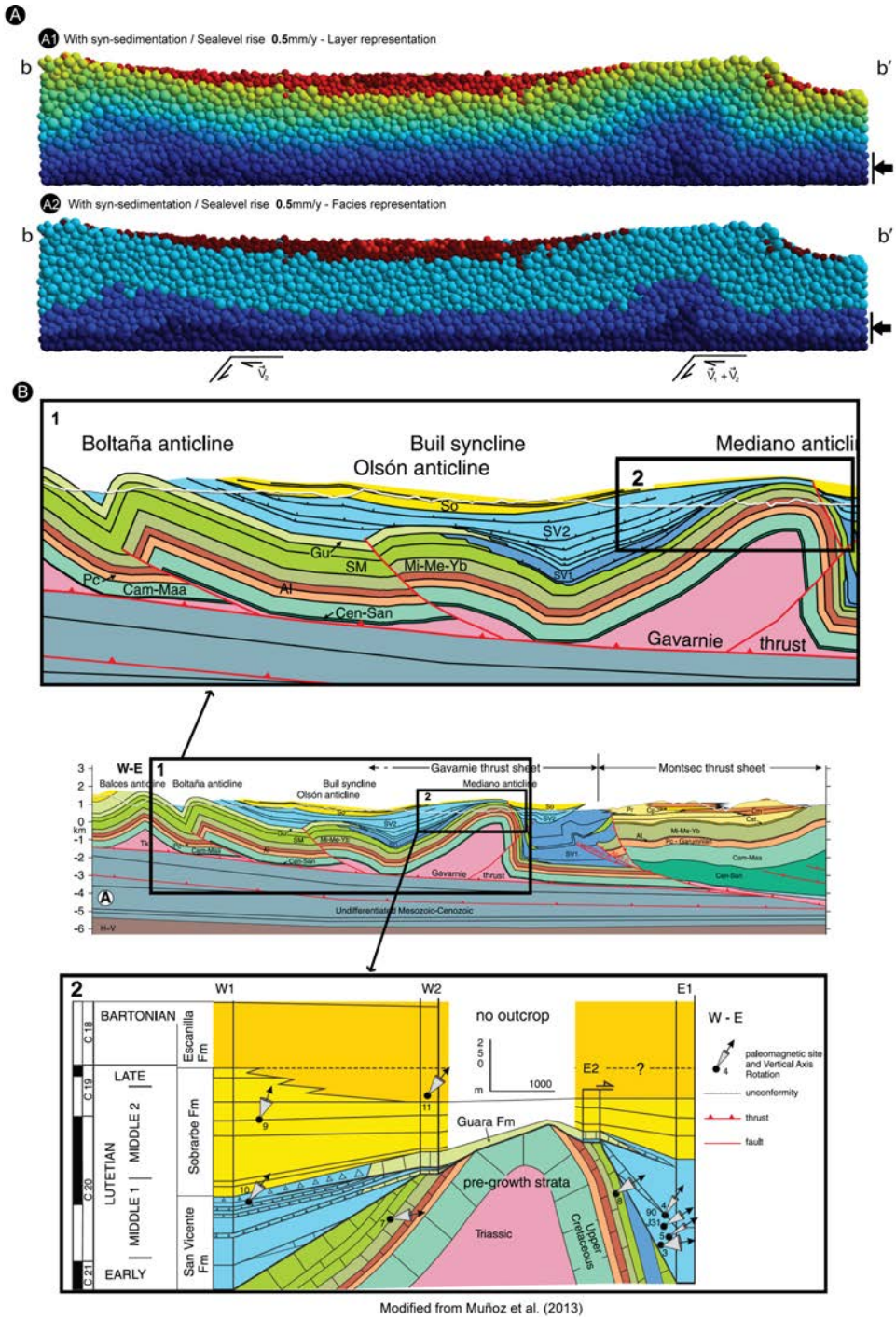

Modified from Muñoz et al. (2013)

Figure 5.2.14 A- Modified from Muñoz et al. 2013. Cross-section of the Southern part of the Ainsa Oblique Zone (see location in Fig. 5.2.12). (1) Enlargement of the three of the main structures of the Sobrarbe fold system: the Mediano anticline in the East (right-side), the Boltaña anticline to the North (left-side) and the Olson anticline (with no topographical expression). (2) Enlargement of the Mediano anticline (base of the Escanilla FM. restored to horizontal) where the synfolding growth sequence can be appreciate in detail.

CHAPTER 6

DISCUSSION, CONCLUSIONS AND FUTURE WORK

6.1 DISCUSSION

The work involved in this thesis can be divided in two main different tasks: (1) the development of a numerical model itself, and (2) its application through two case studies. Nonetheless, both tasks are clearly involved in a main aim, which is the numerical modelling of geological processes, aiming to widen the understanding between the interaction of deformation and sedimentary processes in a subaquatic environment, as well as to give new insights in both cases studies proposed.

The skills for carrying out each part are different: first part requires mainly of mathematical, numerical and programing skills to solve a geological problem, while for the second part (the application part) is needed mainly a geological knowledge, specifically when defining the case study and interpreting the results. The different kind of the work involved in each part, leads in that each part has got already its own proper discussions. The approach taken in the development of the new model is already discussed in the chapter 3 (section 3.1.2) as well as the limitations encountered (section 3.2.6). On the other hand, each case study has its own discussion of the results, since each case study takes place in different tectonic setting: extensional (section 5.1.4) and contractional (5.2.4).

Even the difference of the geological setting between both cases studies, the main purposes of the performed numerical modelling are similar for both: 1) the understanding of the main processes that control the sedimentary record 2) the understanding of the mechanical processes that control the structural setting as well as the deformation pattern; and 3) providing new ideas for the interpretation of sedimentary basins based either on surface field data or subsurface data. The experiments results of both case studies may provide new concepts to improve the interpretation of the sedimentary basins and develop new predictive models.

In the first case study, *the effect of normal faulting and a relay ramp on sediment dispersal*, the results can help to improve the interpretation in subaqueous overfilled rift basins. Some of the results, such as the role of the strain rate on the internal architecture of syn-rift sequences, can be applied in a wide variety of rift basins.

For the second case study, *the effect of syntectonic sedimentation in fold geometry*, the results suggest that the syntectonic sediments can have a strong influence in the final geometry of

the fold as well as on its deformation mechanism. The implications of these results can also be used when analysing other different contractional scenarios.

It is worth to note that each case study makes emphasis in different abilities of the new merged model, the first case study make emphasis in the analysis of the sedimentary patterns, while the second case study is more focussed in the analysis of the deformation. Nonetheless, any of these analysis, sedimentological or structural, can be performed in any case study if necessary. These different analyses in the case studies show the versatility of the model, and its range of possible applications.

Obviously, the reality is too complex and the different geological processes are controlled by numerous geological parameters with complex relationships. The main aim of the numerical model is not to reproduce exactly the geological reality, but to help to understand the different geological processes in order to be predictive. Numerical models allow to simplify and to study the relationship between each parameter, and to provide valuable information about the sensitivity of each parameter on the geological process under study. In order to do that, the best approach is to start with simple experiments, with only few geological variable parameters, and then progressively add new variables or changing parameters in order to gradually increase the understanding of the geological complexity.

This approach is applied in each case study:

- In the experiments performed to study the effect of a relay ramp on sediment dispersal, the initial configuration was designed with one simple fault configuration in two different positions, proximal and distal. The patterns of sedimentation obtained for both simple configurations are analysed for different slip rates of the fault. The results obtained with these simple configurations are compared with the results obtained for the configuration with two overlapped faults (located in the same position used for the two initial simple experiments) linked by a relay ramp. The control of each parameter: fault configuration, deformation rate and source area position, over all the sedimentary patterns, allows us to determine, how the configuration with two overlapped normal faults and a relay ramp is affecting the sediment dispersal into the basin.

- In the set of experiments performed to study the effect of syntectonic sedimentation on the fold geometry, the simplest experiment is defined with deformation but without sediments in order to be used as a *reference model*. This first experiment allows us to analyse the evolution of the structures and their

deformation and final geometry without the interaction of any other process. Therefore, when adding new syntectonic sediments and applying the same deformation conditions, any variations in the kinematic and final geometry of the fold structure can be considered as a result of the interaction of the syntectonic sedimentation with the deformation of the pretectonic unit. If the main objective of this second case study would have been to study the evolution of the syntectonic unit in a contractional setting, the design of the experiments set would have been initially different. The first experiment would be defined without deformation, in order to study the evolution of the deltaic system in a non-contractional setting. Gradually, deformation would have been added to the initial configuration defining different shortening rates (or uplift rates) in order to determine which is the influence of the deformation in the final geometry of the sedimentary bodies and the depositional architecture.

The results and its analysis for each case study, highlight the applicability of the developed model that can be applied to a wide range of geological scenarios. Specifically, the last case study strength the model to the maximum of its limitation: a large model size, with a large number of DE, and necessarily, also considerable large size of the radii of these spheres. Moreover the deformation model also has a large shortening in the *x* axis direction. Nonetheless, the number of transfers of sediments between SFM and DEM are frequent enough to minimize the error in the final location of the sediment. This error is produced as a consequence of the relative horinzontal displacements between the FEM mesh and the DEM surface (see 'limitations of the model' in section 3.2.6). Thus, the results of the model offer a plausible analysis.

Last but not least, these case studies also remark the importance of consider a 3D model when analysing the interactions between deformation and sedimentation. In the first case study the sedimentation pattern has differences in transversal and longitudinal direction. For the second case study, the effect of the syntectonic sedimentation on fold geometry is not constant along the fold axis, and it depend on the distance to the source area, and the available accommodation space together with the deformation stage in which the sediment settle over the different parts of the structure.

6.2 CONCLUSIONS

This thesis provides a comprehensive overview of the work carried out to combine two previous models, SFM (sedimentation) and DEM (tectonics), into one single model. This new model allows us to simulate simultaneously tectonic and sedimentary processes,

and thus, to simulate their interactions. The code of the model is implemented using the previous versions of SFM and DEM, as starting codes.

The feature and novelty of this new code lie in two main facts: On the one hand, the new model combines processes of deformation of the upper crust and subaquatic processes of transport and sedimentation in a single setting; on the other hand, the model merges two completely different numerical methods, the **discrete element** technique, which manages the deformation in the sedimentary cover due to tectonic movement, and the **finite element** method that solves the equations related to sedimentary processes in the overlying water column. The model combines the two previous models by allowing them to run separately, exchanging the necessary information at each time step: DEM provides SFM with the new position of the topographic surface due to tectonic movements, while SFM supplies new syntectonic materials to DEM. These links between both models allow us to establish an interesting feedback between both processes. New stratigraphic architectures, and new deformation evolution can be obtained as a consequence of interaction of these two processes.

In order to test the performance of the developed combined code, the code has been applied to model two simple test experiments. Moreover, the code has been used to study two more complex cases studies: (1) the syntectonic sedimentation in an extensional fault system and the related relay ramp; and (2) the effect of syntectonic sedimentation on fold geometry. The following sections summarize the main conclusions derivate from these applications of the code.

6.2.1 Conclusions drawn from the simple test experiments.

The two test experiments, models the sedimentation associated with the growth of a normal fault and a reverse fault, respectively. Each experiment has been defined with a different set of initial and boundary conditions for fluid flow, transport and sedimentation, as well as different tectonic boundary conditions and displacement rates.

Results obtained by both experiments show realistic syntectonic stratigraphic architectures. The evolution of the basin topography in the two examples is the result of both tectonic movements and sedimentation. Fluid flow and, consequently, transport and sedimentation, change according to this evolving topography. The depositional sedimentary bodies are similar to reported natural examples in each case. The transfer of sediments from SFM to DEM allows us to have more realistic deformed sedimentary bodies as a result of the tectonic movements occurring in a basin. It is also noted that the

propagation of the deformation is affected by the addition of syntectonic sediments into the model.

6.2.2 The effect of normal faulting and relay ramp on sediment dispersal. Conclusions.

The syntectonic sedimentary model presented in this thesis has proven to be a promising tool with which to analyse the effect of two overlapped normal faults and the related relay ramp on sediment dispersal. In this sense, different experiments have been performed varying three main parameters: fault displacement rates; fault configuration; and source area location.

Regarding the fault displacement rates, the final dominant sediment type distributions show clear differences as function of the deformation velocity and the related accommodation space. The distribution trend is wider at lower displacement rates (2 cm/y), due to less accommodation space and a higher transport distance of the different terrigenous sediment types (because of higher fluid flow velocities). The most complete and detailed stratigraphic record is obtained defining a deformation velocity of 10 cm/y.

Concerning the fault configuration, both experiments with a normal fault in a proximal or distal position (and defining a regional source boundary or RSBE) show no clear differences in the dominant sediment type trend and distribution. The same dominant sediment type arrangement can be observed, which is controlled by the fault position. Differences in grain-size distribution are found in transversal direction, i.e. perpendicular to the normal faults. In the third experiment comprising two overlapping normal faults linked by a relay ramp and using a regional source, the sedimentation pattern of the syntectonic package is not found to be the combination of the previous experiments, and no oblique transition from fault to fault is obtained. In contrast, the stepped left fault experiment also shows a dominant sediment type trend linear and parallel to the normal faults (or very slightly left stepped for the coarse- to medium-grained transition) without reflecting the real geometry of the faults and the relay ramp. Only the transition between the footwall and the hangingwall shows the left stepped fault geometry. Although dominant grain-size trends do not reflect the fault configuration, sediment accumulation for the coarse and medium-grained sediments shows not only differences perpendicular to faults, but also differences parallel to faults as a result of the left stepped fault geometry and the relay ramp position. In this sense, an asymmetric sediment distribution, parallel to fault strike, is obtained, being higher in the proximal normal fault than in the distal normal fault.

With regard to the results obtained by changing the source area location (to a punctual source area or PSEs), it is concluded that the nonlinear dominant sediment map trends and the grain-size distribution in the hangingwall and the relay ramp, are mainly conditioned by the source area location, *not* the fault geometry. This is especially pronounced when source points are defined parallel to the fault strike (left and right PSE). In these cases, the relationship between the relay ramp dip and the transport direction strongly influences the grain-size arrangement, and an opposite distribution can be obtained. In this sense, when the transport direction is opposed to the relay ramp dip, a complex stratigraphic architecture is obtained. Interpreting the grain-size distribution, a correct right source area location must be deduced. Nevertheless, in cases with little (or poor) lithological information (for example in seismic profiles), erroneous or complex conclusions could be extracted using only the geometrical relationships of the reflectors terminations.

In general, even though the sedimentary infill of these experiments shows differences in grain-size sediment accumulation, the same stratigraphic architecture is obtained in the PSEs. The sedimentary bodies shows a mainly progradation bottom trend (with higher delta front slopes) infilling the initial accommodation space. The upper stratigraphic units are more aggradational (and progradational), since they are mainly controlled by the subsidence. Therefore more tabular beds characterize these upper units, with lower delta front slopes in perpendicular to fault direction.

Regarding the pretectonic sediment deformation, model results show a triangle deformation zone with a layer thickening and thinning that are in agreement with a trishear kinematic model related to a fault propagation fold. Deformation is also present in the hangingwall and causes slightly retrogradation/progradation/aggradation trends in the sedimentary trend.

6.2.3 The effect of syntectonic sedimentation in fold geometry. Conclusions.

The numerical model developed during this thesis has been also applied to study the effect of syntectonic sedimentation on fold geometry. Thus, a contractional system that reproduces the development of two anticlines has been designed for the DEM. The initial and boundary condition for the sedimentary model (SFM) aims to reproduce the evolution of a deltaic system located in the syncline between both structures.

From the numerical results, can be concluded that the syntectonic sedimentation is controlling the fold style and geometry. Nonetheless, the effect of syntectonic sedimentation over the fold geometry is larger in the left-side anticline (sediment settles in the backlimb of

the anticline) than in the right-side anticline (sediment settles in the forelimb of the anticline). Comparing the experiments with and without syntectonic sediments, the geometry of the left-side anticline changes from a box-fold geometry to an asymmetric fold with a clear vergence towards the left; the internal deformation suggests that the fold evolves from a detachment fold to a fault propagation fold. The right-side anticline only shows a slightly vergence towards the right considering the highest sea-level rise rate with a higher accommodation space. Therefore, the effect of syntectonic sedimentation on the fold geometry could be related to: (i) the location of the sediments in relation to the fold structure; (ii) the time relation between the structure uplift and the sedimentation (that is controlled by the sea-level rise), and (iii) the shortening direction.

As a consequence of the fold geometry changes, the inner syncline and the related sedimentary basin are also changing in transversal and longitudinal direction, being wider when sedimentation is considered and a highest sea-level rise rate is defined. As a consequence, the deltaic system is also controlled by these parameters.

The effect of syntectonic sedimentation in fold style and geometry is not constant longitudinally along the anticline axis, and it can also be related to the accommodation space and the distance to the source area. In proximal areas, with an initial lower bathymetry, and therefore less sediments settled, the effect of the syntectonic sedimentation over the fold geometry is less noticeable. Basinward, the effect of the syntectonic sedimentation increases with the sediment thickness. This effect decreases in the distal areas, where no sedimentation occurs or the sediments settle in late stages of the deformation.

The results allow us to conclude that numerical model is a powerful and promising tool to simulate syntectonic sedimentation and to study the interaction between sediments and deformation.

The first comparison with a real geological example (the Sobrarbe fold system) gives new insights to be considered, and makes worth to take into an account the effect of syntectonic sedimentation as another factor that can influence the final fold geometry and the deformation style.

6.2.4 Final remarks

The results of the experiments support the viability of the approach of combining the two models (i.e. SFM and DEM). Thus, we can conclude that this new tool can allow

us to perform a more realistic and detailed study of the manner in which sedimentation and tectonics interact in nature.

Nonetheless, two key issues limit the performance of the model. The first is the size of the DE, which limits the resolution and accuracy of the model, and also controls the transfer of sediments between models. The second is the difficulty, with the current methodology, of the finite element mesh to adapt to a DEM surface when an abrupt topography, with high slopes, is formed.

However, despite these two issues, the model has been applied in several cases studies successfully, and it can be concluded that the model meets the objective for which it is designed: to study the syntectonic sedimentation (syntectonic architectures and sedimentary patterns in tectonic settings), and how these processes interact and are influenced by each other.

6.3 FUTURE WORK

Although the main objectives of this thesis have been fulfilled, new (and exciting) goals have arisen. These goals can be envisaged as a future work, which can be divided in three main groups as follows: (a) possible future case studies; (b) suggested improvements; and (c) new features to be added to the current model.

a) The first group, which can also be classified as a short-term future work, would be related to the application of the code to new cases studies, or, further develop of those presented in this thesis.

For example, the case study that analyses the effect of normal faulting and a relay ramp in sediment dispersal could be expanded in distinct ways. Firstly, the effect of decreasing or increasing, the distance, and also the overlap, between faults in the final sediment dispersal could be studied. Secondly, and considering a fixed position of the two faults, one could study the effect of the syntectonic sediment on the deformation of the pretectonic unit, comparing the same example with and without syntectonic sediments. The deformation can also be analysed considering different rheological conditions, by defining different cohesions or coefficient frictions, and considering, or not, syntectonic sediments.

Another case study, which is currently in progress, is to investigate the effect of syntectonic sedimentation in a contractional environment considering one intermediate weak décollement level. The intermediate weak layer is defined as frictionless layer and with low cohesion, while the rest of the pretectonic materials are defined with friction and

cohesion. These experiments would examine different geometries of the décollement level as well as different pinch out geometries. The main aim would be to characterize the deformation of the décollement level and the related structures in function of the decóllement level geometry and considering again, or not syntectonic sedimentation.

b) The second group of future works would include medium-terms tasks, which would be those related to the improvement of the code in order to overcome some of its limitations (section 3.2.6). The first priority, as commented in chapter 3, would be the incorporation of an adaptive mesh to have more accurate results in those areas with abrupt slope changes. The main aim of the new adaptive mesh would be, not only to improve accuracy in the sedimentary model (e.g. fluid flow depend on bathymetry), but also to improve the current new numerical model. The algorithm to introduce an adaptive mesh into the code has already been developed. Nonetheless, it has not been presented in this thesis because its final implementation needs some important adaptations related to the transport equation. In this sense, a necessary change is to re-define the dispersion coefficients of the transport equation, specifically for each element of the mesh, and as a function of the element mesh size, which will change with the re-meshing processes. This improvement would need further testing of the transport equation in order to avoid numerical errors.

The next suggested improvements are related to the limitations produced due to the size of the DE, through the parallelization of the code in MPI. MPI is a type of parallelization, which mainly differs from the openMP parallelization in the fact that MPI allows to run the code in a computers cluster with non-shared memory. This will enable running the model with a larger number of processors than the currently used. This allows us to decrease the diameter of the spheres and increase the amount of DEs used in the examples without increasing (at least too much) the computing time. This will provide a double benefit: on the one hand a gain in the resolution of both the sedimentary and deformation model, and on the other hand, an improvement in the sediment transfer between both models. It also enables the model to simulate more complex geological scenarios.

c) The third group of future works would be related to the introduction of new features in the model, as the addition of new processes such as erosion, or other sediment types, e.g. carbonates or turbidites among others. It could also be considered to include subaerial processes. The idea is that the new proposed sedimentary processes could interact or exchange information with the deformation model in a similar way to the current

syntectonic sedimentary model. However, to introduce the right models for each new process will need to go through all the work methodology applied already in this thesis. .

These tasks would be not essential to the model itself, and they can be thought of as long-term tasks. Nonetheless, their incorporation to the model would make the model more complete.

CHAPTER 7

BIBLIOGRAPHY

Allen M.P., Tidsley D.J., 1987. Computer simulations of liquids. Edited by Oxford Science Publications.

Allmendinger R. W., 1998. Inverse and Forward numerical modeling of trishear fault-propagation folds. Tectonics, 17(4), 640-656

Antonellini M.A., Pollard D.D., 1995. Distinct element modeling of deformation bands in sandstone. *Journal of Strucrural Geology*. 17(8), 1165-1182.

Athmer W., Gonzalez Uribe G.A., Luthi S. M., Donselaar M. E., 2011. Tectonic control on the distribution of Palaeocene marine syn-rift deposits in the FenrisGraben, northwesternVøring Basin, offshore Norway. *Basin Research*. 23, 361-375

Athmer W., Groenenberg R.M., Luthi S. M., Donselaar M. E., Sokoutis D., Willingshofer E., 2010. Relay ramps as pathways for turbidity currents: a study combining analogue sandbox experiments and numerical flow simulations. *Sedimentology*. 57, 806-827

Athmer W., Luthi S. M., 2011. The effect of relay ramps on sediment routes and deposition: A review. *Sedimentary Geology*. 242, 1-17

Barrier L., Nalpas T., Gapais D., Proust J.N., Casas A., Bouquin S., 2002. Influence of syntectonic sedimentation on thrust geometry. Field examples from the Iberian Chain (Spain) and analogue modelling. *Sedimentary Geology*. 146, 91-104.

Bernal A., Hardy S., 2002. Syntectonic sedimentation associated with three-dimensional fault-bend fold structures: a numerical approach. *Journal of Structural Geology*. 24, 609-635

Bertrand F., Leclaire L.A., Levecque G., 2005. DEM-based models for the mixing of granular materials. *Chemical Engineering Science*. 60, 2517 – 2531

Bice D.M., 1991. Computer simulation of carbonate platform and basin systems. *Kansas Geological Survey Bulletin*. 233, 431-447.

Bitzer K., Pflug R., 1990. DEPO3D: A three-dimensional model for simulating clastic sedimentation and isostatic compensation in sedimentary basins. *Quantitative Dynamic*

Stratigraphy. Edited by TA Cross, 1990.

Bitzer K., Salas R., 2001. Simulating Carbonate and mixed carbonate-clastic sedimentatio using predator-prey models. Editors: Merriam D. Davis J.C). *Geologic modeling and simulation: sedimentary systems*. Kluwer Academic/Plenum publications. 169-204.

Bitzer K., Salas R., 2002. Simsafadim: Three-dimensional simulation stratigraphic architecture and facies distribution modelling of carbonate sediments. *Computers and Geosciences*. 28, 1177-1192.

Bitzer K., 1997. BASIN: A finite-element model for simulation of consolidation, fluid flow, solute transport and heat flow in sedimentary basins. In: Pawlowsky-Glahn V. (eds). Proceedings of the Third Annual Conference of the International Association for Mathematical Geology. Part I, 444-449.

Blanchette F., Strauss M., Meiburg E., Kneller B., Glinsky M.E., 2005. High-resolution numerical simulations of resuspending gravity currents: conditions for self-sustainment. *Journal of Geophysical Research*.110, C12022, doi:10.1029/2005JC002927.

Bobet, A., Fakhimi, A., Johnson, S., Morris, J., Tonon, F., and Yeung, M., 2009. Numerical Models in Discontinuous Media: Review of Advances for Rock Mechanics Applications. *Journal of Geotechnical and Geoenvironmental Engineering*. 135 (11), 1547-1561.

Bruhn R., Vagle K., 2005. Relay ramp evolution and mass flow deposition (Upper Kimmeridgian Lower Volgian) in the Tail End Graben,Danish North Sea. *Basin research*, 17, 551-567

Burgess, P.M., Lammers, H., Van Oosterhout, C., Granjeon, D, 2006. Multivariate sequence stratigraphy: tackling complexity and uncertainty with stratigraphic forward modeling, multiple scenarios and conditional frequency maps. *AAPG Bulletin.* 90, 1883–1901.

Burgess P.M., Wright V., Emery D., 2001. Numerical forward modelling of peritidal carbonate parasequence development: implications for outcrop interpretation. *Basin Research*. 13, 1-16.

Burgess P. 2012. Chapter: A brief review of developments in stratigraphic forward modelling, 200-2009. In *Regional geology and Tectonics: principles of geologic analysis*. Editors:

Roberts D.G., Bally A.W.

Burgess P.M., 2013. CarboCAT. A cellular automata model of heterogeneous carbonate strata. *Computers and Geosciences*. 53, 129-140.

Cardozo N., Allmendinger R.W., 2009. SSPX: a program to compute strain from displacement/velocity data. *Computers and Geosciense*. 35(6), 1343–1357.

Carmona A., Clavera-Gispert R., Gratacós O., Hardy S., 2010. Modelling syntectonic sedimentation: combining a discrete element model of tectonic deformation and a process-based sedimentary model in 3D. *Mathematical Geoscience*. 42, 519-534

Childs C., Watterson J., Walsh J. J., 1995. Fault overlap zones within developing normal faults systems. *Journal of the Geological Society, London,*152, 535-549

Clavera-Gispert R., Carmona A., Gratacós O., Tolosana-Delgado R., 2012. Incorporating nutrients as a limiting factor in carbonate modelling. *Palaeogeography, Palaeoclimatology, Palaeoecology*. 329-330, 150-157.

Clavera-Gispert R., Carmona A., Gratacós O., Tolosana-Delgado R., 2015. Process-based forward numerical ecological modelling for carbonate sedimentary basins. Submitted to *Computers and Geosciences*.

Clavera-Gispert R., 2016. Forward numerical modelling of carbonate basins: an ecological approach. TU Freiberg Germany.

Clearly P.W., 2000. DEM simulation of industrial particle flows: case studies of dragline excavators, mixing in tumblers and centrifugal mills. *Powder technology*. 109, 83-104

Clearly P.W., Sawley M. L., 2002. DEM modelling of industrial granular flows: 3D case studies and the effect of particle shape on hopper discharge. *Applied Mathematical Modelling*. 26, 88-11

Clevis Q., Boer D.E., Wachter P.M., 2003. Numerical modelling of drainage basin evolution and three-dimensional alluvial fan stratigraphy. *Sedimentary Geology*. 163 (1-2), 85-110.

Cooper K.A., Hardy S., Gawthorpe R., 2003. Stratigraphic and structural expression of the lateral growth of thrust fault-propagation folds: results and implications from kinematic

modelling. *Basin Research*. 15, 165-182.

Courant R., Friedricks K., Lewy H., 1967 [1928]. On the partial difference equations of mathematical physics. *IBM Journal of Research and Development*. 11(2), 215-234.

Cowie P.A., Tucker G.E., Whittaker A.C., Naylor M., Ganas A., Roberts G. P., 2006. Investigating the surface process response to fault interaction and linkage using a numerical modelling approach. *Basin Research.* 18, 231-266

Cundall P.A., 1971. A computer model for simulating progressive, large-scale movements in blocky rock systems. *Proc. Symp. Int. Soc. Rock Mech.*, Nancy 2, 8

Cundall P.A., 1978. BALL- A program to model granular media using the distinct element method. Technical Note. Advanced Technology Group, Dames & Moore, London

Cundall P.A., Strack O.D.L., 1979. A discrete numerical model for granular assemblies. *Géotecnique.* 29 (1), 47-65.

Dawers N.H., Underhill J.R., 2000. The role of fault interaction and linkage in controlling synrift stratigraphic sequences: Late Jurassic, Statfjord East area, Northern North Sea. *AAPG Bulletin*. 84(1), 45-64.

De Josselin de Jong G., Verruijt A., 1969. Etude photo-élastique d'un empilement de disques. *Cahiers du Groupe français d'Etudes de Rhéologie*. 2, 73-8.

Deresiewicz H., 1958. Mechanics of granular material. *Advances in Applied Mechanics*, 5, 233-306.

Donzé F., Mora P., Magnier S.A.,1994. Numerical simulation of faults and shear zones. *Geophysical Journal International,* 116, 46-52.

Doutsos T., Piper D.J.W., 1990. Listric faulting, sedimentation, and morphological evolution of the Quaternary eastern Corinth rift, Greece: First stages of continental rifting. *Geological Society of America Bulletin,* 102, 812-829.

Duerto L., McClay K., 2009. The role of syntectonic sedimentation in the evolution of doubly vergent thrust wedges and foreland folds. *Marine and Petroleum Geology*. 26, 1051-1069.

Erslev E. A., 1991. Trishear fault-propagation folding. *Geology*, 19(6), 617-620

Fillon C., Huismans R.S., van der Beek P., 2013. Syntectonic sedimentation effects on the growth of fold-and-thrust belts. *Geology*. 41, 83-86

Finch E., Hardy S., Gawthorpe R., 2003. Discrete element modelling of contractional faults-propagation folding above rigid basement rocks. *Journal of Structural Geology*, 25, 515–528.

Finch E., Hardy S., Gawthorpe R., 2004. Discrete element modelling of extensional faults propagation folding above rigid basement rocks. *Basin Research*, 16, 489–506

Flemings P.B., Jordan T.E., 1989. A synthetic stratigraphic model of foreland basin development. *Journal of Geophysical Research.* 94, 3851-3866.

Fossen, H., Rotevatn, A., 2015. Fault linkage and relay structures in extensional settings – a review. *Earth Science Reviews*. doi: 10.1016/j.earscirev.2015.11.014

Fugelli, E.M.G., Olsen, T.R., 2007. Delineating confined slope turbidite systems offshore mid-Norway: the Cretaceous deep-marine Lysing Formation. *AAPG Bulletin*. 91 (11), 1577–1601.

Gawthorpe R.L., Colella A., 1990. Tectonics controls on coarse-grained delta depositional systems in rift basins. *The International Association of Sedimentologists.* Especial Publication 10, 113-127

Gawthorpe R.L, Hardy S., Ritchie B., 2003. Numerical modelling of depositional sequences in half-graben rift basin. *Sedimentology*. 50, 169-185.

Gawthorpe R.L., Hardy S., 2002. Extensional fault-propagation folding and base-level changes as controls on growth strata geometries. *Sedimentary Geology.* 146,47-56.

Gawthorpe R.L., Hurst J.M., 1993. Transfer zones in extensional basins: their structural style and influence on drainage development and stratigraphy. *Journal of the Geological Society, London*. 150, 1137-1152.

Gawthorpe R.L., Leeder M.R., 2000. Tectonic sedimentary evolution of active extensional basin. *Basin Research*. 12, 195-218.

Granjeon, D., Joseph, P., 1999. Concepts and applications of a 3-D multiple lithology, diffusive model in stratigraphic modeling. Numerical experiments in stratigraphy: recent

advances in stratigraphic and sedimentologic computer simulations. *SEPM Spec. Publ.* 62, 197– 210.

Granjeon, D., 2010. Dionisos - 3D Stratigraphic modelling of sedimentary basins. *AAPG-ER Newsletter, R&D projects*. 2, 3-4.

Gratacós O., Bitzer K., Cabrera L., Roca E., 2009a. SIMSAFADIM-CLASTIC: a new approach to mathematical 3D forward simulation modelling for clastic and carbonate sedimentation. *Geologica Acta*. 7, 311-322.

Gratacós O., Bitzer K., Casamor J.L., Cabrera L., Calafat A., Canals M., Roca E., 2009b. Simulating transport and deposition of clastic sediments in an elongate basin using the SIMSAFADIM-CLASTIC program: The Camarasa artificial lake case study (NE Spain). *Sedimentary Geology*. 222(1–2), 16-26.

Gratacós O., 2004. Simsafadim-Clastic: modelización 3D de transporte y sedimentación clástica sub-acuática. *Tesis doctoral*. Universidad de Barcelona

Griffiths C. M., Dyt C., Paraschivoiu E., Liu K., 2001. Sedsim in hydrocarbon exploration. Chapter of *Geologic Modeling and Simulation, Sedimentary Systems*. Edited by Springer. 71-91.

Gupta S., Underhill J.R., Sharp I.R., Gawthorpe R.L., 1999. Role of fault interactions in controlling synrift sediment dispersal patterns: Miocene, Abu Alaqa Group, Suez Rift, Sinai, Egypt. *Basin Research*. 11, 167-189.

Hardy S., Finch E., 2005. Discrete-element modelling of detachment folding. *Basin Research*. 17, 507-520.

Hardy S., Finch E., 2006. Discrete element modelling of the influence of cover strength on basement involved fault-propagation folding. *Tectonophysics,* 415, 225–238.

Hardy S., Finch E., 2007. Mechanical stratigraphy and the transition from trishear to kink-band fault propagation fold forms above blind basement thrust faults: a discrete-element study. *Marine and Petroleum Geology*. 24, 75–90.

Hardy S., Ford, M., 1997. Numerical modelling of trishear fault-propagation folding and associated growth strata. *Tectonics*. 16(5), 841-854.

Hardy S., Gawthorpe R.L., 2002. Normal fault control on bedrock channel incision and

sediment supply: Insights form numerical modeling. *Journal of Geophysical Research*. 117, NO.B10, 2246, doi:10.1029/2001JB000166

Hardy S., McClay K., Muñoz J.A., 2009. Deformation and fault activity in space and time in high-resolution numerical models of doubly vergent thrust wedges. *Marine and Petroleum Geology*. 26, 232-248.

Hardy S., 2008. Structural evolution of calderas: Insights from two-dimensional discrete element simulations. *Geology*. 36(12), 927-930.

Hardy S., 2011. Cover deformation above steep, basement normal faults: Insights from 2D discrete element modeling. *Marine and Petroleum Geology*. 28, 966-972.

Hardy S., 2013. Propagation of blind normal faults to the surface in basaltic sequences: Insights from 2D discrete element modeling. *Marine and Petroleum Geology,* 48, 149-159.

Hemelsdaël R., Ford M., 2014. Relay zone evolution: a history of repeated fault propagation and linkage, central Corinth rift, Greece. *Basin Research*. 1-23, doi: 10.1111/bre.12101

Hoogendoorn R.M., Overeem I., Storms J.E.A., 2008. Process-response modeling of fluvio-deltaic stratigraphy. *Computers and Geosciencies*. 34, 1394-1416.

Huang X., Dyt C., Griffiths C., Salles T., 2012. Numerical forward modelling of 'fluxoturbidite' flume experiments using Sedsim. *Marine and Petroleum Geology*. 35, 190-200

Hutton E.W.H., Syvitski J.P.M., 2008. Sedflux 2.0: An Advanced process-response model that generates three-dimensional stratigraphy. *Computer and Geosciences*. 34, 1319-1337.

Jain R., Kasturi R., Schunk B.G., 1995. Machine Vision. Edited by Mc Graw-Hill series in computer sciences. Chapter 4.

Jing L., 2003. A review of techniques, advances and outstanding issues in numerical modelling for rock mechanics and rock engineering. *International Journal of Rock Mechanics and Mining Sciences*. 40, 283-353.

KetterHagen W.R., Am Ende M. T., Hancock B. C., 2009. Process modelling in the Pharmatheutical Industry using the Discrete Element Method. *Journal of Pharmaceutical Sciences*. 98(2), 442-470.

Kinzelbach W., 1986. Groundwater modelling: an introduction with sample programs in BASIC. Elsevier, Amsterdam

Kneller B., Buckee C. The structure and fluid mechanics of turbidity currents: a review of some recent studies and their geological implications. *Sedimentology*. 47 (Suppl. 1) 62-97.

Kramer J. 2007. Is abstraction the key of computing?. *Comunications of the ACM*. 50 (4), 37-42.

Kristensen M.B., Childs C.J., Korstgård J. A., 2008. The 3D geometry of small-scale relay zones between normal faults in soft sediments. *Journal of Structural Geology*. 30, 257-272.

Lee Barbour S.L., Krahn J., 2004. Numerical modelling, prediction or process?. *Geotechnical News*. December 2004, 44-52.

Long J.J., Imber J., 2011. Geological controls on fault relay scaling. *Journal of Structural Geology*. 33(12), 1790-1800.

Lorig L.J., Brady B.H.G., Cundall P.A., 1986. Hybrid distinct element-boundary element analysis of jointed rock. *International Journal of Rock Mechanics, Mining Science & Geomechanics*. 23(4), 303-312.

Maniatis G., Kurfeß D., Hampel A., Heidbach O., 2009. Slip acceleration on normal faults due to erosion and sedimentation – Results from a new three-dimensional numerical model coupling tectonics and landscape evolution. *Earth and Planetary Science Letters*. 284: 570-582.

Mercer J.W., Faust C.R., 1981. Ground-water modeling. Worthington, Ohio: National Water Well Association. 60 pp.

Mora P., Place D., 1993. A lattice solid model for the non-linear dynamics of earthquakes. *International Journal of Modern Physics Computer*. 4(6), 1059–1074.

Mora P., Place D., 1994. Simulation of the frictional stick-slip instability. *Pure Applied Geophysics*. 143(1–3), 61–87.

Mora P., Place D., 1998. Numerical simulation of earthquake faults with gouge: Towards a comprehesive explanation for the heat flow paradox. *Journal of Geophysical Research, Solid Earth*. 103(B9) 21067-21089.

Mora P., Place D., 1999. The weakness of the earthquake faults. *Geophysical Research Letters*. 26, 123-126.

Moreno R., Ghadiri M., Antony S.J., 2003. Effect of the impact angle on the breakage of agglomerates: a numerical study using DEM. *Powder Technolology*. 130, 132-137.

Morley C.K., R.A. Nelson, T.L. Patton, and S.G. Munn, 1990. Transfer zones in the East African Rift system and their relevance to hydrocarbon exploration in rifts. *AAPG Bulletin*. 74, 1234-1253.

Morris J., Glenn L., Blair S., Heuze F., 2011. The Distinct Element Method - Application to structures in jointed rock. *International Workshop Mesh free Method of Partial Differential Equations*. Bonn,Germany, September 11-14, 2001.

Moustafa A. R., 2002. Controls on the geometry of transfer zones in the Suez rift and northwest Red Sea: Implications for the structural geometry of rift systems. *AAPG Bulletin*. 86 (6), 979–1002.

Munjiza A., Owen D.R.J., Bicanic N., 1995. A combined finite-discrete element method in transient dynamics of fracturing solids. *Engineering Computations*. 12, 145-174

Munjiza A., 2004. The Combined Finite-Element Method. Edited by Wiley &Sons.

Muñoz J.A., Beamud E., Fernández O., Arbués P., Dinarès-Turell J., Poblet J., 2013. The Ainsa Fold a thrust oblique zone of central Pyreness: Kinematics of a curved contractional system from paleomagnetic and structural data. *Tectonics*. 32, 1-34.

Murray A.B., Paola C., 1997. Properties of a cellular braided stream model. *Earth Surface Processes Landforms*. 22, 1001-1025.

Nicholas A. P., Quine T.A., 2007. Modeling alluvial landform change in the absence of external environmental forcing. *Geology*. 35, 527-530.

Nicol A., Gillespie P.A., Childs C., Walsh, J.J., 2002. Relay zones between mesosocopic thrust faults in layered sedimentary sequences. *Journal of Structural Geology*. 24, 709-727.

Oreskes N., Shrader-Frechette K., Belitz K., 1994. Verification, validation, and confirmation of numerical earth sciences. *Science*. 263, 4th Febrary, 641

Paola C., 2000. Quantitative models of sedimentary basin filling. *Sedimentology*. 47 (Suppl. 1)

121-178.

Peacock D.C.P., 2002. Propagation, interaction and linkage in normal fault systems. *Earth-Sciencies Reviews*. 58, 121-142.

Place D., Lombard F., Mora P., Abe S., 2002. Simulation of the micro- physics of rocks using LSMEarth. *Pure and Applied Geophysics*. 159, 1911–1932.

Poblet J., Muñoz J.A., Travé A., Serra-Kiel J., 1998. Quantifying the kinematics of detachment folds using three-dimensional geometry: Application to the Mediano anticline (Pyrenees, Spain). *Geological Society of America Bulletin*. 110 (1), 111-125.

Richards K., Bithell M., Dove M., Hodge R., 2004. Discrete element modelling: methods and applications in environmental sciences. *Philosophical Transactions of the Royal Society A: Mathematical, Physical and Engineering Sciences*. 362, 1797-1816.

Ritchie B.D., Gawthorpe R. L., Hardy S., 2004. Three-dimensional numerical modeling of deltaic depositional sequences 1: Influence of the rate and magnitud of sea-level change. *Journal of Sedimentary Research*. 74 (2), 203-220.

Ritchie B.D., Gawthorpe R. L., Hardy S., 2004. Three-dimensional numerical modeling of deltaic depositional sequences 1: Influence of local controls. *Journal of Sedimentary Research*. 74 (2), 221-238.

Rodriguez-Ortiz J.M., 1974. Estudio del comportamiento de medios granulares heterogéneos mediante modelos discontinuos analógicos y matemàticos. *Phd Tesis*. Universidad Politécnica de Madrid.

Rohais S., Eschard R., Ford M., Guillocheau F., Moretti I., 2007. Stratigraphic architecture of the Plio-Pleistocene infill of the Corinth Rift: Implications for its structural evolution. *Tectonophysics*. 440, 5-28.

Salvini S., Storti F., 2002. Three-dimensional architecture of growth strata associated to fault-bend, fault-propagation, and de´collement anticlines in non-erosional environments. *Sedimentary Geology* . 146, 57-73.

Schöpfer M.P.J., Abe S., Childs C., Walsh J.J., 2009. The impact of porosity and crack density on the elasticity, strength and friction of cohesive granular materials: Insights from DEM modelling. *International Journal of Rock Mechanics & Mining Sciences*. 46, 250-261.

Shaw J.H., Novoa E., Connors C.D., 2004. Structural controls on growth stratigraphy in contractional fault-related fold, in McClay K.R, ed. *Thrust tectonics and hydrocarbon systems: AAPG Memoir*. 82, 400-412.

Shi G. H., 1988. Discontinuous deformation analysis - a new numerical model for the statics and dynamics of block systems. *PhD Thesis*. University of California, Berkeley.

Simpson G.D.H., 2009. Mechanical modelling of folding versus faulting in brittle-ductile wedges. *Journal of Structural Geology*. 31, 369-381.

Soliva R., Benedicto A., 2004. A linkage criterion for segmented normal faults. *Journal of Structural Geology*. 26, 2251-2267.

Somme, T.O., Helland-Hansen, W., Granjeon, D., 2009. Impact of eustatic amplitude variations on shelf morphology, sediment dispersal, and sequence stratigraphic interpretation: Icehouse versus greenhouse systems. *Geology*. 37, 587–590.

Storti F., Poblet J., 1997. Growth stratal architectures associated to decollement folds and fault-propagation folds. Inferences on fold kinematics. *Tectonophysics*. 282, 353-373.

Syvitski J.P.M., Alcott J.M., 1995. DELTA6: numerical simulation of basin sedimentation affected by slope failure and and debris flow runout. In: *proceedings of the Pierre Beghin international workshop on rapid gravitational mass movements*. Grenoble, France, 305-312.

Syvitski J.P.M., Hutton E.W.H., 2001. 2D SEDFLUX 1.0C: an advanced process-response numerical model for the fill of marine sedimentary basins. *Computers&Geosciencies*. 27 (6), 731-754.

Tetzlaff, D.M., Harbaugh J.W., 1989. Simulating clastic sedimentation. *Van Nostrand Reinhold*. New York, 202pp.

Tetzlaff D.M., 2005. Modelling Coastal Sedimentation through Geologic Time. *Journal of Coastal Research*. 21(3), 610 – 617.

Trudgill B., Cartwright J., 1994. Relay ramps forms and normal-fault linkages, Canyolands National Park Utah. *Geological Society of America Bulletin.* 106 (9), 1143-1157.

Velten K., 2009. Mathematical modeling and simulation. Edited by Wiley-VCH - Verlag GmbH & Co. KGaA.

Waltham D., Jaffey N., MacLean S., Zampetti V., 2008. Stratigraphic modelling of turbidite proscpects to reduce exploration risk. *Petroleum Geoscience*. 14, 273-280.

Warner J.C., Sherwood C.R., Signell R.P., Harris C.K., Arango H.G., 2008. Development of a three-dimensional, regional, coupled wave, current and sediment-transport model. *Computer &Geosciencies*, 34, 1284-1306.

Williams J.R., Hocking G., Mustoe G.G.W.,1985. The theoretical basis of the discrete element method. NUMETA '85, Balkema, Rotterdam

Williams J.R., Mustoe G.G.W., 1987. Modal methods for the analysis of discrete systems. *Computer and Geotechnics*. 4, 1-19.

Yin H., Zhang J., Meng L., Liu Y., Xu S., 2009. Discrete element modeling of the faulting in the sedimentary cover above an active salt diapir. *Journal of Structural Geology*. 31, 989-995.

Young, M.J., Gawthorpe, R.L., Hardy, S., 2001. Growth and linkage of a segmented normal fault zone; the Late Jurassic Murchison-Statfjord North Fault, northern North Sea. *Journal of Structural Geology,* 23, 1933–1952.

Young M.J., Gawthorpe R.L., Sharp I.R., 2002. Architectura and evolution of syn-rift clastic depositional systems towards the tip of a major fault segment, Suez Rift, Egypt. *Basin Research*, 14, 1-23.

Walsh J.J., Watterson J., Bailey W.R., Childs C., 1999. Faults relays, bends and branch-lines.*Journal of Structural Geology*, 21, 1019-1026.

APPENDIX

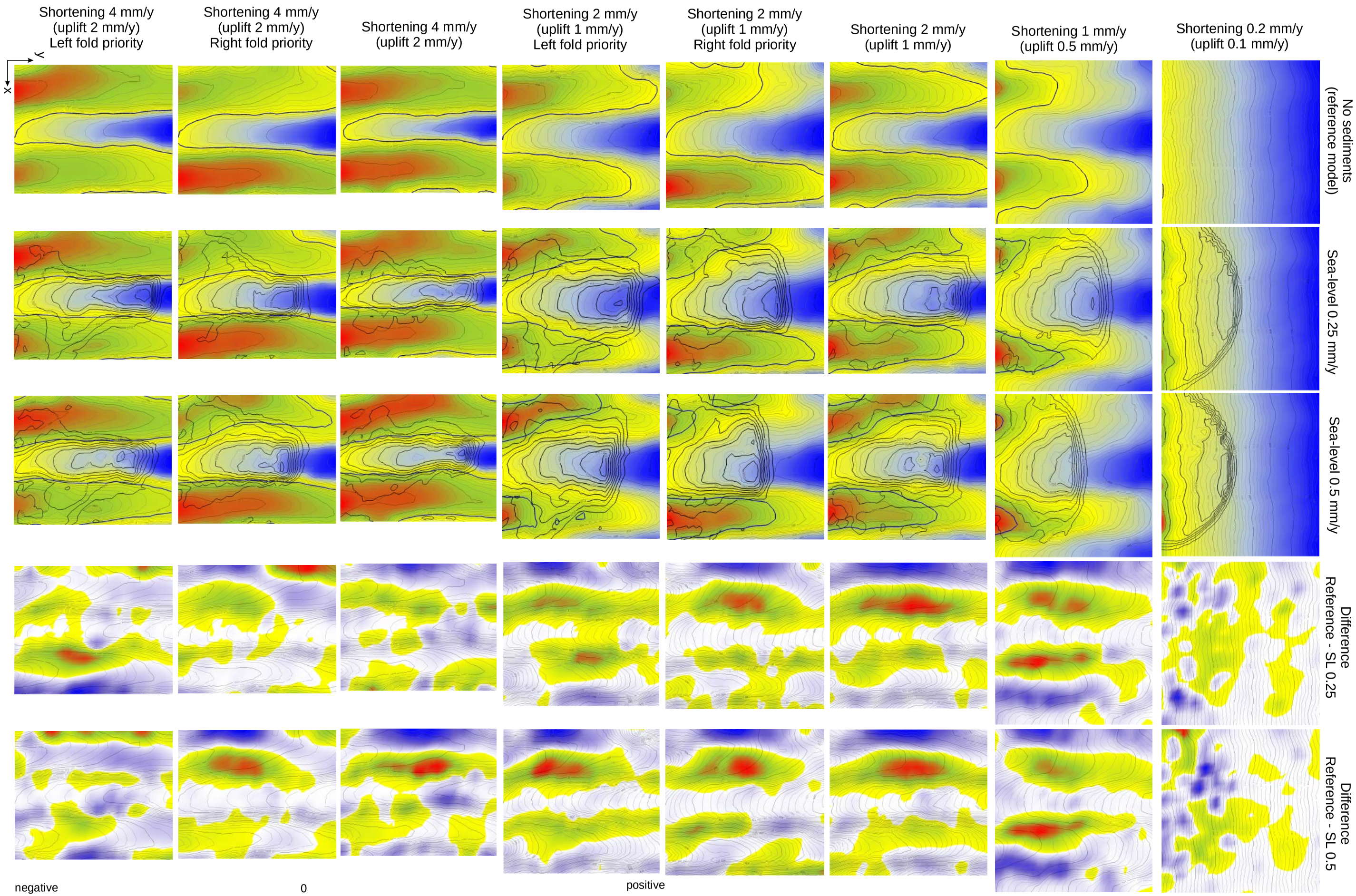

Contour coloured maps for the top of the pre-tectonic unit for the different experiments (without sediments, with sediments and a sea-level rise rate of 0.25 and 0.5 mm/y), considering different shortening rates: 0.2mm/y, 1mm/y, 2mm/y and 4mm/y (or 0.1mm/y, 0.5mm/y, 1mm/y and 2mm/y uplift rate respectively). The right-side anticline priority and the left-side anticline priority are also included. The isopach map for the syn-tectonic unit is superimposed (black contour lines). The difference between the top of the pre-tectonic unit in the reference model and the experiments with sediments are also included in order to highlight the effect of sedimentation on the top of the pre-tectonic unit surface.

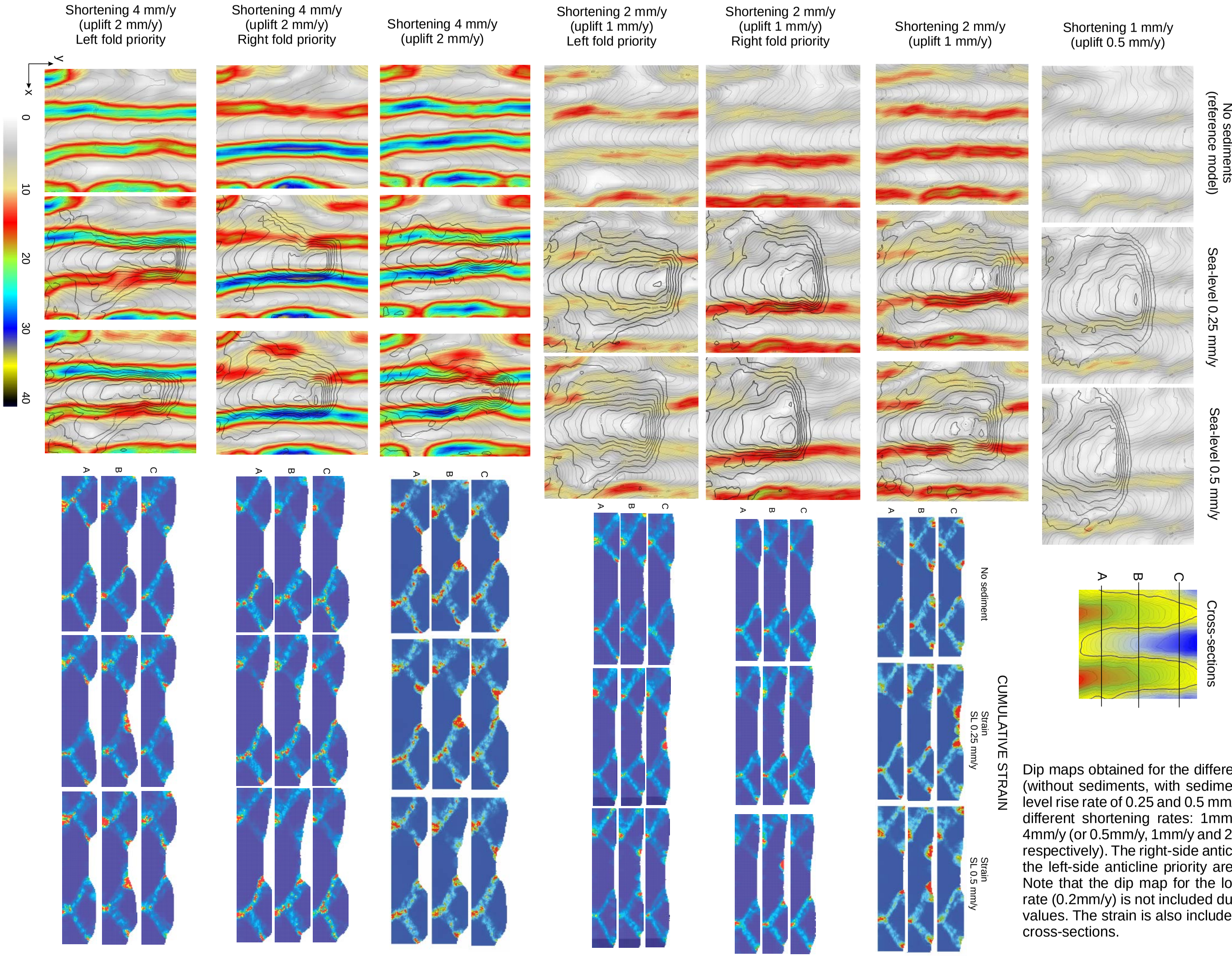

Dip maps obtained for the different experiments (without sediments, with sediments and a sea-level rise rate of 0.25 and 0.5 mm/y), considering different shortening rates: 1mm/y, 2mm/y and 4mm/y (or 0.5mm/y, 1mm/y and 2mm/y uplift rate respectively). The right-side anticline priority and the left-side anticline priority are also included. Note that the dip map for the lower shortening rate (0.2mm/y) is not included due to the low dip values. The strain is also included for 3 different cross-sections.